

Micropropulsion for Space Probes of Particle Cosmology



Maheen Parbhoo

School of Physics
University of Witwatersrand

Submitted in fulfilment of the requirements for the degree of
Master of Science

January 2022

To my parents, sister and dearly departed grandmother . . .

Declaration

I hereby declare that except where specific reference is made to the work of others, the contents of this dissertation are original and have not been submitted in whole or in part for consideration for any other degree or qualification in this, or any other university. This dissertation is my own work and contains nothing which is the outcome of work done in collaboration with others, except as specified in the text and Acknowledgements. This dissertation contains fewer than 65,000 words including appendices, bibliography, footnotes, tables and equations and has fewer than 150 figures.

M. Parbhoo

Maheen Parbhoo

23 January 2022

Acknowledgements

To my primary supervisor Prof. Philippe Ferrer, Thank you for all of your guidance, patience and support throughout the duration of my master's candidature. You have inspired me to think in novel ways and have contributed significantly towards my development as a young researcher.

To Prof. Vishnu Jejjala, Thank you for your prompt responses to my emails and for assisting me with funding for the duration of my research term.

To Mr Gerrad Peters, I greatly appreciate your assistance with the cleaning of my samples and for allowing me to use the optical and scanning electron microscopes.

To all the gentlemen at the mechanical workshop, I am extremely grateful for your assistance with the fabrication of components and experimental apparatus, without your help none of the experiments would have been possible.

Last but not least, to my good friend Paul, your ingenious (and sometimes outlandish) ideas have served me well. I have had much fun engaging in banter with you and wish you all the best in your endeavours.

The financial assistance of the National Research Foundation (NRF) towards this research is hereby acknowledged. Opinions expressed and conclusions arrived at, are those of the author (Mr. Maheen Parbhoo) and are not necessarily to be attributed to the NRF.

Abstract

The accumulation of orbital debris poses many risks for current and future space missions. Along with an increasing number of satellite launches forecast for the coming years, it has now become mandatory for newly launched payloads to have end-of-life disposal mechanisms. Furthermore, as the market for small satellites continues to grow, there is a demand to improve the performance of these systems to allow for more complex missions to be realised. An on-board propulsion system would allow a spacecraft to perform various orbital manoeuvres, like formation flying and altitude control, which would greatly improve the operational capabilities of the satellite.

Recent advancements in Microelectromechanical systems detectors and miniaturised radio frequency transmitters are facilitating a new domain for CubeSat-based astronomy research. Such in-space observatories, consisting of a constellation of CubeSats forming large distributed apertures, may allow for a rapid cost effective means of making major scientific breakthroughs. In the field of particle cosmology, these CubeSat missions can work in conjunction with ground based observatories to conduct multiwavelength observations. One of the key components for mission success is an on-board micropropulsion system needed for satellite maneuverability.

To date, the integration of miniaturised propulsion systems on CubeSats has proven challenging, due power and mass budget restrictions. To address these issues, a proof of concept DC discharge microthruster was developed. The system utilises a coupling of propellant ionisation and acceleration mechanisms which eradicates the need for additional components, leading to reduced mass and power consumption. In this research, experimental tests were performed to characterise the system's feasibility for use as an on-board propulsive mechanism. Preliminary experiments were conducted whereby the relation between the thruster's electrical behaviour against variations in the electrode aperture size were explored and the thruster's stable operating parameters were deduced. The subsequent experiments aimed to study the effect of variations in the number of electrode extraction apertures on the discharge behaviour and the magnitude of extracted ion beam current. From the measured values the

system's main performance metrics (thrust and electrical efficiency) were inferred and used to evaluate the overall feasibility of the thruster concept.

Table of contents

List of figures	x
List of tables	xvi
Nomenclature	xviii
1 Introduction	1
1.1 Characteristics of Small Satellites	1
1.2 Micropropulsion Systems for CubeSats	2
1.3 Research Objectives	8
1.4 Research Methodology	9
1.5 Dissertation Structure	11
2 CubeSat Micropropulsion- Enabling Breakthroughs in Particle Cosmology	12
2.1 Introduction	12
2.2 Motivation for utilising CubeSats to conduct research in particle cosmology	13
2.3 Enhancing mission capabilities with on-board micropropulsion systems	15
2.4 CubeSat mission concepts for particle cosmology	16
2.4.1 HaloSat: The search for mission baryons	16
2.4.2 RELIC: Characterising energy transport from black holes	17
2.5 Conclusions	20
3 Literature Survey	21
3.1 Fundamentals of Propulsion	21
3.2 Electric Micropropulsion Concepts	24
3.2.1 Electrothermal thrusters	25
3.2.2 Electrostatic thrusters	26
3.2.3 Electromagnetic thrusters	32

3.2.4	Propellant-less propulsion	34
3.3	Basic Plasma Physics	35
3.3.1	The plasma state of matter	35
3.3.2	Definition of a plasma	38
3.3.3	Plasma particle energies and velocities	42
3.3.4	Collisional processes and collision frequencies	43
3.3.5	Plasma sheaths	45
4	Glow Discharge Theory and Simulation	50
4.1	DC Glow Discharges	50
4.1.1	Electrical breakdown in low pressure gases	52
4.1.2	Paschen's law	55
4.1.3	Anatomy of normal glow discharge	56
4.2	Argon Glow Discharge Simulation	58
5	Materials and Experimental Apparatus	68
5.1	Materials	68
5.1.1	Electrode and thruster body material selection	68
5.1.2	Geometric considerations	69
5.1.3	Selection of propellant gas	71
5.2	Experimental Apparatus	71
5.2.1	Vacuum chamber	71
5.2.2	Vacuum pump system	73
5.2.3	Power supply	73
5.2.4	Oscilloscope	74
5.2.5	Micro-controller and current sensor board	75
5.2.6	Mass flow measurement system	75
5.2.7	Optical Microscope	76
6	Preliminary Experimental Tests	78
6.1	Introduction	78
6.2	Theory	79
6.3	Aims	82
6.4	Apparatus	82
6.5	Methodology	83
6.6	Results and Discussion	85
6.7	Conclusions	94

7	Ion Beam Current Measurements and Thrust Estimation	97
7.1	Introduction	97
7.2	Theory	98
7.3	Aims	103
7.4	Apparatus	104
7.5	Methodology	105
7.5.1	Measuring the influence of changes in electrode aperture configuration on the discharge characteristics of the system	107
7.5.2	Characterising the extracted ion beam current as a function of changing electrode configuration	108
7.6	Results and Discussion	109
7.6.1	Voltage-current characteristics as a function of changing electrode aperture number and propellant flow rate	110
7.6.2	Measuring the ion beam current as a function of applied voltage and discharge current	114
7.6.3	Characterising the thruster efficiency as a function of changing aperture number	118
7.7	Conclusions	123
8	Research Summary and Conclusions	125
	References	128
	Appendix A Performance Comparison of Electric Thruster Varieties	135
	Appendix B Plasma Physics Derivations	140
	Appendix C Mass Flow Measurement System Calibration	144
	Appendix D Calculation of Beam Divergence Angle	152
	Appendix E Data and Error Analysis	155
E.1	Preliminary Experiments	155
E.2	Ion Beam Current Measurements and Thrust Estimation	166

List of figures

1.1	1U and 3U CubeSat configurations developed by California Polytechnic State University [1].	2
1.2	The total number of nanosatellites and CubeSats launched over the past 20 years. The number of Nanosats launched with a propulsion module is comparatively low. Image taken from <i>www.nanosats.eu</i> , <i>date of last access: 18/11/2021</i>	3
1.3	Schematic of the CorIon thruster principle of operation [2].	4
1.4	Schematic of the "U-shaped" DC discharge based microthruster concept [2].	6
1.5	Schematic showing the working principle of the thruster concept studied in this research. The cathode extracts the positive ions into a focused beam which creates a net momentum providing the desired thrust.	8
1.6	Summary of Research Methodology.	10
2.1	Diagrammatic representation of the atmospheric electromagnetic opacity. CubeSats would enable all-sky surveys to be conducted across portions of the EM spectrum not accessible to ground-based telescopes. Image taken from: <i>Caltech.edu</i> , <i>date of last access: 10/11/2021</i>	14
2.2	Advantages of micropropulsion systems for nanosatellite space science missions [3]	15
2.3	Proposed design of an individual 3U CubeSat for RELIC [4].	18
2.4	Schematic of the proposed RELIC mission concept consisting of a spherical constellation of 3U CubeSats forming a 1 km diameter spherical aperture. Image taken from [4].	19
3.1	Schematic showing the principle of operation of the resistojet [5].	25
3.2	Schematic showing the principle of operation of the Radio Frequency Ion Thruster. [5].	28
3.3	Schematic showing the principle of operation of the Hall Effect Thruster [5].	29

3.4	Schematic showing the principle of operation of the Electrospray Thruster [5].	31
3.5	Schematic showing the principle of operation of the Pulsed Plasma Thruster [5].	33
3.6	Characteristic temperature and density of various plasma sources [6].	37
3.7	Illustration of the Debye shielding effect. An electron cloud forms around a positive test charge q_t which effectively screens the positively charged ions.	38
3.8	Comparison of a standard Coulomb potential with a Debye screened potential.	40
3.9	Plasma slab with electrons displaced from a fixed ion background.	40
3.10	Schematic of the Coulomb interaction experienced by an electron.	45
3.11	Plasma particle densities before (a) and after (b) sheath formation at the plasma boundary. Image taken from [7].	46
3.12	The plasma and potential distribution near a material wall [8].	47
4.1	Circuit setup used to generate a glow discharge.	51
4.2	Voltage-current relationship of a glow discharge.	52
4.3	Current-voltage evolution throughout the Townsend regime.	54
4.4	Relationship between the breakdown voltage and the product of pressure and distance in a discharge tube for various gases [9].	56
4.5	Schematic showing the visual features of a low pressure glow discharge [9].	57
4.6	Spatial variation of the plasma potential from the argon glow discharge simulation.	60
4.7	Spatial variation of the argon ion number density from the argon glow discharge simulation.	62
4.8	Spatial variation of the electron number density from the argon glow discharge simulation.	63
4.9	Spatial variation of the argon mass fraction (denoted as A_{rs}) from the argon glow discharge simulation.	64
4.10	Spatial variation of the electron temperature from the argon glow discharge simulation.	65
4.11	Spatial variation of the electron, ion and total current density from the argon glow discharge simulation. The current densities are negative as the current vector and electrode surface normal are in opposite directions.	66
5.1	Geometry of the discharge tube (thruster body), end cap fittings and electrode dimensions used in this research. Note that the dimensions were measured using a vernier caliper which gives a reading error of 0.05 mm and thus the actual dimensions are accurate to ± 0.05 mm to those quoted above.	69

5.2	Dimensions of the teflon endcaps used to shield the outside of the electrodes from unwanted electrical arcing.	70
5.3	Image of the thruster mounted on the thruster stand.	70
5.4	The various electrode configurations used in the preliminary experiments. The error in the orifice diameter is estimated to be ± 0.1 mm, arising from the machining process.	71
5.5	Glass vacuum chamber used in preliminary experiments (left) and base plate design (right).	72
5.6	Stainless steel vacuum chamber used in the experimental tests proceeding the preliminary studies.	72
5.7	Vacuum pump system used to obtain an artificial space environment.	73
5.8	High voltage DC power supply used in all experimental tests conducted in this research.	74
5.9	Oscilloscope used to indirectly measure the ion beam current density.	74
5.10	Micro-controller and current sensor setup used to obtain more accurate measurements of the the discharge current.	75
5.11	Schematic and cross section through the orifice plate box used in the mass flow rate calibration process. Images taken from [10] and [2].	76
5.12	SteREO V8 microscope used to study the surface features of the electrodes after conducting the experiments.	77
6.1	Thruster concept viewed as a quintessential ion source.	79
6.2	Preliminary Experimental Setup.	83
6.3	Experimentally determined Paschen curve for argon discharge.	86
6.4	Discharge voltage as a function of current in the pressure range 0.8-0.95 Torr.	87
6.5	V-I characteristics of the 1 mm and 2 mm aperture configurations.	89
6.6	V-I characteristics of the 4 mm and 8 mm aperture configurations.	89
6.7	Average voltage (over four trials) vs discharge current for various aperture sizes.	90
6.8	Power vs discharge current for different aperture sizes.	90
6.9	Plume formation of 2 mm and 8 mm apertures at a discharge current of 6 mA.	91
6.10	Image of the electrodes taken before running the preliminary experiments. (1 mm, 2 mm, 4 mm and 8 mm aperture sizes).	92
6.11	Image of electrodes taken after conducting the preliminary experiments. Top: ground electrodes (cathodes), bottom: plasma electrodes (anodes).	92
6.12	Stereo microscopic image of the inner surface of the 1 mm aperture cathode after it was cleaned in an ultrasonic bath.	93

6.13	Stereo microscopic image of the inner surface of the 4 mm aperture cathode after it was cleaned in an ultrasonic bath. The concentric rings are an artefact of the machining process.	93
6.14	Optical microscope image of the 2 mm (left) and 8 mm (right) aperture cathodes. The scratches on the surface are artefacts of the machining process.	94
7.1	Plasma meniscus formed in a diode extraction system.	98
7.2	A single aperture cylindrically symmetric ion beam extraction system. . . .	99
7.3	Child-Langmuir law: typical current density vs acceleration voltage relationship in a diode tube.	100
7.4	AXCEL-INP simulation of an ion extraction system with three different plasma densities and a fixed potential drop across the electrodes. PE = Plasma electrode, GE = Ground electrode and $N_1 < N_2 < N_3$. Image taken from [11], p.63.	101
7.5	Experimental setup used to measure the influence of changing aperture size/number on the discharge characteristics of the thruster.	105
7.6	The setup used inside the vacuum chamber. The thruster stand was modified for easier and more secure attachment of the electrodes to the HV cables through the use of pressure contacts. Note that the teflon endcaps were eventually removed and replaced with a silicone shielding.	106
7.7	The mass flow rate measurement system setup including the in-house developed orifice plate box.	107
7.8	The experimental setup used to measure the extracted ion beam current. . .	108
7.9	Modified thruster tube geometry and the different electrode aperture configurations used in the experimental tests.	110
7.10	Thruster V-I characteristics with a 1x2 mm and 2x2 mm aperture electrodes.	111
7.11	Left: Thruster V-I characteristics with 4x2 mm aperture electrodes. Right: Average discharge current (over 5 trials) as a function of applied voltage and changing electrode aperture number.	111
7.12	V-I characteristics for the 4x2 mm aperture system at different propellant flow rates.	112
7.13	Plume formation observed at the anode when the propellant flow rate was set above 300 ng/s. The thruster did not operate stably when the propellant flow rate was set higher than this. Despite its dramatic appearance, it is hypothesised that this plume consists predominately of electrons which do not contribute significantly to thrust.	113

7.14	Image taken from the vacuum chamber viewing port of the extracted ion beam generated at the 2x2 mm aperture cathode.	114
7.15	Measured ion beam current, calculated from the voltage drop across a 0.82, 1.64 and 2.45 ± 0.01 M Ω resistor, as a function of applied voltage and discharge current across the plasma source. Note that the parallel resistance of the oscilloscope has been taken into account when calculating the beam current, see equation (7.11).	115
7.16	Measured ion beam current (obtained using a 2.45 ± 0.01 M Ω resistor) as a function of aperture number. The discharge current was kept fixed at 1.000 ± 0.001 mA and the MFR was set to $180-200 \pm 6$ ng/s.	116
7.17	The ion production efficiency vs aperture number at 1 mA discharge current.	119
7.18	The electrical efficiency vs aperture number at 1 mA discharge current. . .	120
7.19	The thrust-to-power ratio vs aperture number at 1 mA discharge current. . .	121
7.20	The cross section of the 2x2 mm electrode aperture thruster discharge tube reveals the formation of debris collected on the walls of the discharge channel. The debris may be a result of the burnt out residue from the nylon gas feed inlet thread (bottom right).	122
7.21	The formation of black debris on the outer surface of the electrodes, most likely caused by the interaction of the discharge plasma and the adhesive used to bond the electrodes to the thruster. Top: plasma electrodes. Bottom: extractor electrodes.	122
A.1	Relationship between thrust and specific impulse of various chemical and electrical propulsion systems [5].	137
A.2	Relationship between power and specific impulse of various electrical propulsion systems [5].	138
A.3	Relationship between thrust to power ratio and specific impulse of various electrical propulsion systems [5].	138
B.1	Neutral plasma containing a test charge.	140
B.2	Plasma slab with electrons displaced from the fixed ion background.	143
C.1	Orifice flow concept	145
C.2	Mass flow measurement system calibration setup.	147
C.3	Fitted calibration curve for the mass flow measurement system	150
D.1	Schematic of the beam current density profile and the beam divergence angle.	153

D.2 Colour adjusted image of the beam spot size for the 1x2 mm and 2x2 mm
extractor apertures measured at the collector plate. 154

List of tables

4.1	Plasma parameters used in Argon glow discharge simulation	59
4.2	Collisional reactions modelled in the simulation [12]	59
7.1	The relationship between the number of apertures, the average ion acceleration voltage, the measured ion beam current (from the $2.45 \pm 0.01 \text{ M}\Omega$ resistor) and the estimated thrust for a fixed aperture radius of 2 mm. The discharge current was kept constant at $1.000 \pm 0.001 \text{ mA}$ across all aperture configurations.	117
7.2	Comparison between the theoretical ion beam current I_b^{Theo} , the measured ion beam current I_b^{Exp} , as a function of changing aperture number.	118
A.1	Table showing the performance parameters for various thruster varieties . . .	136
C.1	Data obtained from the mass flow rate calibration experiment. The time taken to evacuate $15 \pm 0.1 \text{ ml}$ of argon from the burette is measured at various pressure differentials. ΔP_i is the differential pressure measured at the beginning of the evacuation and ΔP_f is the final pressure measured after the 15 ml of argon had been evacuated. All tests were conducted at an ambient temperature of $293 \pm 3 \text{ K}$, with the vacuum chamber evacuated down to $0.10 \pm 0.01 \text{ Torr}$	149
C.2	The calculated average pressure differential and corresponding average evacuation time, along with the calculated Volume Flow Rates (VFR) and Mass Flow Rates (MFR) obtained using the data from Table C.1.	150
C.3	Calculation of errors in volume flow rate and mass flow rate.	151
E.1	Raw data, with errors, used to plot the Paschen curve in Fig.6.3. Note that the breakdown voltage represented here is taken as the average over three trials.	156
E.2	Raw data, with errors, used to plot Fig.6.4. Note that the discharge voltage represented in each pressure range is taken as the average over five trials. . .	158

E.3	Continuation of data from Table.E.2	159
E.4	The calculated standard deviation of the measured voltage across five trials used to generate the error bars in Fig.6.5.	160
E.5	The calculated standard deviation of the measured voltage across five trials used to generate the error bars in Fig.6.5.	161
E.6	The calculated standard deviation of the measured voltage across five trials used to generate the error bars in Fig.6.6.	162
E.7	The calculated standard deviation of the measured voltage across five trials used to generate the error bars in Fig.6.6.	163
E.8	Raw data, with errors, used to generate Fig.6.8.	164
E.9	Raw data, with errors, used to generate Fig.6.8.	165
E.10	Standard deviation of measured discharge current across five trials, used to produce the error bars for the V-I curve for the 1x2 mm electrode aperture configuration in Fig.7.10.	166
E.11	Standard deviation of measured discharge current across five trials, used to produce the error bars for the V-I curve for the 2x2 mm electrode aperture configuration in Fig.7.10.	167
E.12	The calculated error in the measured ion beam current use to generate the error bars in Fig.7.15.	168

Nomenclature

Acronyms / Abbreviations

CorIon	Corona Ionisation
DC	Direct Current
EELV	Evolved Expendable Launch Vehicle
EP	Electric Propulsion
ESPA	EELV Secondary Payload Adapter
FEEP	Field-Emission Electric Propulsion
GIT	Gridded Ion Thruster
HV	High Voltage
MEMS	Microelectromechanical Systems
PIT	Planar Pulsed Inductive Thruster
PPOD	Poly-Picosatellite Orbital Deployer
PPT	Pulsed Plasma Thruster
RIT	Radio Frequency Ion Thruster
RTG	Radioisotope Thermoelectric Generator
V-I	Voltage-Current

Chapter 1

Introduction

1.1 Characteristics of Small Satellites

The advent of small satellites (SmallSats) has seen a substantial increase in the interest in space-related activities particularly among the private sector. These miniaturised systems allow for low cost access to space due to their reduction in manufacturing costs, small size and subsequently reduced mass, in comparison to conventional spacecraft [5]. SmallSats can be subdivided into categories based on their mass, these are [13]:

1. Microsatellites: 10-100 kg,
2. Nanosatellites: 1-10 kg,
3. Picosatellites: 0.01-1 kg,
4. Femtosatellites: 0.001-0.01 kg.

To date, the most popular type of small satellite is the CubeSat- a class of nanosatellites consisting of individual cubic modules or units. The standard unit size, referred to as 1U, of a CubeSat is $10 \times 10 \times 11.35 \text{ cm}^3$, provides 1 litre of volume and weighs roughly 1.33 kg [14]. CubeSat units can also be stacked lengthwise and deployed in 3U form factors¹, 6U and 12U form factors have also been considered [15]. They are launched as secondary payloads on-board larger launch vehicles.

¹In this context, form factor is a term used to describe the size, shape and mass of the CubeSat.



Fig. 1.1 1U and 3U CubeSat configurations developed by California Polytechnic State University [1].

Since all CubeSats are required to have the same dimensions they can be deployed into orbit using a common deployment system called a Poly-Picosatellite Orbital Deployer, or P-POD [16]. The restrictions imposed on the dimensions and mass of the CubeSat has limited the available power supply of these systems to 100 W [17]. Moreover, the size, mass and power restrictions have made it difficult to design effective on-board miniaturised propulsion systems, which in turn limits the performance capabilities of the CubeSat.

1.2 Micropropulsion Systems for CubeSats

A propulsion system is the primary mechanism responsible for the mobility of a spacecraft. It allows the spacecraft to perform altitude control as well as various orbit modifications. Despite the growing trend of nanosatellite launches in recent years, the total number of nanosatellites with an on-board propulsive mechanism has been comparatively low. This is clearly demonstrated in Fig.1.2 which shows the cumulative number of nanosats launched, over the past 20 years, in relation to the proportion of nanosats with on-board propulsion modules.

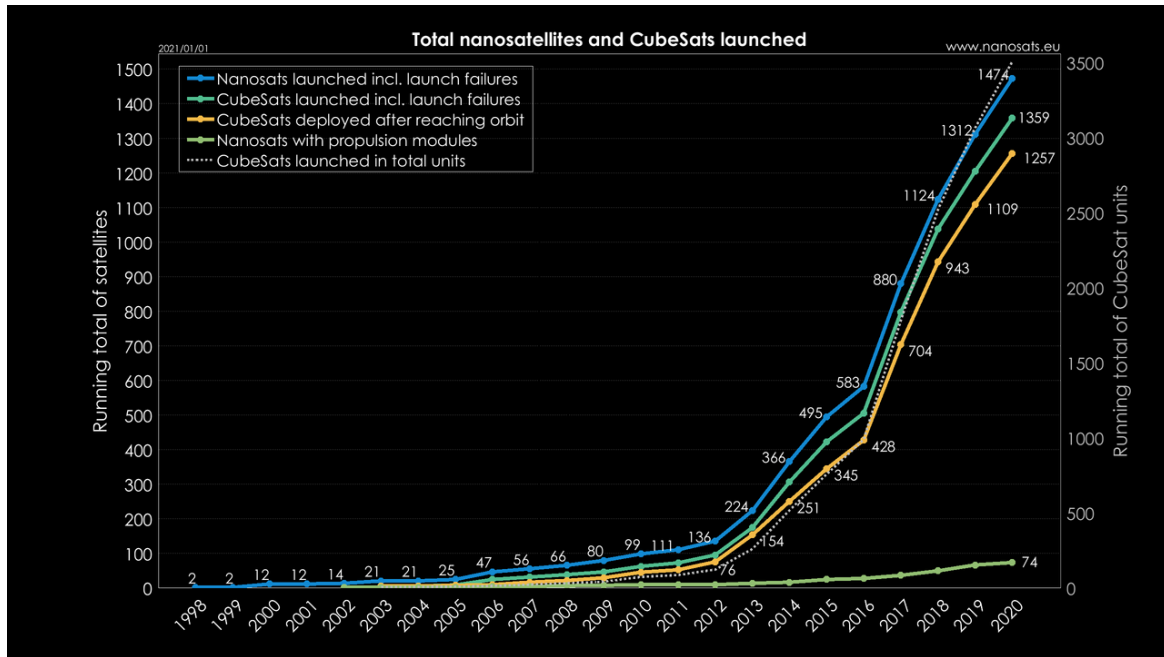


Fig. 1.2 The total number of nanosatellites and CubeSats launched over the past 20 years. The number of Nanosats launched with a propulsion module is comparatively low. Image taken from www.nanosats.eu, date of last access: 18/11/2021.

The market for nanosatellite propulsion modules is forecasted to grow significantly in the coming years, largely due to the need for on-board satellite de-orbiting capabilities [18]. In spite of numerous challenges faced when developing reliable micropropulsion modules, there has been a plethora of micropropulsion concepts that have been proposed and some already have a heritage of flying on CubeSat missions [5]. Many of these concepts have limited performance capabilities and there is still room for improvement.

Lately, there has been a growing interest in the use of electric propulsion as these systems offer low fuel consumption and high overall efficiencies [19]. One of the most popular types of electric propulsion is the Kaufman ion engine, first demonstrated in the 1960s on-board the SERT-1 spacecraft [20]. Ion engines can reach efficiencies as high as 80%, produce a fairly high thrust to power ratio and can deliver a total impulse of 10^6 Ns, over many months to years of operation. These characteristics make ion engines ideal for long duration space missions [19].

Ion engines are difficult to miniaturise due to scaling problems: at the required dimensions the ionisation chamber is smaller than the mean free path of the electrons and this prevents ionisation from occurring. The addition of magnetic fields may mitigate this prob-

lem, however, they usually add significant mass to the spacecraft. Attempts to address these issues have led to the development of propulsion systems that are void of accelerator grids and have more efficient ionisation mechanisms. One such system is the Corona Ionisation thruster (or CorIon thruster), developed by the Space Propulsion Research Lab at the University of Witwatersrand [21]. The thruster's characteristics and principle of operation are discussed below.

The Corona Ionisation (CorIon) thruster concept

The CorIon thruster utilises the phenomenon of corona ionisation as its primary ionisation and thrust mechanism. The system consists of a hollow needle, with radius $R \sim 0.1 \text{ mm}$, embedded in an insulating material (Teflon). The bipolar design utilises two needles as seen in Fig.1.3 below [21]. A gas flow system is connected at the insulated ends of the needles and feeds propellant into the needles at a specific mass flow rate. The needles are connected to a high voltage power supply. When a high voltage is applied across the needles, a corresponding high electric field is produced. This electric field ionises the gaseous propellant, via corona ionisation, as it exits the tips of the needle at the other end of the gas flow system. The same electric field then accelerates the resulting ions and electrons away from the system, generating thrust. In this way the ionisation and acceleration mechanisms are coupled. This subsequently results in a significant size and mass reduction making the system suitable for micropropulsion applications.

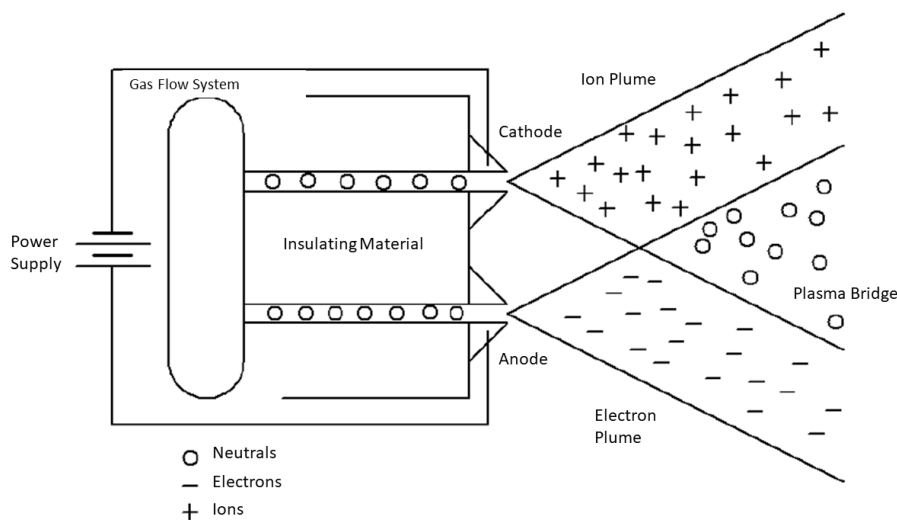


Fig. 1.3 Schematic of the CorIon thruster principle of operation [2].

Experimental testing on the system found that only a small fraction of neutral propellant had been ionised through collisions with electrons. Nevertheless, the propellant utilisation was observed to be significantly larger than the ionisation rate, implying that the small fraction of ionised neutrals had efficiently imparted momentum to the remaining neutrals [22]. This led to a higher plume velocity, predominantly consisting of neutral particles. Partial ionisation is advantageous as it results in a lower power requirement. Further details on the CorIon concept, as well as the results from preliminary tests on the thruster, can be found in [21] and [22].

Despite its numerous advantages, the CorIon thruster suffered many drawbacks [2]:

- In its current form, it is highly unstable. The needles small size means that a high power density is produced at the tip during the ionisation process. The resulting ions impact the needle tips with high energies causing sputtering to occur, leading to a high erosion rate.
- The erosion alters the shape of the needle tips, which affects the electric field and gas flow characteristics of the system. This subsequently changes the plasma characteristics and alters the system's performance. These problems led to a reduction in both the operational lifetime of the thruster and the repeatability of experiments.
- The CorIon thruster utilises gaseous propellant, from a high-pressure propellant tank, which significantly increases the overall mass of the system. Moreover, the amount of gaseous propellant available to the thruster for ionisation is severely limited by the maximum pressure restrictions imposed on CubeSats (i.e. pressure vessels on CubeSats cannot exceed 1.2 bar [14]). These drawbacks extend to all propulsion systems that utilise pressurised propellant as fuel source.

Modifications to the CorIon thruster concept

Attempts to address the shortcomings of the CorIon thruster led to the development of a similar thruster concept which was inspired by the conventional glow discharge tube.

A conventional glow discharge tube consists of an insulating container enclosing a low pressure gas with two electrodes, placed at opposite ends of each other, connected to a high voltage power supply. Initially, electrons are emitted from the cathode through photoionisation. When a high voltage is applied across the electrodes an electric field is set up which accelerates the electrons towards the positively charged anode. As the electrons gain

sufficient kinetic energy they begin to ionise the gaseous atoms and produce electron-ion pairs (a Townsend avalanche forms [9]). The discharge becomes self sustaining when the ions are accelerated towards the cathode where they impact the cathode's surface and release secondary electrons. Different discharge regimes are obtained by varying the potential applied between the electrodes. These discharge regimes would allow for various operating modes on a potential thruster. Furthermore, conventional discharge tubes have been shown to operate in the stable glow regime for thousands of hours and thus a DC discharge based thruster offers the potential for good lifetime and repeatability characteristics [23].

For the discharge tube to be adapted into a working thruster, the tube needs to have both its ends open to the vacuum of space to allow for particles to be ejected outwards for thrust and for the overall ejected charge to be neutral. By exploiting the characteristics of the plasma produced from the discharge, the tube can be constructed into a wide range of different geometries. The author in [2] decided to use a cylindrical "U-shaped" bipolar design as shown in Fig.1.4 below:

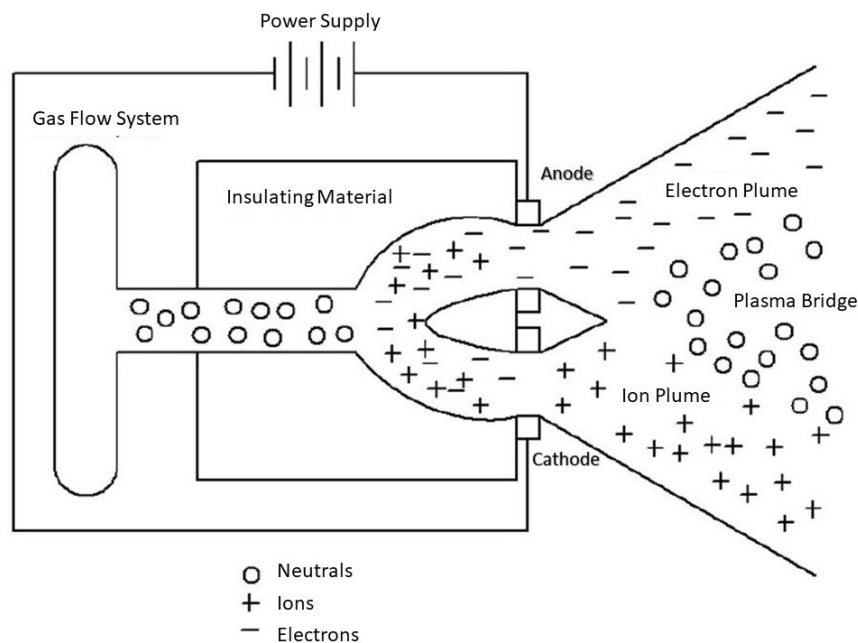


Fig. 1.4 Schematic of the "U-shaped" DC discharge based microthruster concept [2].

The system was hypothesised to produce a plasma in a similar way to a discharge tube. In this case, two ring-shaped electrodes, placed at the ends of the thruster, are open to the vacuum of space. The electrodes are connected to a high voltage power supply and when turned on produces an electric field along the channel of the tube. The electrons and ions

from the plasma are attracted to the anode and cathode respectively and are accelerated outwards producing the necessary thrust. This thruster design shares many common elements with the CorIon thruster: it consists of a gas flow system that feeds propellant into the tube, it utilises a coupling of ionisation and acceleration mechanisms and, it is hypothesised that the electrons and ions leaving the thruster should neutralise each other upstream, producing a plasma bridge [2]. In this way the "U-shaped" thruster design was expected to retain all of the positive characteristics of the CorIon system with the added benefits of a longer operational lifetime and greater repeatability.

Preliminary tests conducted on the thruster aimed to measure its behaviour under different operating parameters. These tests included: measurements of the lifetime and repeatability characteristics, measurements of the thrust production, and plasma diagnostic measurements used to understand the behaviour of the discharge plasma. Although the "U-shaped" thruster had demonstrated an improved lifetime in comparison to the CorIon system, many of the experimental tests had produced results contrary to the thruster's hypothesised mechanism of operation. Further details on this work can be found in [2].

Proof-of-concept DC glow discharge microthruster

Prior to testing the "U-shaped" thruster design, a proof-of-concept straight discharge tube was tested to ascertain whether the proposed concept would in fact work as a plasma propulsion system. In this case the discharge tube was a straight cylinder with ring-shaped electrodes at either end opened to the vacuum of space. The proof-of-concept was able to operate stably for a much longer time (> 5 hours) than the "U-shaped" thruster, showed very little damage to the electrodes in comparison to the "U-shaped" thruster, and passed repeatability tests with only small parameter fluctuations (as opposed to the "U-shaped" thruster which exhibited larger fluctuations in the measured parameters during repeatability tests). Unfortunately, the proof-of-concept was not studied in further detail as Wright [2] was mainly interested in the "U-shaped" thruster design.

From the preliminary tests on the proof-of-concept, plasma plumes formed and were observed at both of the open ends of the tube. It is hypothesised that the plume formed on the anode end of the tube will mostly consist of electrons which are attracted to the positive electrode, meanwhile the plume at the cathode end will predominantly consist of positive ions, generated from the ionisation of the gaseous propellant. Since the electrons have a significantly lower mass in comparison to the ion mass, the thrust produced by the electron plume should be negligible, hence the net thrust will cause the spacecraft to move in the

opposite direction to that of the ejected ions. Fig.1.5 illustrates this concept.

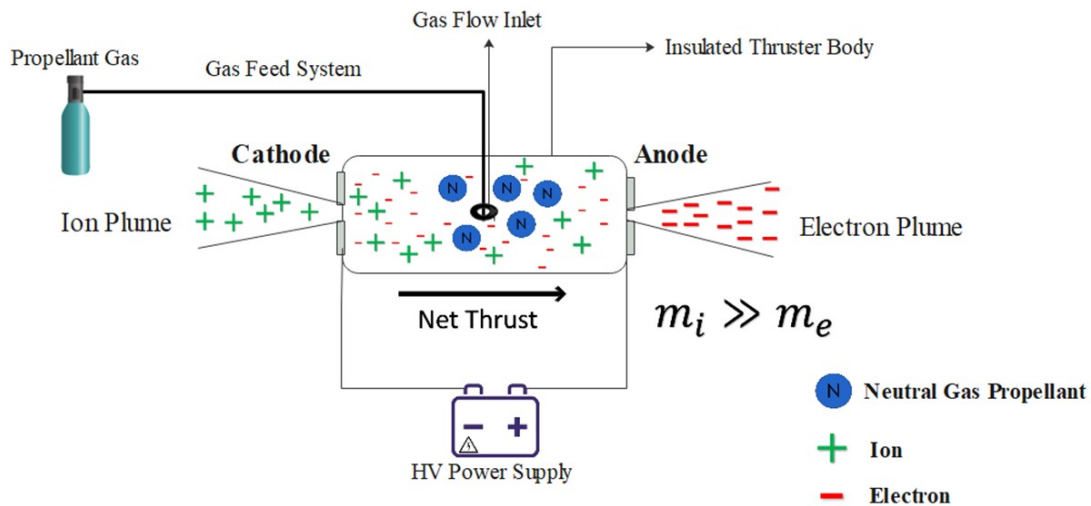


Fig. 1.5 Schematic showing the working principle of the thruster concept studied in this research. The cathode extracts the positive ions into a focused beam which creates a net momentum providing the desired thrust.

Considering the positive observations associated with the proof-of-concept, the natural question arose as to whether the proof-of-concept straight discharge thruster could itself be adapted into a working micropropulsion system. Hence the motivation for conducting further studies on this system configuration. The results of which are presented here.

1.3 Research Objectives

The general goal of this research will be to conduct a detailed study and perform further testing on a straight DC discharge based microthruster, to determine if it is a viable option for a propulsion system, to be used on future CubeSat science missions. The following list highlights the specific objectives of this research:

- To design and construct a straight DC discharge microthruster, similar to the proof-of-concept, using a ceramic as the material for the thruster body.
- To verify whether the thruster concept works as hypothesised - according to the ionisation-acceleration coupling mechanism.

- To deduce an optimal set of operating parameters for a stable discharge and thruster operation.
- To investigate the effect of changes in electrode aperture size and number on the electrical (voltage-current) characteristics of the system.
- To investigate the effect of changes in electrode aperture size and number on the total ion beam current emanating from the thruster.
- To produce estimates of the system's thrust and efficiency based on the measured values.

1.4 Research Methodology

The discharge characteristics within the thruster plays a crucial role in determining the total ejected ion current. This subsequently influences the total thrust generated by the system. Many satellite missions implement orbital maneuvers that require specific amounts of thrust to be produced at set periods of time. It is therefore important to develop a thruster that operates stably and produces repeatable results when the same set of operating parameters are applied as even small variations may lead to disastrous implications, including complete mission failure.

This research was therefore conducted in three parts:

1. Preliminary studies were done, within a smaller vacuum chamber, to verify the system's hypothesised operating mechanism and to identify the optimal parameters: like the optimal working gas pressure, the optimal electrode aperture size and related voltage-current characteristics required for stable operation in a given thruster geometry.
2. Further testing was then conducted, in a larger vacuum chamber, to determine the effects of changing the thruster configuration (i.e the electrode aperture size and number) and measuring the system's electrical characteristics in each case. These experiments also aimed to characterise the magnitude of extracted ion current under different system configurations.
3. Finally, the data obtained from the extracted ion current measurements, along with the data of the system's electrical discharge characteristics, were used to produce estimates for the system's thrust and overall efficiency.

Fig.1.6 below summarises the general methodology used in this research. The exact details of each step will be discussed in subsequent chapters.

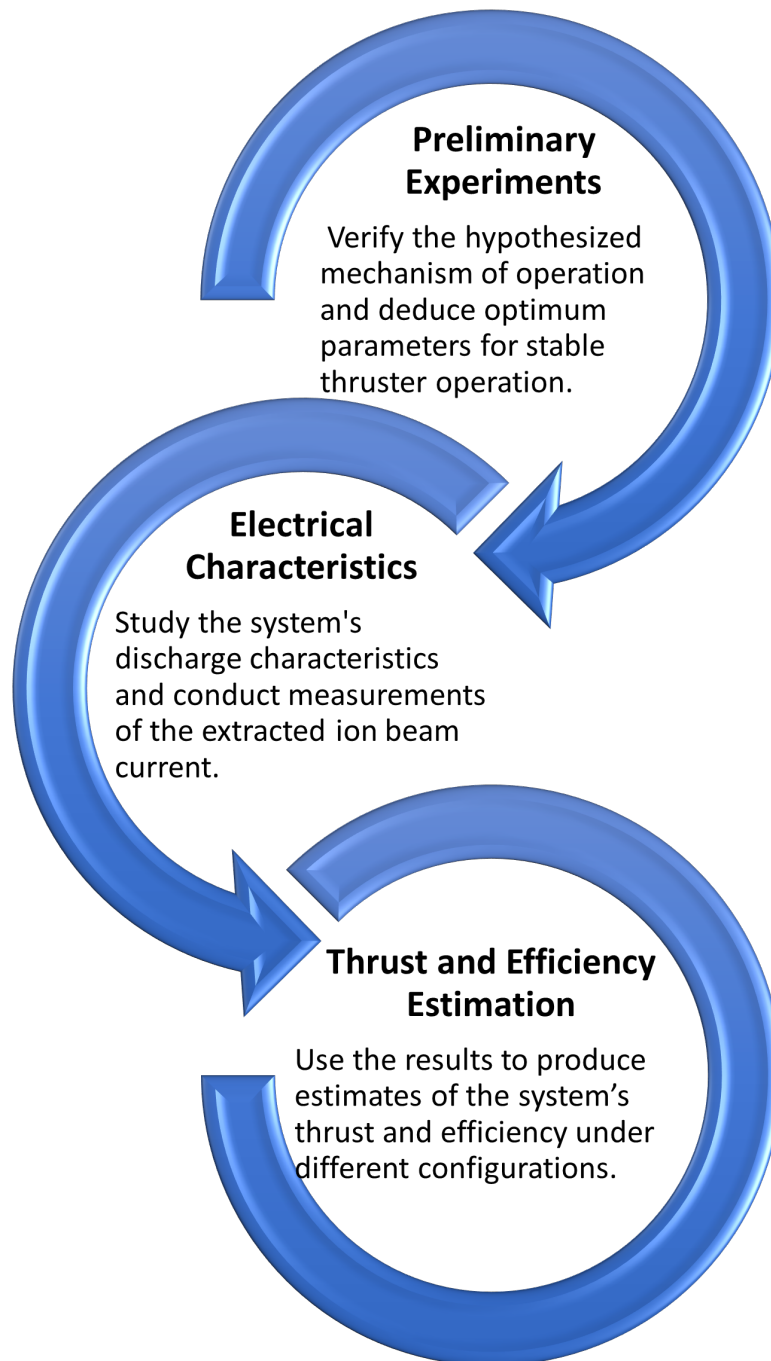


Fig. 1.6 Summary of Research Methodology.

1.5 Dissertation Structure

An outline of the dissertation is provided below:

- Chapter 2 begins with a discussion on the contribution of this research to the field of particle cosmology (i.e the study of the interface between elementary particle physics and physical cosmology). In particular, it covers the various CubeSat mission concepts that can enable new discoveries for particle cosmology and the role that micropropulsion systems can play in realising these mission concepts.
- Chapter 3 contains a survey of the relevant literature and includes a brief discussion of the principles of propulsion, the important performance metrics used to assess propulsion systems, along with an overview of the various electric microthruster concepts currently in use or under development. This chapter also contains a discussion of the basic plasma physics required to understand the working mechanism of the proposed thruster concept.
- Chapter 4 provides a detailed description of glow discharge physics including a 1D simulation of an argon glow discharge used to develop insights on the variation of plasma parameters along the axis of the thruster's discharge channel.
- Chapter 5 presents the materials and apparatus used in all experimental tests.
- Chapters 6 and 7 contains the results obtained from the preliminary tests, along with results from measurements of the thruster's electrical characteristics and the extracted ion beam current. Chapter 7 ends with a discussion on the relationship between the estimated thrust and efficiency as a result of changing the system's configuration. All data obtained from experiments along with a detailed error analysis is provided in Appendix E.
- Chapter 8 gives an overall evaluation of the research, including the main findings and recommendations for future work on the system.

Chapter 2

CubeSat Micropropulsion- Enabling Breakthroughs in Particle Cosmology

2.1 Introduction

In 2009, the European Space Agency (ESA) launched the Planck space observatory which produced a higher resolution and higher accuracy map of the temperature fluctuations in the CMB in comparison to its predecessor WMAP [24]. The Planck mission had established precise measurements of several key cosmological parameters, including the average densities of dark matter and ordinary matter as well as the approximate age of the universe [24]. Sophisticated space observatories, like Planck, take many years to develop, have high risks of technical failure and are extremely expensive.

The recent surge in CubeSat development has led to significant advancements in micro-electromechanical systems (MEMS) detectors that are compatible with the nanosatellite platform [3]. Additionally, compact radio frequency transmitters, in both the X-band (8-12 GHz) and the Ka-band (26-40 GHz), are becoming more readily available. These compact RF transmitters have the potential to extend the downlink data rate to >100 Mbps [3]. These advancements, coupled with improvements in terrestrial digital processing, are providing the key technological requirements for in-space astronomical observatories on the nanosatellite platform.

There are two major factors that make CubeSats highly appealing for conducting astronomical research [4]:

- They can be developed in a relatively short period of time (it usually takes 18-24 months to go from mission conception to realisation).
- Since CubeSats can be manufactured using commercial off the shelf components, they can be built for a fraction of the cost of larger spacecraft and can thus meet strict budget requirements.

Furthermore, the reduced cost of launching lower mass payloads makes in-situ space research more accessible to developing nations, like South Africa, and affords the opportunity for university students to engage directly in the building and launching of satellites [1]. This will likely increase the public interest in space science and contribute towards the growth of a knowledge-based economy.

In addition to the technologies mentioned above, a reliable and energy efficient on-board micropropulsion system is foreseen to be a prerequisite for many of these future in-space observatories. The reasons for which will be elaborated on more in this chapter. The main motivation driving the use of CubeSats to conduct research in astrophysics will be presented. Examples of current CubeSat missions, as well as novel mission concepts, aimed at addressing fundamental questions in particle cosmology will be discussed. The chapter ends with concluding remarks and justifies the contribution of this research to the field of particle cosmology.

2.2 Motivation for utilising CubeSats to conduct research in particle cosmology

The major criticisms directed towards the use of CubeSat based astronomy mainly revolve around the need for large apertures, high precision pointing stability and sophisticated cryogenic detectors which are, at the time of writing this, incompatible with the nanosatellite platform [4]. However, a study conducted by the Keck Institute for Space Studies (KISS) [4] had identified various survey missions that would be more suited towards utilising constellations of CubeSats rather than a typical singular large telescope. These missions would allow for continuous all-sky surveys across a greater portion of the electromagnetic spectrum (see Fig.2.1) and have the potential to resolve fundamental questions in astrophysics and particularly particle cosmology [4].

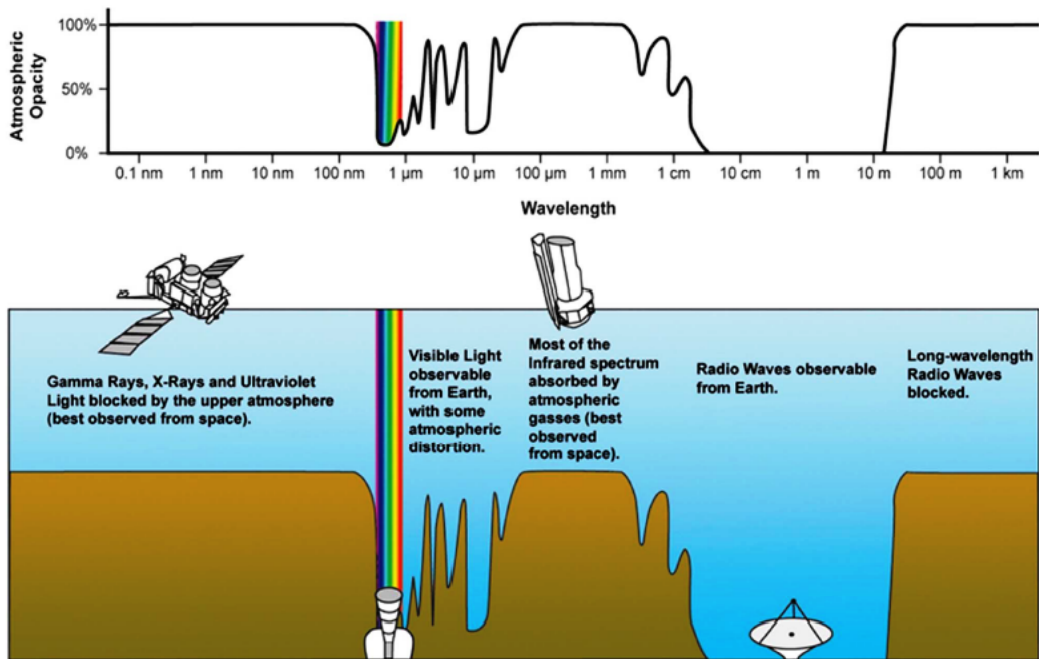


Fig. 2.1 Diagrammatic representation of the atmospheric electromagnetic opacity. CubeSats would enable all-sky surveys to be conducted across portions of the EM spectrum not accessible to ground-based telescopes. Image taken from: *Caltech.edu*, date of last access: 10/11/2021

There are a number of notable advantages that CubeSat astronomical observatories could afford, namely [25]:

- The CubeSat design specifications facilitate a streamlined delivery of instrument payloads to space.
- Mission designers have the freedom to tailor CubeSat orbits to meet observational needs and can quickly reschedule observations to respond to transient phenomenon (i.e. extremely short-lived astrophysical events).
- The growing commercial interest in CubeSats has resulted in a thriving supply chain subsequently making commercial-off-the-shelf (COTS) components, including power systems, solar panels and reaction wheels, more accessible.
- The increased commercial interest has also led to reduced costs for components which allows for a greater portion of the budget to be spent on developing the payload, including the on-board scientific instrumentation.

In addition to the advantages listed above, the authors of [25] also note that an improved spectral, temporal, and spatial coverage of astrophysical targets, relative to a single large

telescope, can be enabled using CubeSat constellations or swarms. The CubeSats can also be used solely for technology demonstration purposes without making any scientific observations. These technology demonstrations may allow for risk mitigation and could increase the technology readiness level of various spacecraft components (for example: detectors, optical sub-assemblies, actuators and micro-controllers) that would be crucial for future mission success.

2.3 Enhancing mission capabilities with on-board micropropulsion systems

A spacecraft generally consists of multiple subsystems including: a propulsion system, a thermal control mechanism, power generation and power distribution systems, telemetry command and control mechanisms, transmitters/antenna, computers and on-board processing units [26]. These subsystems are required to work synergistically to ensure mission success. In the context of small satellites, the propulsion system is of much interest as it affords the spacecraft the ability to perform various maneuvers like: altitude control, station keeping and formation flying. These characteristics are particularly important for astrophysics observations that would require nanosatellite constellations to produce large distributed apertures for greater sensitivity or resolution. Fig.2.2 provides an overview of the main advantages associated with having an on-board propulsion system.

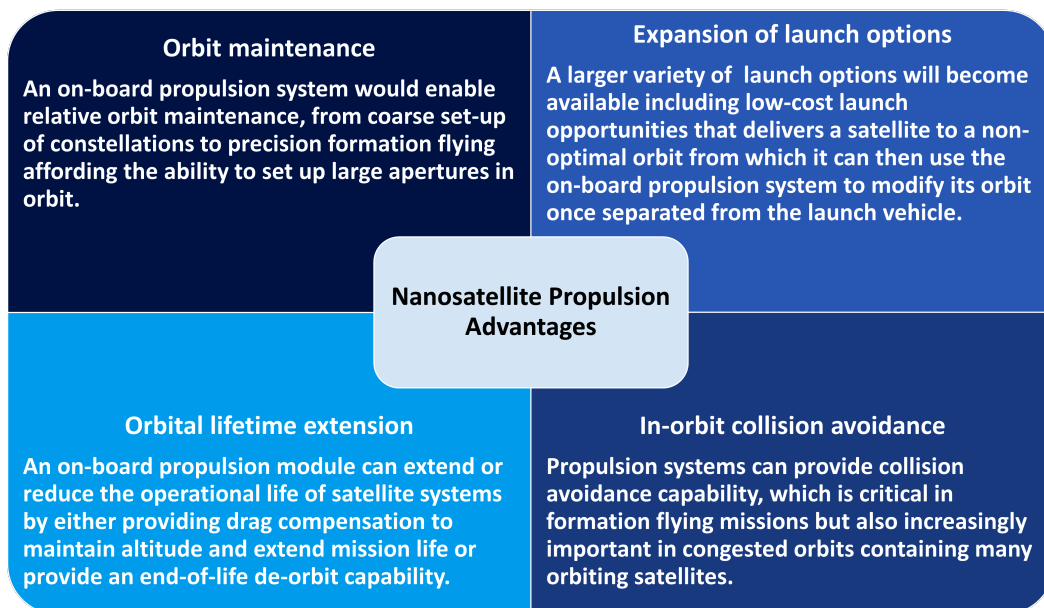


Fig. 2.2 Advantages of micropropulsion systems for nanosatellite space science missions [3]

2.4 CubeSat mission concepts for particle cosmology

A number of nanosatellite missions aimed at answering fundamental questions related to particle cosmology have already been launched [25]. The most notable among these is the HaloSat (deployed from the ISS in July 2018 [27]) and the Cosmic X-Ray Background Nanosatellite (CXBN) mission whose successor CXBN-2 was launched in 2012 [25]. In addition to these missions, a number of proposed nanosatellite missions have been put forth by the Keck Institute of Space Studies, for example; the UVIP-UV Re-ionisation probe, SoftX and RELIC [27]. A brief description of the mission requirements and research goals for two of these mission concepts, namely: HaloSat and RELIC, will be provided in this section.

2.4.1 HaloSat: The search for mission baryons

Background

Observations of minute temperature fluctuations in the Cosmic Microwave Background (CMB) had shown that nearly 5% of the universe is composed of ordinary baryonic matter [24]. Until recently, cosmologists could only account for about half of this baryonic matter. This had been an open question in cosmology and was dubbed, "the missing baryon problem." An example of this can be seen in the Milky Way, where a large discrepancy exists between the theoretically estimated baryonic mass of the Milky Way in comparison to the observed baryonic mass in the stars and disk gas (see [28] and [29]) indicating a large fraction of missing baryons. Attempts to better understand the missing baryon problem had led to the deployment of the HaloSat mission, which was the first astrophysics-focused NASA funded CubeSat mission [27], in 2018.

Scientific goals

The HaloSat mission aimed to map soft X-ray oxygen line emission across the Milky Way's halo (which covers the entire sky) in the hopes of constraining the mass and spatial distribution of the hot gas in the Milky Way [27]. The primary goal of the mission was to determine if this hot gas, which is gravitationally bound to galaxies, contributes significantly to the cosmological baryon budget. In addition to its primary goal, the HaloSat mission also had a secondary science goal of conducting observations on solar-wind charge exchange (SWCX) emissions. These observations were required to reduce uncertainties in the oxygen line emission measurements.

Mission design

HaloSat aimed to survey roughly 75% of the sky with an angular resolution of at least 15° [27]. It utilised three miniaturised detectors with each detector having an effective area of roughly 5.1 mm^2 for 600 eV X-rays and a field of view of approximately 100 degrees squared. In the context of diffuse emission observations, the grasp, which is given by the product of the effective area of the detector and the detector field of view, is used as an important measure of merit. For 600 eV X-rays, the total grasp of HaloSat was roughly two times greater than the Chandra X-ray observatory was at launch. This demonstrates how CubeSats can compete with larger space-based observatories when used to conduct specific science goals involving efficient all-sky surveys [27]. For an extensive overview of the HaloSat mission, including results from early observations, refer to [27].

It is worth noting here that, in 2021, cosmologists had determined that $\sim 50\%$ of the baryonic matter is located outside dark matter haloes, in the space between galaxies. This has been supported by observations (see [30]). Along with the total baryonic mass inside and surrounding the galaxy, the total number of baryons is now compatible with early universe measurements. Thus, the missing baryon problem has been resolved [31]. Nevertheless, follow up measurements are needed to support the leading observations.

2.4.2 RELIC: Characterising energy transport from black holes

Background

The long wavelength, low frequency radio regime ($< 10 \text{ MHz}$), is an interesting band for studying the underlying mechanisms of particle acceleration in active galaxies [4]. Unfortunately, this portion of the EM spectrum is inaccessible to ground based telescopes since the atmospheric opacity reaches 100% for radio frequencies lower than 10 MHz [32] (see Fig.2.1). Therefore, probing such low frequency radio emissions requires space-based observatories. In 2012, a novel astrophysics CubeSat mission concept called RELIC was put forward to address this issue [4].

Scientific goal

The main objective of the RELIC mission is to image double lobbed active galaxies, to map the low frequency radio emissions from active galactic nuclei (AGN), with the intent of gaining deeper insights on how energy is transported from black holes to the intergalactic

medium [4]. The RELIC mission would form an integral part in multi-wavelength studies aiming to understand the underlying physical processes occurring within active galaxies [32].

Mission design

The concept proposes a constellation of thirty 3U CubeSats, all flying in a spherical formation, where the minimum separation distance between each satellite is kept smaller than the wavelength of the 5 MHz radio signal. The spherical constellation would create a synthetic aperture with a sensitivity and angular resolution that would be sufficient to probe the regions of low frequency radio emission in AGNs [4]. Each CubeSat, within the constellation, would consist of a single dipole antenna along with a low frequency receiver [4]. An on-board propulsion module would be required for station keeping and formation flying. Located at the centre of the spherical constellation is a larger, higher power consuming, host satellite (or 'mothership') which intercepts the signals from the orbiting CubeSats. The host satellite performs the necessary signal processing, for example through cross correlation, to produce the desired images and is responsible for the direct transmission of the data back to Earth.

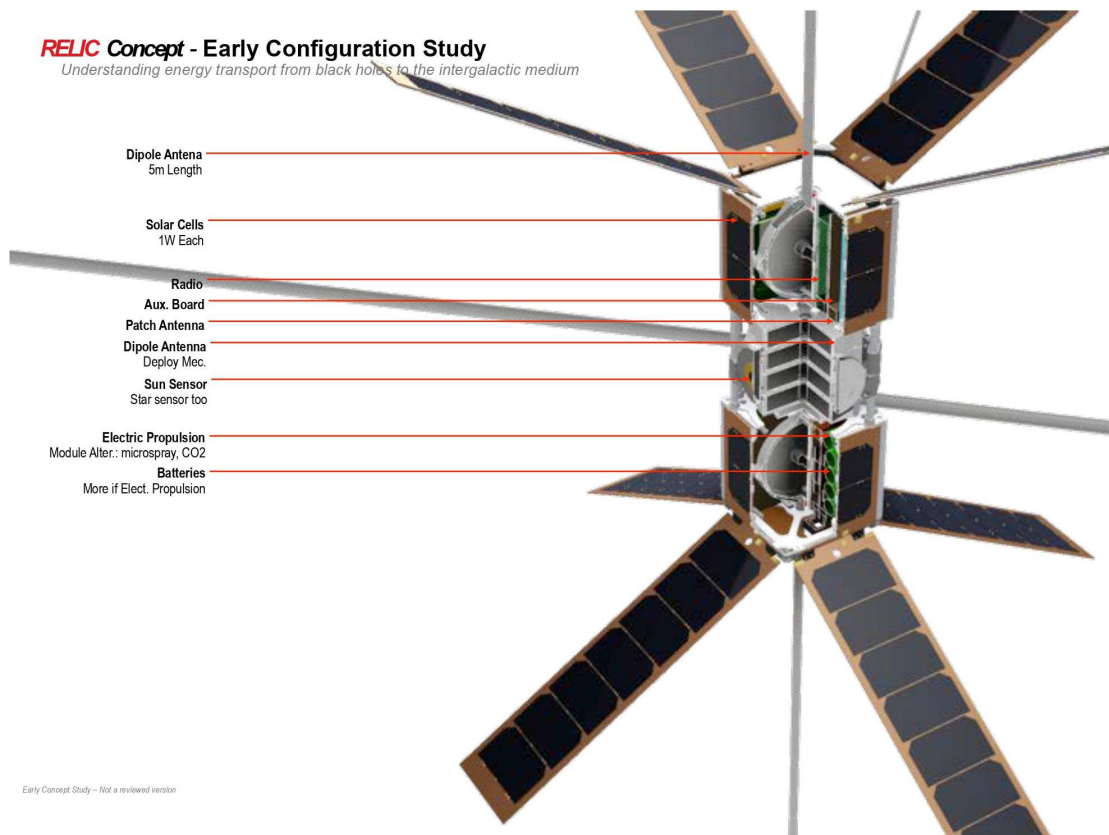


Fig. 2.3 Proposed design of an individual 3U CubeSat for RELIC [4].

Fig.2.4 shows a schematic of the proposed RELIC mission design. The mission is expected to be launched as an EELV Secondary Payload Adapter (ESPA) spacecraft. Each ESPA spacecraft has the potential to support the deployment of up to sixty 3U CubeSats [4]. The CubeSats should be deployed in a radio quiet zone far from the magnetic field of the earth to prevent radio interference, to minimise potential torque disturbances and to minimise propulsion requirements for station keeping. More details on the engineering considerations and the key technological advancements required for successful mission implementation can be found in [32] and [4] p. 68-71 .

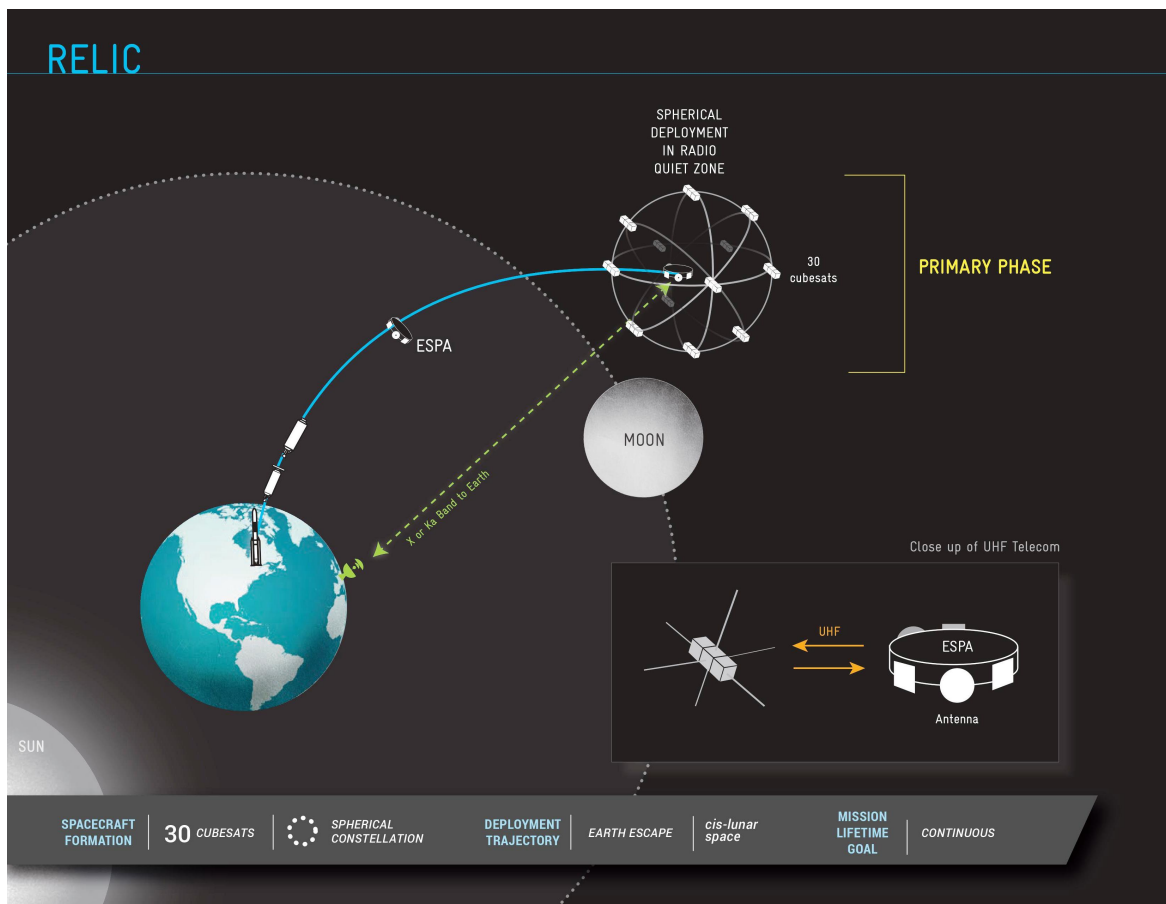


Fig. 2.4 Schematic of the proposed RELIC mission concept consisting of a spherical constellation of 3U CubeSats forming a 1 km diameter spherical aperture. Image taken from [4].

2.5 Conclusions

Studies have identified various scientific advances that can be enabled through the use of the nanosatellite platform [4]. These missions will incorporate new approaches to observation, such as continuous all-sky observing coverage and the deployment of spacecraft constellations, more suited to smaller platforms (like CubeSats). There is also the benefit of a lower risk of complete mission failure when multiple systems are deployed [4]. Exploiting the small satellite platform would allow for rapid and cost effective means to make important scientific breakthroughs, they can also complement larger missions by making collaborative observations and conducting secondary science experiments [25].

In observational cosmology, the small satellite platform provides the potential for continuous all-sky measurements, requiring multipoint observations, to be made in the low frequency (radio) and ultraviolet end of the electromagnetic spectrum [4]. These observations cannot be made using ground based observatories. Moreover, constellations of small satellites can be deployed to form distributed large synthetic aperture systems and, with advancements in distributed processing, high resolution measurements can be made. One of the major technological hurdles preventing the realisation of these mission concepts is the development of reliable micropropulsion systems. An on-board propulsion system will be crucial for all of the above mentioned concepts to be successful. The goal of this research is to develop such a system that is both reliable and versatile to propell the manifestation of these mission concepts forward, and to open up new frontiers in particle cosmology.

Chapter 3

Literature Survey

As highlighted in the previous chapter, an on board propulsion system can equip nanosatellites with a means to perform complex maneuvers, which can improve their operational capabilities and extend their in-service lifetimes (Fig. 2.2). This chapter gives an overview of the principles of propulsion, including the major performance metrics used to assess the feasibility of a propulsion system for performing specific mission objectives. Thereafter, various electric microthruster concepts are presented and the advantages and drawbacks associated with each concept is discussed. Lastly, a brief discussion on the basic plasma physics, essential for understanding the underlying mechanism of operation of the modified DC discharge microthruster concept, is presented.

3.1 Fundamentals of Propulsion

Modern propulsion systems can be broadly classified into two categories: electric and non-electric systems. Conventional chemical propulsion systems differ from electric propulsion systems by means of energy supply for the acceleration of propellant mass. In chemical systems this energy is stored in the molecular bonds of the propellants and is released through combustion, decomposition or expansion [33]. In contrast, electric systems utilise an external energy source for exhaust acceleration. In the majority of electric propulsion systems this energy is sourced from solar panels, however, electrical power can also be supplied from nuclear reactors or Radioisotope Thermoelectric Generators (RTGs) [33].

Although rockets may differ in the type of propulsion mechanism utilised, they all operate principally by Newton's third law of action and reaction forces. In essence, all propulsion systems are analysed using four main performance parameters [5], these are: the rocket's thrust T , specific impulse I_{sp} , change in velocity, or delta-v Δv and its overall efficiency

of converting energy into motion η . These parameters will be discussed in greater detail below and will be used to draw performance comparisons between various micropropulsion concepts in the next section.

Thrust

Thrust, produced from a propulsion system, is the main force responsible for a spacecraft's motion. As mentioned earlier, the thrust a rocket experiences is due to Newton's action-reaction law- arising from the propulsion system. The engine does work on the propellant ejecting it from the spacecraft, to produce a net force. The rocket is accelerated, through a momentum exchange, in the opposite direction to the force produced by the ejection of the propellant fuel. A spacecraft's thrust is an important parameter used to assess its suitability for a particular mission. A propulsion system that can only produce minuscule amounts of thrust cannot be used to deliver payloads from the Earth's surface into space, where such a system would be more beneficial for some in-space low-thrust applications.

The total thrust that a spacecraft generates is a combination of momentum thrust and pressure thrust [5]. The momentum thrust is dependent on the mass flow rate of the accelerated propellant/ ions \dot{m} and the effective exhaust velocity v_e . The pressure thrust depends on the exit area A_e - where propellant is ejected from the thruster, the exit pressure P_e and the ambient pressure P_a . The ambient pressure refers to the pressure of the environment surrounding the spacecraft and is zero in vacuum conditions:

$$T = \dot{m}v_e + (P_e - P_a)A_e. \quad (3.1)$$

Specific Impulse

The specific impulse I_{sp} is defined as the total momentum change produced per unit of propellant consumed [2]. It gives an indication of the efficiency of propellant usage. For a constant thrust and propellant flow rate, the specific impulse of a rocket can be calculated from the ratio of a rocket's thrust to its propellant consumption or input propellant flow rate (\dot{m}_p):

$$I_{sp} = \frac{T}{\dot{m}_p g} = \frac{v_e}{g}, \quad (3.2)$$

where g represents the gravitational acceleration and v_e is the rocket's effective exhaust

velocity. The exhaust velocity is defined as the velocity of the propellant exiting the rocket. In practice, the *actual* exhaust velocity can only be determined experimentally and differs from the effective exhaust velocity, which is used primarily as a measure of a thruster's efficiency. A high exhaust velocity is desirable for missions that require a high delta-v.

Delta-v

The spacecraft delta-v is a measure of the impulse per unit of spacecraft mass that is required to perform a maneuver, or more commonly: the maximum change in velocity of the spacecraft, ignoring other external forces [19]. It can be obtained from the well known Tsiolkovsky rocket equation which relates the spacecraft's maximum change in velocity to its exhaust velocity v_e , its initial mass m_i and final mass m_f after a propulsive maneuver has been performed [5]:

$$\Delta v = v_e \ln \left(\frac{m_i}{m_f} \right) \rightarrow m_i = m_f \exp \left(\frac{\Delta v}{v_e} \right). \quad (3.3)$$

The rocket equation demonstrates that high delta-v missions require substantially more fuel and thus a greater propellant mass is required to accelerate the spacecraft to a high final speed. This can be mitigated by using propulsion systems that generate high exhaust velocities which would in turn require less propellant mass, and consequently, a reduced spacecraft launch mass to reach reasonably high final speeds.

Thruster Efficiency

In general, the overall efficiency of a propulsion system η can be obtained from the fraction of source power P_s that is converted to kinetic power at the exhaust P_{jet} [33]:

$$\eta = \frac{P_{jet}}{P_s} = \frac{T^2}{2\dot{m}P_s}. \quad (3.4)$$

Here P_s represents the total input power, which could be the energy released from chemical bonds (for chemical propulsion systems) or the energy supplied by an external power source (for electric propulsion systems). Chemical and electric propulsion systems exhibit different scalability and performance properties [33]. In general, electric propulsion systems have limited electrical power and thus produce significantly less thrust than chemical propulsion systems. In contrast, since the exhaust velocity of electric propulsion systems are far greater than that of most chemical propulsion systems, electric propulsion systems display higher

efficiencies and can reach higher speeds when operating over long periods of time. In essence, there is a trade-off between specific impulse and thrust [19].

Although chemical propulsion has its place as a viable option for small satellite propulsion, especially with the recent development of thrusters utilising environmentally-friendly, high performance propellants, in exchange for the commonly used toxic hydrazine propellant, electric propulsion systems are better suited for long duration space science missions for the reasons highlighted above. As such, the discussion in the following section will focus exclusively on electric micropropulsion concepts. For more information regarding chemical micropropulsion concepts, developed and tested on CubeSats, see [5]

3.2 Electric Micropropulsion Concepts

Electric propulsion systems have been implemented extensively, by space agencies across the globe, to carry out various missions involving cutting-edge science. At the time of writing, the most notable missions include: the retrieving of asteroid samples (JAXA's Hayabusa 2 and NASA's OSIRIS-REx missions [34],[35]) and testing the technologies required for the Laser Interferometer Space Antenna (LISA) to be used for a future in-space gravitational wave observatory [36].

Although electric propulsion systems have worked well on larger spacecraft, their miniaturisation to smaller platforms has proven quite challenging. This is mainly due to the power limitations imposed on small spacecraft, resulting from decreases in solar panel area and battery sizes as the satellite's mass decreases. The typical power available to a nanosatellite ranges from 2.5 to 100 W [33]. The amount of power available to a satellite has an implication on its propulsive capabilities, including the choice of thruster and its subsequent performance.

Types of electric thrusters

Existing electric propulsion systems can be grouped into three main categories based on their acceleration mechanism, these are [19]:

1. Electrothermal thrusters
2. Electrostatic thrusters
3. Electromagnetic thrusters

3.2.1 Electrothermal thrusters

In electrothermal engines, the propellant gas is electrically heated causing it to expand from the subsequent increase in pressure. The thermal energy from the expanding gas is converted into kinetic energy, as the energised propellant mass is forced out through a nozzle which provides the desired thrust [37]. The resistojet is an example of an electrothermal thruster.

Resistojet

A resistojet operates by passing its propellant through a heating element and allowing the heated gas to be expelled through an expansion nozzle. The gas leaves the nozzle at a relatively high temperature, leading to an increase in the thruster's specific impulse in proportion to the square root of the stagnation temperature. Laboratory tests have demonstrated that micro resistojets can produce exhaust velocities of approximately 2.2 km/s [38], however, their performance is limited by the melting temperature of the heating element in use. Despite this, well designed resistojets can exhibit high thruster efficiencies (ranging from 65- 90 % [39]).

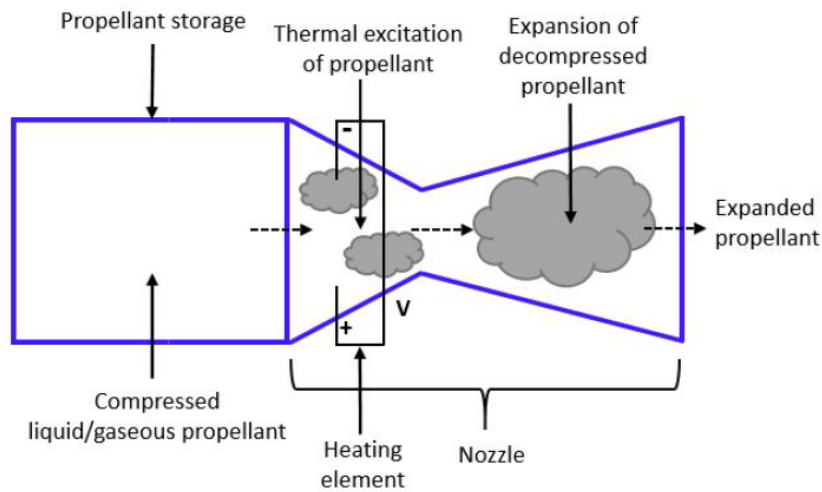


Fig. 3.1 Schematic showing the principle of operation of the resistojet [5].

The thrust and specific impulse of the resistojet can be obtained from the following relations [40]:

$$T = A_0 \left(\frac{n_0 k T_0}{2} \right) \chi, \quad (3.5)$$

$$I_{sp} = \sqrt{\frac{\pi k T_0}{2m}} \frac{1}{g_0}, \quad (3.6)$$

where T represent the thrust, n_0 is the number density of propellant atoms (in m^{-3}) and T_0 represents the temperature of the propellant, all of which are at the stagnation pressure. The expansion area (where the gas exits the thruster) is given by A_0 and χ represents the probability of a gas molecule exiting through this expansion area. The specific impulse depends on the stagnation temperature and the propellant mass m , where k and g_0 are Boltzmann's constant and the gravitational acceleration at sea level respectively.

To date, a number of resistojets have flown on-board CubeSat missions, see for example: the Aqua Thruster Demonstrator (AQT-D) mission [41]. Additionally, a type of resistojet called the Free Molecule Micro Resistojet (FMMR) is a MEMS fabricated resistojet that utilises water as its propellant and operates by expanding the heated propellant through a series of slots [42]. The system's low cost, low mass and low power consumption makes it highly favourable for use on a future CubeSat mission.

3.2.2 Electrostatic thrusters

These engines work by accelerating ions with the aid of electric fields as the ions move across a potential drop applied between two electrodes. The ions are used to generate thrust and are produced from the propellant atoms through electron bombardment. Numerous methods can be applied to heat the electrons which generate the ions in the plasma, namely: DC methods, radio frequency fields or, microwave fields. Electrostatic engines are the most developed type of electric thruster, originating from the 1950s [19]. Gridded ion thrusters, Hall effect thrusters, and more recently, Colloid-electrospray devices are the most commonly employed electrostatic thrusters. The principle of operation of each thruster is described below.

Gridded Ion Thruster (GIT)

This system achieves ion acceleration by utilising a potential drop between an extractor and acceleration grid. Ions are produced in an ionisation chamber either through collisions with injected electrons, through radio/microwave frequency or contact ionisation [33]. The accelerated ions are ejected from the system, producing thrust, and the resulting ion beam is neutralised by electrons emitted from an external cathode. Neutralisation is necessary to ensure that electrons collected at the anode are ejected to prevent the negative charging of the spacecraft.

The efficiency of ion engines depends on the type of propellant used (usually propellant with

a low first ionisation energy is desirable) as well as the electron current and the residence time of the propellant in the ionisation chamber [33]. When implemented on larger spacecraft, ion engines have demonstrated considerably high efficiencies (between 60% to 80% [19]) however, the miniaturisation of these systems has faced a myriad of challenges; namely:

- Decreasing the volume of the ionisation chamber reduces the residence time for electrons in the chamber and thus leads to a significant decrease in the propellant utilisation efficiency, at some point ionisation will cease completely. To maintain thruster efficiency the miniaturisation of the chamber must scale with the electron mean free path. This, however, necessitates operation in a high density regime which may lead to higher ion fluxes to the chamber wall, having an overall detrimental effect on the thruster [5].
- The electron supply, in the ionisation chamber, is usually sourced from an internal cathode; however, miniaturisation of a durable electron emitting cathode, as well as the manufacturing of electrical grids, poses a major challenge with regards to constructing them out of materials that are highly resistant to erosion caused by ion impact [33].
- At small scales the space charge between the accelerating grids imposes a limit on the maximum emission current density and subsequently the achievable thrust.

To mitigate some of these effects, miniaturised ion engines have incorporated radio frequency ionisation, as opposed to electron bombardment, as its main ionising mechanism. This eradicates the need for an internal electron emitter [43].

Radio Frequency Ion Thruster (RIT)

In RITs, the propellant is fed into a discharge chamber where it is ionised through radio frequency (RF) electromagnetic radiation produced from RF coils. The resulting plasma is extracted and accelerated through a combination of grids: the screen and accelerator grids. The screen grid extracts the positive ions from the plasma towards the accelerator grid which accelerates the ions outwards producing thrust. A neutraliser cathode is placed on the outside of the thruster which emits electrons to neutralise the resulting ion beam.

The thrust produced by the RF ion engine, equation (3.7), depends on the mass of the ions m_{ion} , the charge of the propellant ions q and the ion accelerating voltage V_i [5]. The specific impulse, equation (3.8), is also a function of these parameters and additionally depends on the mass utilisation efficiency η_m , which indicates the fraction of propellant mass that is converted into ions that are accelerated out from the thruster, and the total thrust

correction factor γ , which takes into account the divergence of the ion beam as well as the presence of multiply charged species.

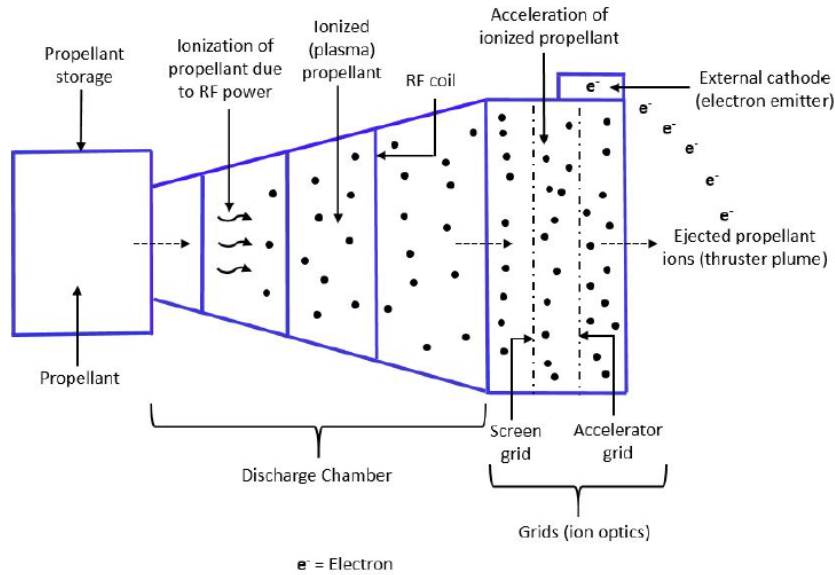


Fig. 3.2 Schematic showing the principle of operation of the Radio Frequency Ion Thruster. [5].

The thrust generated by a GIT is proportional to the ion mass and also depends on the ion beam current I_i , for this reason it is desirable to use a propellant source composed of elements with a high atomic mass (inert gases like xenon and krypton are most commonly used as propellants). The specific impulse of the system can be varied by changing the voltage applied between the accelerating grids. The mathematical equations for thrust and specific impulse of the GIT are:

$$T = \sqrt{\frac{2m_{ion}V_i}{q}} I_i, \quad (3.7)$$

$$I_{sp} = 1.417 \times 10^3 \gamma \eta_m \sqrt{\frac{V_i}{m_{ion}}}. \quad (3.8)$$

Considering all the limitations imposed on the miniaturisation of ion thrusters, none of these systems have been implemented on CubeSat missions; however, the upcoming Lunar IceCube mission will incorporate a miniature RF ion engine with solid iodine as its propellant source [44].

Hall-Effect Thrusters

Hall effect thrusters generate thrust from the ionisation and acceleration of propellant placed in a radially applied magnetic field and an axially applied electric field that are mutually perpendicular [45]. Neutral gas propellant is injected into the annular ionisation chamber near an anode located at the base of the discharge channel. The propellant is ionised by electrons produced from an external cathode located outside the discharge channel. These ions are then accelerated by the electrostatic fields applied between the anode and cathode. As the electrons move towards the anode they interact with the radial magnetic field and spiral around the thruster in the $(\vec{E} \times \vec{B})$ direction.

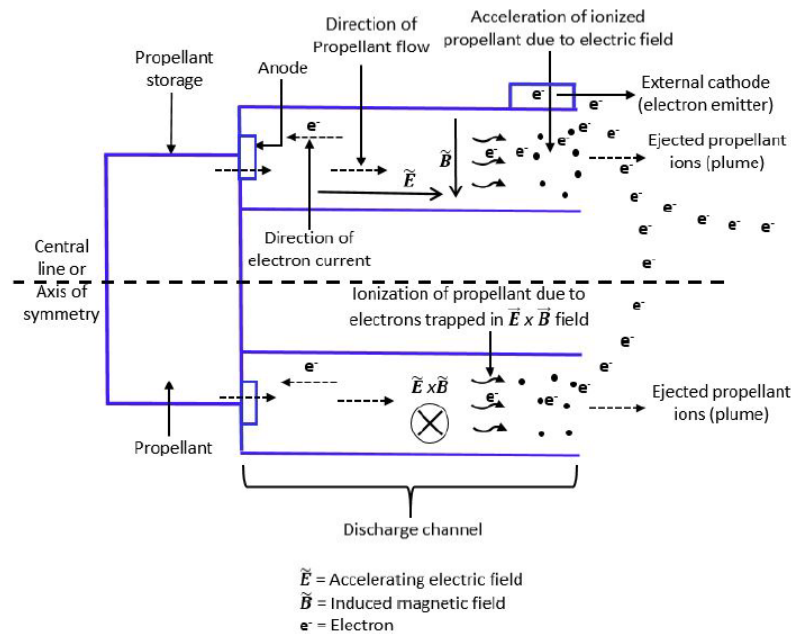


Fig. 3.3 Schematic showing the principle of operation of the Hall Effect Thruster [5].

The miniaturisation of the Hall effect thruster is advantageous over the GIT for the following reasons:

- The precessing of the electrons, due to their interaction with the radial magnetic field, leads to an increase in their residence time within the chamber, thereby resulting in an increase in the probability of collisions between the electrons and the neutral propellant. This subsequently results in an increase in the propellant utilisation efficiency.
- Hall thrusters are void of any acceleration grids, which are major life limiting components of most electric thrusters. Instead ions are primarily accelerated by the

electrostatic force produced by the potential drop between the anode and cathode, resulting from the Hall-effect.

- Generally, Hall thrusters produce a lower specific impulse but a much higher thrust density (in some cases up to an order of magnitude higher) than ion engines. These systems also exhibit greater adaptability over a wide range of power levels [19].

Notwithstanding its benefits, the Hall thruster also experiences erosion of its magnetic circuitry from interactions with the discharge plasma, resulting in a degradation in the thruster's performance. Furthermore, it is more challenging to control the ion beam in a Hall thruster than in an ion engine. In many cases this leads to wall erosion; however, wall erosion may be mitigated using magnetic shielding such that when the walls are magnetically shielded, the electric component parallel to the wall is largely negated, resulting in a decrease in ion impacts on the chamber walls [5]. Overall the efficiency of these systems are lower than GITs [19].

As in the case of ion engines, it is also beneficial to use high atomic mass propellant in Hall thrusters. Common propellant sources include: xenon (Xe), krypton (Kr), argon (Ar) and iodine (I). The mathematical equations representing the performance factors, like thrust and specific impulse, are the same for both systems and were shown in equation (3.7) and (3.8) respectively.

Various studies have found that, in miniaturised Hall thrusters, the propellant mass flow rate and the applied power are proportional to the length of the discharge channel [46]. In contrast, the magnetic field strength was found to be inversely proportional to the channel length. In this way, important parameters such as: the propellant mass flow rate, the strength of the magnetic field and the length of the discharge channel can be deduced through scaling laws provided that the power of the larger Hall thruster is known.

Electrospray thrusters

The electrospray thruster operates by extracting charged particles (ions) from a liquid (propellant) surface and accelerating them electrostatically to generate thrust. When the electric potential passes a threshold value, the conductive surface of the propellant is deformed into a Taylor cone and the ions are extracted from the apex of the cone [5]. Electrospray thrusters are capable of accelerating both positive and negative ions and can thus produce both a positive and negative ion beam, obviating the need for an external neutraliser cathode.

Low-volatility ionic liquids are used as the propellant source. Ionic liquids exhibit high conductivity in the pure state, have low operating voltages and a negligible vapour pressure [47]. These properties make the system favourable for miniaturisation. In electrospray thrusters, the exhaust velocity and thrust depend heavily on the charge-to-mass ratio. The average charge-to-mass ratio $\langle \frac{q}{m_{ion}} \rangle$ is given by:

$$\left\langle \frac{q}{m_{ion}} \right\rangle = \frac{1}{\rho Q}, \quad (3.9)$$

where ρ and is the density of the propellant and Q is the volume flow rate of the propellant. The main elements of the propulsion system are the propellant storage chamber, the emitter and extractor electrode shown in Fig.3.4.

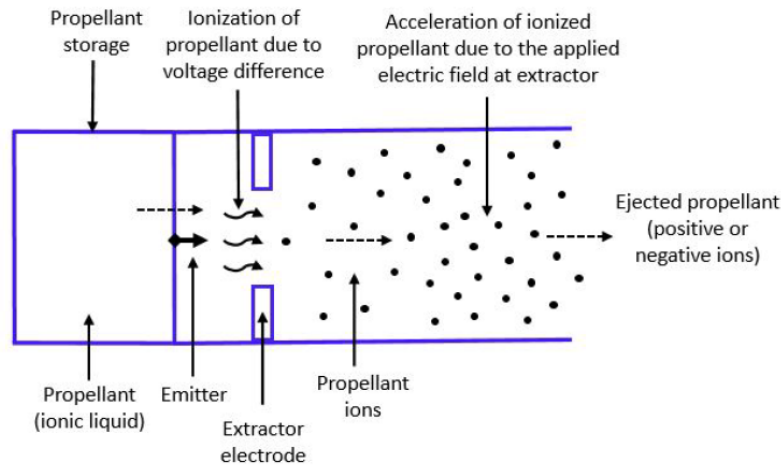


Fig. 3.4 Schematic showing the principle of operation of the Electrospray Thruster [5].

The thruster's performance can be controlled by varying the voltage passing through the emitter and extractor electrodes. The exhaust velocity v_{ei} depends on the ion accelerating voltage V_i , the ion beam current I_i and the average charge-to-mass ratio. The system's thrust can be calculated from the product of the propellant (ion) mass flow rate and the exhaust velocity as shown in equation (3.11):

$$v_{ei} = \sqrt{2V_i I_i \left\langle \frac{q}{m_{ion}} \right\rangle} = \sqrt{\frac{2V_i I_i}{\rho Q}}, \quad (3.10)$$

$$T = \dot{m}_{ion} v_{ei} = \sqrt{2V_i I_i \dot{m}_{ion}}. \quad (3.11)$$

The electrospray thruster can be further classified into two subthruster types, based on the method of extraction of the charged particles. These are the Colloid thruster and the Field Emission Electrostatic Propulsion (FEEP) thruster. Individual electrospray thrusters operate on the milli-Watt power level with a typical thrust in the micro-Newton range, suitable for microradian altitude control applications. An electrospray propulsion system has already been implemented on a CubeSat mission, the AeroCube 8 [47].

3.2.3 Electromagnetic thrusters

Electromagnetic thrusters use both electric and magnetic fields to produce, accelerate and expel ionised propellant for thrust. In these thrusters the ionised propellant is accelerated by the Lorentz force. These systems can generate high thrust densities in comparison to other electric propulsion systems. Two types of electromagnetic thrusters have been identified as systems with high potential to be used on the small satellite platform, namely: the Pulsed Plasma Thruster (PPT) and the Vacuum Arc Thruster (VAT).

Pulsed Plasma Thruster (PPT)

A Pulsed Plasma Thruster incorporates a solid insulating propellant (for example Teflon) and operates by producing a pulsed, high current discharge across the propellant's surface. The current discharge results in ablation (or vaporisation) of the propellant's surface, and the resulting vaporised propellant material is accelerated to produce thrust. The system operates in an unsteady regime where the current pulse lasts for a fraction of a second and is driven by the charging and discharging of a capacitor. A spring mechanism is used to feed the solid propellant into a region between two electrodes (the anode and cathode) while a spark plug is simultaneously fired to increase the electrical conductivity in the acceleration chamber [5]. The Power Processing Unit (PPU) provides electrical current to the electrodes through the capacitor and into the arc. The resulting current loop induces a magnetic field. The plasma (produced from the ablation of the propellant) is accelerated by the Lorentz force, generated by the induced magnetic field. The thruster's principle of operation is displayed in Fig.3.5.

A PPT can utilise many different propellants in both solid and liquid form. They can provide short bursts of thrust for precision maneuvering and can maintain a constant specific impulse and thruster efficiency over an extensive input power range. Generally, these systems exhibit a low thruster efficiency (10-20%) and are susceptible to electrode erosion [48], [49]. Another concern is the potential presence of macro-particles in the plume, resulting from

non-uniform ablation. These macro-particles can interact with the surrounding plasma and lead to undesirable effects.

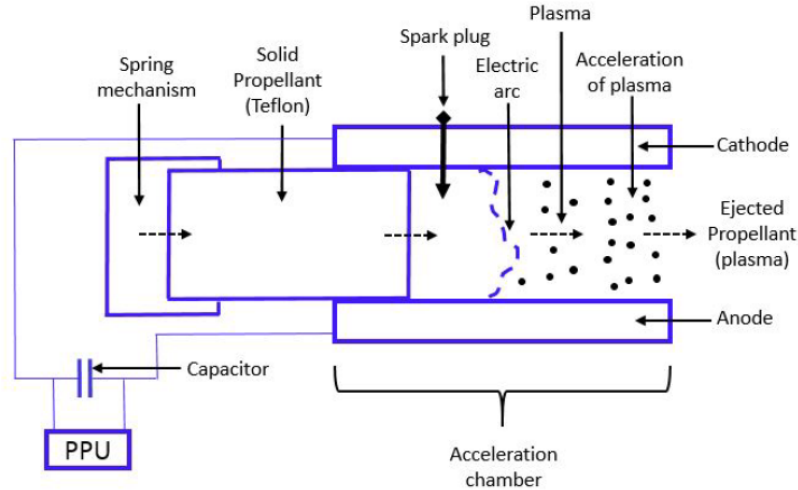


Fig. 3.5 Schematic showing the principle of operation of the Pulsed Plasma Thruster [5].

The thrust in the PPT is dictated by momentum conservation and depends on the charge of the ions q , the particle velocity \vec{u}_i and the sum of all collision forces for each individual particle k over all particles P_i . The first term in equation (3.12) represents the Lorentz force which is generated by the movement of charged particles in a self-induced magnetic field. The effective velocity, equation (3.13), is dependent on the thrust T , the propellant mass flow rate \dot{m} and the thruster efficiency η . It can also be deduced from the ratio of the anode and the cathode radius, R_a and R_c respectively.

$$T = m_{ion} \frac{d\vec{v}_i}{dt} = q(\vec{E} + \vec{u}_i \times \vec{B}) + \Sigma(P_i)_k, \quad (3.12)$$

$$v_e = \frac{T}{\dot{m}\eta} = \frac{1}{\eta} \frac{\mu_0}{4\pi} \ln \left(\frac{R_a}{R_c} \right) \quad (3.13)$$

In addition to the problems associated with electrode erosion, low propellant conversion efficiency in PPTs has hindered the development of efficient PPTs. A modified version of the PPT called the Planar Pulsed Inductive Thruster (PIT) was developed to overcome these issues. The PIT is able to accommodate a variety of propellants (like ammonia, water and carbon dioxide) and does not utilise any electrodes. These systems have shown potential to process high power levels and thereby produce high levels of thrust with just a single thruster [50].

Vacuum Arc Thrusters (VAT)

Another variation of the PPT is the vacuum arc thruster, which produces completely ionised high velocity plasma jets as a result of the ablation of cathode material in a vacuum (through vacuum arc discharges). These thrusters have been studied since the 1960s and exhibit various advantages for propulsion applications. Some of the advantages of VATs are:

- The thruster has a low mass, since it does not use a gas feed system, and is relatively simple to design.
- VATs offer high efficiencies from their highly ionised plasma generation.
- The VAT has an efficient discrete pulse operation allowing the thruster to perform finely tuned spacecraft maneuvers [51], [52].

There are two major disadvantages associated with VATs:

- The thrust level produced by the system can only be adjusted by varying the pulse duty cycle.
- The directional efficiency of the thrust depends strongly on the geometry of the electrodes [51].

Despite its limitations, a VAT has been flown on a CubeSat mission (BRICSat-P [53]).

3.2.4 Propellant-less propulsion

A discussion on novel propulsion concepts is not complete without mentioning propellant-less means of producing thrust. Among various proposed concepts, solar sails (including electric and magnetic sails) are of much interest as they demonstrate a high potential of being used on low mass satellites.

Solar Sails

Solar sails rely primarily on solar radiation pressure for thrust. They utilise lightweight expandable structures made from reflective materials, which provide a means for momentum exchange with incident solar radiation. Theoretically, the solar sail (and any type of propellant-less propulsion for that matter) can produce an infinite specific impulse; however, these systems take a long time to gain an appreciable momentum change. The low thrust characteristic makes the system useful as an end-of-life de-orbiting device, as demonstrated

by the NanoSail-D mission [54]. Solar sails have also seen implementation on IKAROS [55] and CubeSat LightSail-1 [56]. Other types of sail propulsion include electric and magnetic sail propulsion.

Electric sail propulsion

This system consists of a conductive mesh that is maintained at a positive potential relative to the solar wind plasma. The positive potential then repels the positive particles in the solar wind, leading to a momentum exchange on the spacecraft. Since the interactions are weak, these systems would require large scale structures for a noticeable thrust to be achieved. This system still remains in the conceptual phase.

Magnetic sail propulsion

The magnetic sail uses a loop structure (a superconducting wire) and obtains momentum exchange through the interaction of an induced magnetic field on the solar wind particles. The magnetic field deflects the solar particles from their original trajectory and the resulting change in momentum is transferred to the sail producing thrust. In this way the magnetic sail differs from the solar sail (which uses radiation pressure from solar photons for thrust). Since photons carry significantly more momentum than solar wind particles, the magnetic sail needs to deflect a larger area of solar wind particles to generate the same amount of thrust as the solar sail. In both cases the thrust decreases in proportion to the the square distance of the sail from the sun; however, the magnetic sail can also produce thrust by interacting with a strong planetary magnetosphere.

3.3 Basic Plasma Physics

To conduct a detailed study of the thruster concept proposed in this work requires an understanding of basic plasma physics. In this section, a description of the plasma state is given, including: examples of natural and man-made plasmas, the mathematical definition of a plasma, the energy and velocity distributions of the various plasma particles along with the various types of plasma particle collisions, and lastly, the concept of a plasma sheath.

3.3.1 The plasma state of matter

A plasma is composed of neutral gas atoms or molecules, ions, and electrons. Plasmas can be categorized into two groups: thermal plasmas and electrical plasmas.

Thermal Plasma

A thermal plasma is formed when a gas is heated above a certain temperature (usually $\geq 5000\text{ K}$) causing the kinetic energy of the gaseous atoms to increase thus resulting in a high number of atomic collisions within the gas. These collisions cause electrons to be stripped away from the atoms, as the gas becomes ionised and transitions into a plasma state. All species within a thermal plasma are in thermal equilibrium, hence:

$$T_g \simeq T_i \simeq T_e,$$

where the subscripts g , i and e denote the gas, ion and electron quantities respectively.

Electrical Plasma

An electrical plasma can be produced when a gas is subjected to strong electromagnetic fields. This method eradicates the need for high gas temperatures which would otherwise be required in the formation of thermal plasmas. The resulting plasma is composed of electrical charges: ions and electrons. Consequently, the plasma is influenced by electric and magnetic fields (including self-induced electric and magnetic fields) as is also the case in thermal plasmas. The charged particles can thus be preferentially heated by these applied fields. In particular, electrons, due to their lower mass ($m_e \ll m_i < m_g$), can be accelerated to sufficiently high energies for the ionisation of neutral gas atoms. Consequently, the species within an electrically induced plasma (otherwise known as a 'discharge') are not in thermal equilibrium, since

$$T_e \gg T_g, T_e > T_i > T_g.$$

Electrical plasmas exhibit a lower degree of ionisation than their thermal counterparts. This research deals exclusively with a special type of electrically induced plasma known as a low pressure, direct current, glow discharge. In this case, the particle temperatures are known to occur in a more restricted range:

$$T_e \gg T_i \simeq T_g,$$

where T_i and T_g are approximately at room temperature.

Plasmas in nature and the laboratory

Plasmas are ubiquitous in nature, with more than 99% of the observable matter in the universe existing in the plasma state [57]. Examples of naturally occurring plasmas include stars, lightning and the aurora borealis, while neon lamps are the most commonly used example of a man-made plasma. Much of the drive towards understanding the underlying physics of plasmas comes from the desire to produce fusion energy, through nuclear fusion reactors, as a clean and sustainable alternative energy source on Earth. This has led to the development of Tokamaks, which are devices that magnetically confine hot plasma in an attempt to produce controlled thermonuclear fusion power [58].

A plasma state can span a wide range of temperatures and densities. Fig.3.6 provides a depiction of the characteristic temperature and density of various natural and man-made plasmas.

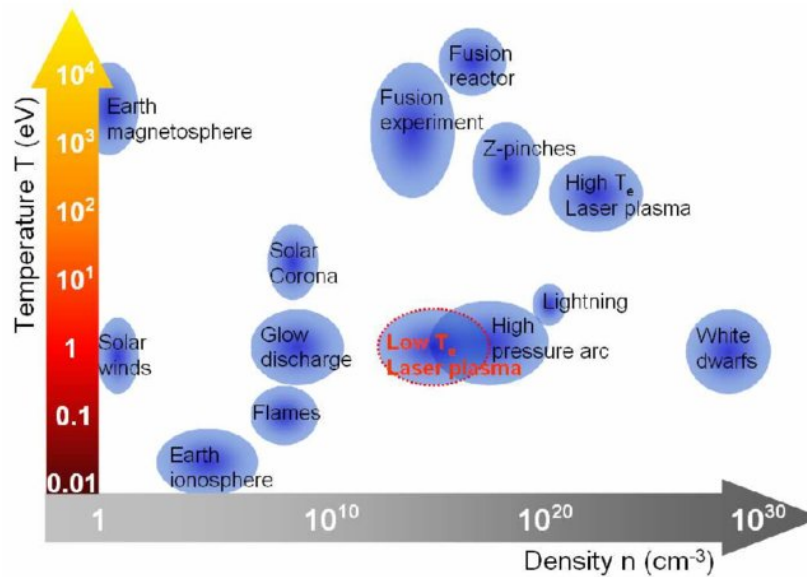


Fig. 3.6 Characteristic temperature and density of various plasma sources [6].

A plasma is a highly complex medium which can be characterised by non-linear phenomena that occur over a wide range of spatial and temporal scales. It is therefore extremely challenging to model the behaviour of a plasma, nevertheless, the complexity can be reduced by understanding some of the basic phenomena occurring within them.

3.3.2 Definition of a plasma

The formal definition of a plasma can be stated as follows:

*"A plasma is an ionised gas that is **globally neutral** and displays **collective effects**."*

To be globally neutral (or rather quasi-neutral) the size of the plasma has to be much larger than the Debye length (the scale length at which quasi-neutrality can be violated). The term collective effects implies two things: firstly, that one-to-one interactions between particles are weak, the plasma interacts through collective electric and magnetic fields and not those resulting from one-to-one particle interactions. Secondly, it implies that the frequency of the collective motion of the plasma (the plasma frequency) is larger than the collision frequency.

The Debye length, plasma frequency, and collision frequency are important concepts and will be discussed in more detail in the sections to follow.¹

Debye length

Consider a plasma that is initially in a quasi-neutral state i.e the electron and ion densities are approximately equal ($n_e \approx n_i = n$). For simplicity, assume that the ions are singly ionised i.e. $Z = 1$ (where Z is the number of positive charges per ion). A positive test charge q_t is inserted within the neutral plasma. Consequently, an electrostatic potential forms around the test charge as the negatively charged particles are attracted towards it. The positive ions are repelled and an electron cloud is formed (see Fig.3.7). In solving for this electrostatic potential a length will appear, this is precisely the Debye length of the plasma.

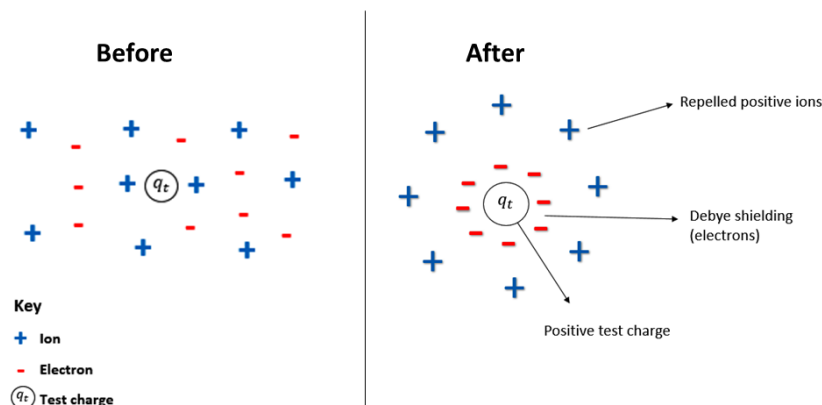


Fig. 3.7 Illustration of the Debye shielding effect. An electron cloud forms around a positive test charge q_t which effectively screens the positively charged ions.

¹Refer to Appendix B for a rigorous derivation of the Debye length and plasma frequency.

The Debye length describes the distance over which charges are electrostatically shielded, it is physically interpreted as the screening distance due to a cloud of negative charges (electrons) surrounding a positively charged ion. In this way, it describes the characteristic length of the plasma where the electric field from a point charge outside the Debye length will be shielded from the positive ion.

The Debye length λ_{De} is mathematically expressed as follows:

$$\lambda_{De} = \sqrt{\frac{\epsilon_0 T_e}{e^2 n}} = 7 \times 10^3 \sqrt{\frac{T_e}{n}}, \quad (3.14)$$

where T_e is the electron temperature (measured in eV) and n is particle number density (in m^{-3}).

Solving the Poisson equation (representing the potential around the test charge) yields the following solution:

$$\Phi(r) = \frac{1}{4\pi\epsilon_0} \frac{q_t}{r} \exp\left(-\frac{r}{\lambda_{De}}\right). \quad (3.15)$$

The result is similar to the electrostatic potential for a charge in a vacuum, with an added exponential factor due to the medium being a plasma. Fig.3.8 shows a comparison between a standard Coulomb potential and the electrostatic potential expressed in equation (3.15).

The one-to-one interactions between particles will be weak only if there is a high number density of electrons and ions within the plasma volume (λ_{De}^3) $\implies n\lambda_{De}^3 = N_D \gg 1$, where N_D represents the number of charged particles within a Debye cube (effectively a cube with side length equal to the debye length). The quasi-neutrality of a plasma is only true at distances beyond the Debye length (deviations from quasi-neutrality will occur at distances shorter than the Debye length). To be globally neutral (or rather quasi-neutral) the size of the plasma has to be much larger than the Debye length.

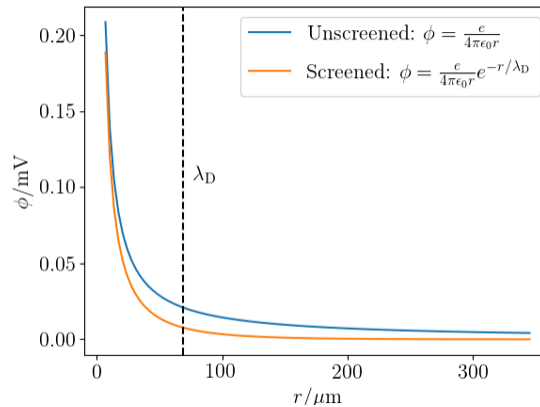


Fig. 3.8 Comparison of a standard Coulomb potential with a Debye screened potential.

Plasma frequency

Consider a slab of plasma with an initial electron number density n_0 . Assume that the ions in the plasma constitute a fixed background, with the same density as the electrons. The plasma can be separated into three regions: region 1 where the charge is positive ($\rho > 0$), region 2 where the charge is approximately zero ($\rho \approx 0$) and region 3 where the charge is negative ($\rho < 0$). If the electrons are displaced from the ions by a distance Δx (see Fig. 3.9) then the displaced electrons will tend to be attracted back towards the ions, causing an oscillatory motion of the electrons with respect to the fixed ion background. The frequency of this resulting oscillation is precisely the plasma frequency.

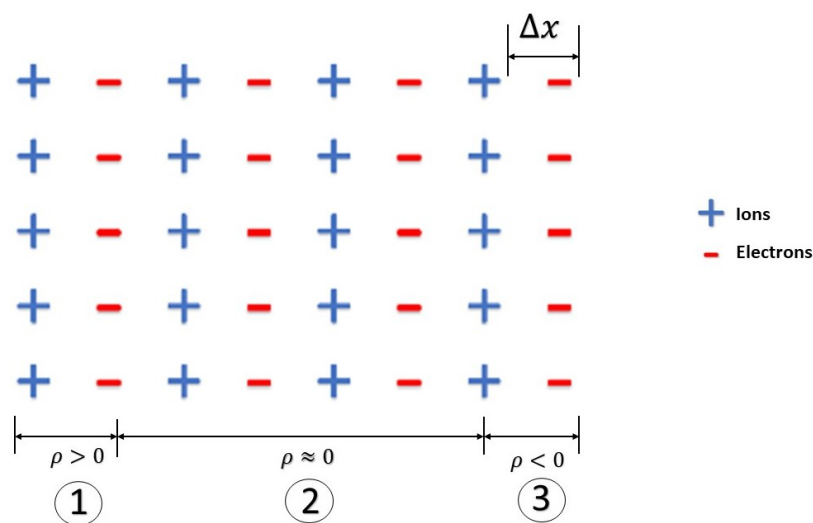


Fig. 3.9 Plasma slab with electrons displaced from a fixed ion background.

The electron plasma frequency ω_{pe} is a fundamental parameter used in characterising a plasma. It gives the rate at which electrons oscillate from equilibrium, relative to a static ion background, and is mathematically expressed as follows:

$$\omega_{pe} = \sqrt{\frac{n_0 e^2}{\epsilon_0 m_e}}, \quad (3.16)$$

where m_e represents the mass of an electron and e is the electron charge. Electromagnetic waves with frequencies lower than the plasma frequency will cease to propagate as the plasma will effectively negate their fields.

The electron plasma frequency can be expressed more conveniently as:

$$f_p = \frac{\omega_{pe}}{2\pi} \sim 9\sqrt{n_e}. \quad (3.17)$$

The inverse of equation (3.17) provides an approximate time scale for the plasma to react to changes in its boundaries and/or in the applied potentials [19]. For example, a plasma with an electron density of 10^{16} m^{-3} will have a corresponding electron plasma frequency of 0.9 GHz, and will take roughly 1 nanosecond to respond to plasma perturbations.

Similarly, for plasmas where ion motions are the dominant driver of plasma perturbations, the ion plasma frequency can be deduced using (3.16) by replacing the electron mass with the ion mass:

$$\omega_{pi} = \sqrt{\frac{n_0 e^2}{\epsilon_0 m_i}}. \quad (3.18)$$

The approximate time scale, to first order, for ion motions within the plasma can be deduced from equation (3.18). The ions, however, have inertia and respond at the ion acoustic velocity v_a . In the special case of electrostatic ion engines, where $T_e \gg T_i$, this ion acoustic velocity is given as:

$$v_a = \sqrt{\frac{kT_e}{m_i}}. \quad (3.19)$$

3.3.3 Plasma particle energies and velocities

A large number of collisional processes may occur within the plasma contained in electrostatic thrusters. These include: collisions between particles of the same species (e.g. ion-ion collisions) and collisions between particles of different species (e.g. electron-neutral collisions). The knowledge of collisional processes is important for characterising the mobility, diffusion and resistivity of the plasma. These collisional processes can be used to develop a velocity distribution for each species. In the absence of external forces, every particle within the plasma (on average) will move with a velocity that depends solely on the mass and macroscopic temperature of that particular species [19].

The majority of charged particles in electric thrusters conform to a Maxwellian velocity distribution. In the generalised three-dimensional case, the Maxwellian velocity distribution function is given by:

$$f(u, v, w) = \left(\frac{m}{2\pi kT} \right)^{3/2} \exp \left[-\frac{m}{2kT} (u^2 + v^2 + w^2) \right], \quad (3.20)$$

where m represents the particle's mass, and T is the corresponding particle temperature. The terms u, v and w represent the respective velocity components in a three coordinate axes. The average kinetic energy of a particle within the Maxwellian distribution can then be deduced as follows:

$$E_{ave} = \frac{\int \int \int_{-\infty}^{\infty} \frac{1}{2} m v^2 f(u, v, w)}{\int \int \int_{-\infty}^{\infty} f(u, v, w)} = \frac{3}{2} kT. \quad (3.21)$$

Similarly, the particle number density, n , can be obtained from equation (3.20):

$$n = \int \int \int_{-\infty}^{\infty} n f(u, v, w) du dv dw. \quad (3.22)$$

Finally, the incident particle flux, in one direction, is [19]:

$$\Gamma = \frac{1}{4} n \bar{v} = \frac{1}{4} n \sqrt{\frac{8kT}{m\pi}}. \quad (3.23)$$

Note that the last term in equation (3.23) represents the average particle speed in a Maxwellian distribution (see [19], p.45).

Equations (3.20-3.23) are accurate descriptions of the energies and velocities of plasma electrons. However, the presence of electromagnetic fields (within the plasma) forces the electrons to move along field lines. Thus, the electron motion is no longer purely random. Subsequently, the flux term needs to be modified to account for this non random motion (see [19], p.46-54).

In electrostatic ion engines, the ions are relatively colder than the electrons, where the electron temperature is roughly ten times greater than the ion temperature (i.e. $T_e/T_i \approx 10$). This is mainly due to inefficient heating and the fact that ions are not well-confined within the ionisation chamber (they are accelerated out of the thruster to produce the thrust beam). Due to charge conservation, the ion velocities and ion particle fluxes at the plasma boundaries are dependent on the electric fields generated within the plasma and differ from the expressions given in this section. These variations will be described in more detail in section 3.3.4.

3.3.4 Collisional processes and collision frequencies

Generally, collisional processes can be described as follows: an incoming particle, for example, an electron, moving at a certain velocity v travels towards a certain number density of target particles n_{target} . From the electron's perspective, each target particle will have a collision area denoted by σ (also called the cross section). The frequency of collisions between the electron and the target particles is then given by the following expression:

$$V_{coll} = n_{target} \cdot \sigma \cdot v. \quad (3.24)$$

Collisions between electrons and neutrals

Electrons can collide elastically or inelastically with neutral particles. The electron mean free path λ_e gives the average distance that an electron would travel, through a fixed neutral particle background n_g , before undergoing a collision:

$$\lambda_e = \frac{1}{n_g \sigma}. \quad (3.25)$$

Inelastic collisions between electrons and neutrals may result in ionisation or excitation of neutral particles. The subsequent ion production rate, $\frac{dn_i}{dt}$, and excited neutral production rate, $\frac{dn^*}{dt}$, per unit volume can be expressed as:

$$\frac{dn_i}{dt} = n_g n_e \langle \sigma_i v_e \rangle \quad (3.26)$$

$$\frac{dn^*}{dt} = \sum_j n_g n_e \langle \sigma_* v_e \rangle_j. \quad (3.27)$$

Here, σ_i represents the ionisation cross section, n_g is the number density of neutrals and v_e is the electron velocity. Collectively, $\langle \sigma_i v_e \rangle$ represents the reaction rate coefficient, the ionisation cross section averaged over the electron velocity distribution function. Similarly, σ_* represents the excitation cross section. In equation (3.27), the reaction rate coefficient is averaged over the electron distribution function and summed over all excited states j . Note that for simplicity, equations (3.26) and (3.27) do not consider the terms associated with particle losses to the boundaries of the plasma

The collision frequency, describing collisions between electrons and neutrals, is given by:

$$\nu_e^{neutral} = n_g \cdot v_e \cdot \sigma \approx n_g \cdot \sqrt{\frac{8kT_e}{m\pi}} \cdot \pi a_0^2. \quad (3.28)$$

The last expression follows from the fact that the cross section can be approximated by the size of the atom, where a_0 is the Bohr radius i.e. $\pi a_0^2 \sim 10^{-20} \text{ m}^2$.

Coulomb collisions

In addition to collisions with neutral particles, electrons can collide with other charged particles (for example electron-electron and electron-ion collisions). The original trajectory of the electron can be deviated by the Coulomb force. This deviation becomes important when the Coulomb interaction energy is comparable to the kinetic energy, i.e. when

$$\frac{\text{Coulomb energy}}{\text{Kinetic energy}} \sim \frac{e^2}{4\pi\epsilon_0 b} \sim 1 \implies b \sim \frac{e^2}{4\pi\epsilon_0 m_e v_e^2}. \quad (3.29)$$

In the above expression, b represents the impact parameter, the distance of closest approach if the particle were to continue moving along its unperturbed trajectory.

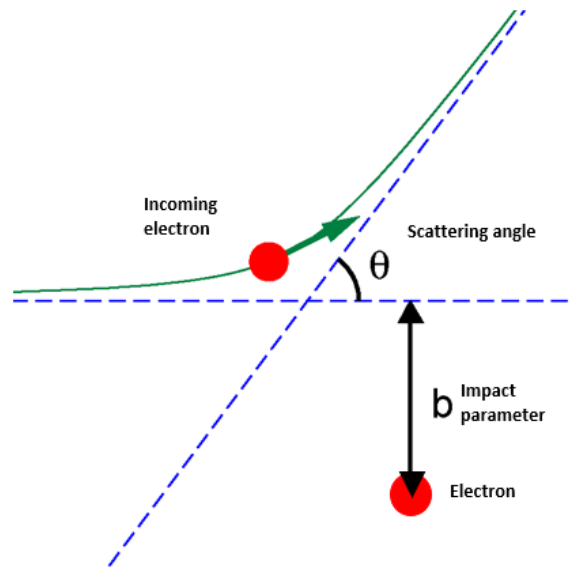


Fig. 3.10 Schematic of the Coulomb interaction experienced by an electron.

The collision frequency due to Coulomb collisions can now be estimated as:

$$\nu_e^{Coulomb} = n_e v_e \pi b^2 = \frac{n_0 e^4}{16\pi \epsilon_0^2 m_e^2 v_e^3}. \quad (3.30)$$

Since the ion mass is far greater than the electron mass (i.e. $m_i \gg m_e$) the energy transferred in electron-electron collisions is much greater than that of electron-ion collisions, and this leads to a shorter electron-electron thermalisation time relative to the electron-ion thermalisation time. This provides a reason as to why electrons thermalise rapidly into a Maxwellian distribution but do not thermalise rapidly with ions [19].

3.3.5 Plasma sheaths

The thruster to be studied in this work consists of a plasma, generated from the electrical breakdown of a gas, confined within a cylindrical discharge tube with the ends of the tube open to a vacuum. The boundaries of the plasma within the tube represent the physical interface at which energy and particles enter and leave the plasma. In this particular case, the boundaries are the walls of the thruster chamber and the surface of the electrodes confining the plasma. The plasma establishes potential and density variations at its boundaries, ensuring that particle balance is satisfied. The region where these variations occur is termed the plasma sheath (see Fig.3.11). An analysis of the sheath region is crucial for assessing the extraction capabilities and performance of the electric thruster.

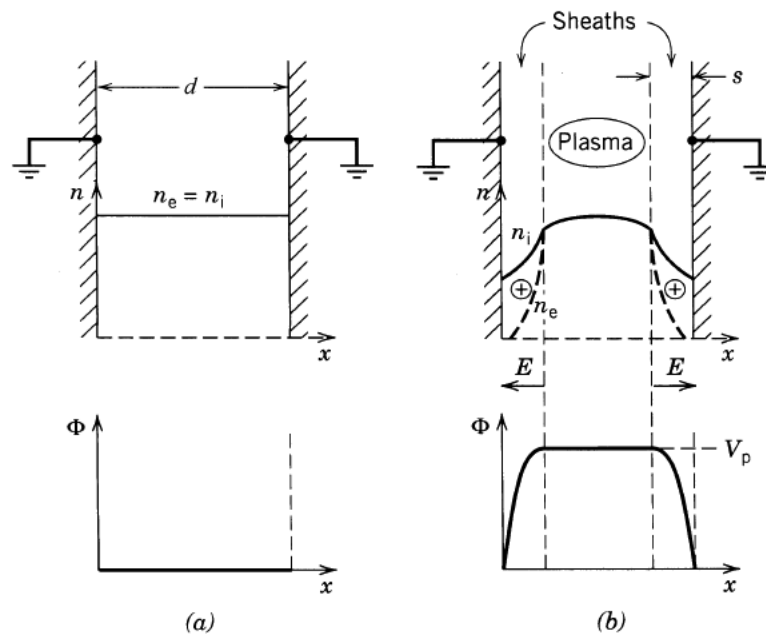


Fig. 3.11 Plasma particle densities before (a) and after (b) sheath formation at the plasma boundary. Image taken from [7].

As soon as the gas is ionised, electrons and ions begin to collide with the thruster walls, which have a plasma potential ϕ_p . The electrons move at higher thermal velocities than ions and collide more frequently with the walls, losing energy at a faster rate than the ions. The higher thermal velocity also means that initially there will be a net negative charge at the thruster walls; consequently, a net positive charge forms in the plasma bulk. This effect makes the potential at the walls negative with respect to the plasma. The resulting potential difference ensures that further incoming electrons are reflected from the walls and the ions fall onto the walls without being reflected. This electron repulsion produces a net positive space-charge region referred to as the Debye sheath. The sheath ensures that neutral plasma is shielded from the negatively charged walls, thereby maintaining the quasi-neutrality condition. If the shielding extends to distances greater than the Debye length, then the plasma will maintain a constant potential (ϕ_p). On the other hand, the equilibrium potential drop ($-\phi_w$) is defined as the potential required to ensure equal electron and ion losses to the wall.

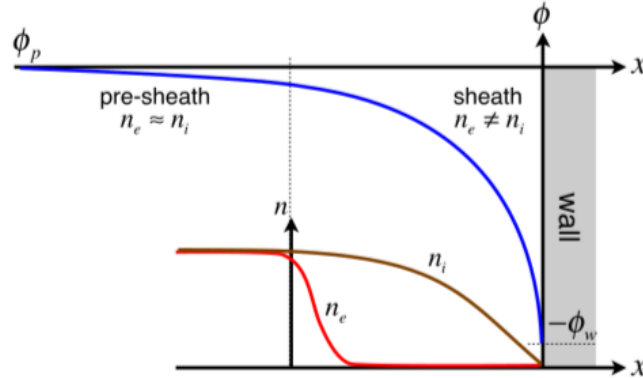


Fig. 3.12 The plasma and potential distribution near a material wall [8].

The pre-sheath (see Fig.3.12) contains the quasi-neutral plasma. A small potential drop occurs within this region which then facilitates the acceleration of ions, ensuring that the ions enter the non-neutral sheath region at high velocities. A similar phenomenon occurs at the negative electrode, the cathode attracts positive ions and repels electrons. This results in the formation of a positive ion sheath (consisting of positive ions and neutral atoms) surrounding the negative electrode. The positive ion sheath screens the electrodes from the discharge.

Ion and electron current densities

The ion current density, J_i , entering at the sheath edge is given as:

$$J_i \approx nev_a = ne\sqrt{\frac{kT_e}{m_i}}, \quad (3.31)$$

where n represents the initial plasma particle density at the sheath edge ($n = n_e \approx n_i$, see Fig.3.12) and v_a is the ion acoustic velocity (also known as the Bohm velocity). Equation (3.31) is more commonly expressed as the Bohm current, I_i :

$$I_i = n_i e \sqrt{\frac{kT_e}{m_i}} A. \quad (3.32)$$

Here, A represents the total ion collection area at the sheath boundary.

Similarly, the electron current entering the sheath region can be deduced using the random electron flux, see equation (3.23), multiplied by the Boltzmann factor:

$$I_e = \frac{1}{4} en_e \sqrt{\frac{8kT_e}{m_e \pi}} A \exp\left(-\frac{e\phi}{kT_e}\right) \quad (3.33)$$

To ensure charge conservation and zero net current at the walls, the plasma will tend to self-bias to a floating potential (ϕ). This floating potential can be determined by equating the ion and electron currents and solving the resulting expression:

$$\phi = \frac{kT_e}{e} \ln\left(\sqrt{\frac{2m_i}{m_e \pi}}\right) \quad (3.34)$$

The thickness (or length) of the sheath region depends on the potential difference between the plasma and the wall, in addition to other plasma parameters. If the electron temperature exceeds the sheath potential, i.e. if $kT_e > e\phi$, the sheath thickness can be estimated to be on the order of the Debye length, see equation (3.14).

When the sheath potential greatly exceeds the electron temperature, i.e. when $e\phi \gg kT_e$, the ion current density through the sheath region can be found from the Child-Langmuir equation [9]:

$$J_i = \frac{4\epsilon_0}{9} \sqrt{\frac{2e}{m_i}} \frac{\phi^{\frac{3}{2}}}{d^2}. \quad (3.35)$$

The above equation states that the ion current in the sheath region is proportional to three-halves the power of the sheath potential divided by the sheath thickness (d) squared. Furthermore, it implies that space charge effects limit the current density passing through a planar sheath region.

Double layered sheaths

The discussion thus far has only considered the unidirectional flow of particles from the plasma to the walls (or electrodes). In many instances, particularly near an electron-emitting cathode, two plasmas of differing potentials may be in contact with each other allowing for electrons and ions to counter-stream across the boundary. This results in the formation of a double sheath layer. If the two plasmas in contact with each other, have the same effective

area, then the space-charge-limited flow of electrons and ions between them is given by:

$$J_e = \kappa \sqrt{\frac{m_i}{m_e}} J_i. \quad (3.36)$$

Here, κ is a constant which depends on the ratio of particle temperatures $\left(\frac{T_e}{T_i}\right)$. In typical thruster plasmas $\kappa \sim 0.5$.

If one of the boundaries of the double layer represents the sheath edge at an electron emitting cathode, then the maximum space-charge-limited current density that the bulk plasma can accept from the electron emitting cathode can be determined from the following expression:

$$J_e = \frac{\kappa}{2} n_i e \sqrt{\frac{kT_e}{m_e}}. \quad (3.37)$$

The equations given in this section are used extensively in describing plasma behaviour in electric thrusters. More details including derivations for these equations can be found elsewhere (see [59] and [60])

This concludes the basic plasma physics section and literature review. The next chapter delves into the physics of DC glow discharges and the main operating principles of low-pressure gas discharge devices, similar to the proposed thruster concept.

Chapter 4

Glow Discharge Theory and Simulation

The thruster concept to be studied in this work is heavily based on the popular DC glow discharge tube. Therefore, a fundamental understanding of the operating principle of glow discharges is required to gain a deeper insight into how the thruster is expected to behave under various conditions.

The study of glow discharges dates back to the latter part of the nineteenth century, occurring in parallel with advancements in vacuum tube technology [61]. A simple DC discharge can be established by passing electric current through a gas between two electrodes (an anode and a cathode) located at opposite ends of each other. The electrodes and the gas are usually enclosed in an evacuated insulating envelope. The type of discharge produced depends on the nature and pressure of the working gas, the voltage applied between the electrodes as well as the geometry of the discharge [61]. This chapter will look more into the phenomenon of glow discharges, which are used for their light emitting characteristics in fluorescent lamps and as pump sources for gas lasers. Glow discharges also find applications in the material processing and microelectronic industries.

4.1 DC Glow Discharges

Glow discharges appear in the current range of μA to hundreds of mA , with current densities ranging from $10^{-7} - 10^{-2} A \cdot cm^{-1}$ and at pressures ranging from 0.5- 300 Pa [9]. Figure.4.1 shows a simple circuit that can be used to generate a DC glow discharge.

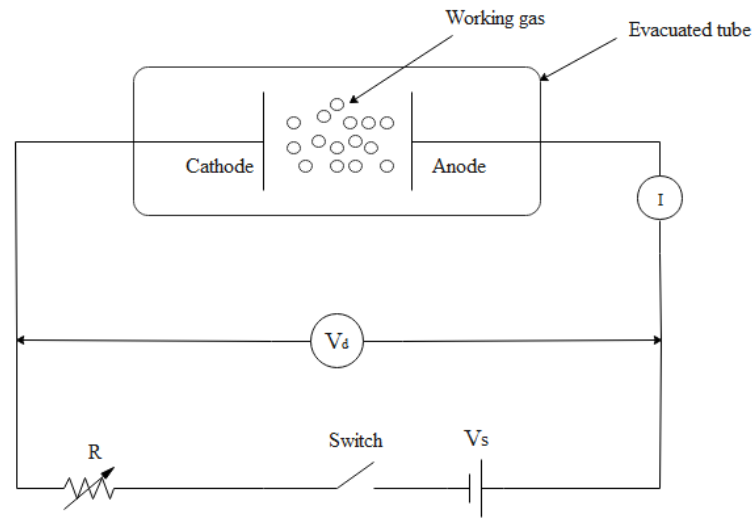


Fig. 4.1 Circuit setup used to generate a glow discharge.

To initiate a gas discharge, a flow of electric current (driven by either ions or electrons) through the gaseous medium is required. This is accomplished through the ionisation of the gas into a plasma state. When the switch is closed, a DC voltage is applied across the two electrodes. The discharge voltage V_d depends on the discharge current I and other properties of the discharge tube; including the gas pressure, the type of gas used, the electrode material and the electrode temperature. It is mathematically expressed as:

$$V_d = V_s - IR, \quad (4.1)$$

where V_s represents the supply voltage. A current limiting variable resistance R is connected in series and is used to control the flow of current through the discharge. The discharge current and voltage can be varied by changing the load resistance and/or the source voltage. The electrical characteristics of a glow discharge inside a short tube can be described using the voltage-current curve shown in Fig.4.2.

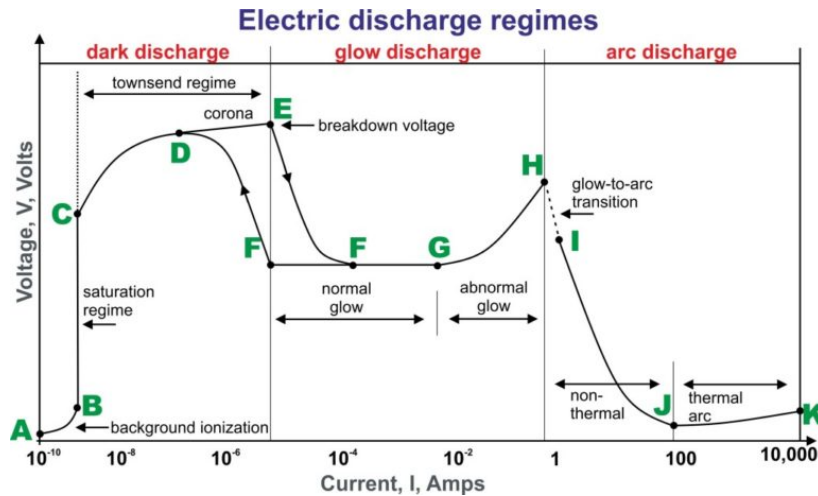


Fig. 4.2 Voltage-current relationship of a glow discharge.

Like most plasma phenomena, the curve in Fig.4.2 displays a highly non-linear behaviour. The electric discharge is characterised by three main regions: the dark discharge, glow discharge and arc discharge. The concept of electrical breakdown in gases needs to be introduced to better understand the processes occurring in each regime.

4.1.1 Electrical breakdown in low pressure gases

Electrical breakdown refers to a phenomenon in which an electrically insulating gas transitions into a conducting state by virtue of an applied electric field. It is precisely this phenomenon that leads to the formation of a self sustaining discharge within a glow discharge tube.

Recall the circuit diagram shown in Fig.4.1. Initially, electrons are emitted from the cathode through either direct emission (thermionic or field emission processes) or through indirect processes (e.g. by photoemission, photon bombardment on the cathode surface). For cold cathode tubes, with applied voltages of the order of a few thousand volts, the direct emission processes are negligible. In this case electrons are most likely ejected by the process of photoemission resulting from background radiation. In addition to this, the background radiation can also directly ionise the gas in the tube, through the process of photoionisation, producing even more electrons [61].

When a potential difference is applied between the electrodes, an electric field is generated along the axis of the discharge tube. The electrons (and ions), generated from photoemission (and photoionisation), then move along the field lines towards the anode (and cathode). This

results in a weak electric current (corresponding to region **A- B** in Fig.4.2).

The fraction of ions and electrons migrating to the electrodes increases with an increase in voltage. Eventually, the voltage increases to a point where all of the electrons and ions are collected by the electrodes and the current saturates. The saturation region (corresponding to region **B- C**) is obtained where the current remains constant as the voltage is increased. This saturation current I_0 is mathematically expressed as:

$$I_0 = \dot{N}_0 e, \quad (4.2)$$

where \dot{N}_0 represents the rate of production of electrons from photoemission/photoionisation and e is the electron charge. At this point the discharge produced is too weak to be visible and depends primarily on an external source, it is therefore not a self-sustaining discharge.

Increasing the voltage beyond point **C** results in a higher electric field strength and subsequently an increase in the energy of the electrons moving towards the anode. The electrons now have sufficient kinetic energy to ionise neutral gas atoms. Each electron can now give rise to two electrons and an ion originating from a neutral atom. The additional electrons can also ionise neutral atoms and subsequently produce an avalanche of electron-ion pairs. Consequently, the discharge current increases exponentially above the saturation current (corresponding to region **C- E**). This region of exponentially increasing current is called the Townsend discharge regime and the corresponding current produced from the avalanche ionisation is given by:

$$I = I_0 e^{\alpha L}, \quad (4.3)$$

where α is defined as the number of ionising collisions per electron, per unit length along the electric field E , otherwise known as Townsend's first ionisation coefficient, and L represents the distance between the electrodes. Despite the exponential increase in current, the discharge is still entirely dependent on an external source and is thus not a self-sustaining discharge.

As the electrodes are stressed even further, the higher electric field may produce corona discharges (region **D- E**) near sharp edges within the tube. At low currents this coronal discharge is not visible to the human eye and fits aptly in the dark discharge regime.

Each electron ionising event gives rise to a positive ion which then moves, through the

electric field, towards the cathode. Most of the ions are neutralised when they impact the cathode but some of the ions go on to produce secondary electron emission from the cathode by virtue of the Auger effect. Townsend's second ionisation coefficient γ characterises the number of electrons emitted per incident ion ($\gamma \sim 10^{-2}$, depending on the type of gas and the electrode material). These secondary electrons can create further avalanches on their path towards the anode and subsequently lead to an increase in current between the electrodes. Taking the secondary emission into consideration gives the following expression for the Townsend discharge current:

$$I = \frac{I_0 e^{\alpha L}}{1 - \gamma(e^{\alpha L} - 1)}. \quad (4.4)$$

Note that the discharge current still depends on an external source I_0 , however, the expression in equation (4.4) becomes theoretically infinite as the denominator tends to zero. This leads to the Townsend criterion for electrical breakdown in gases between parallel electrodes:

$$1 - \gamma(e^{\alpha L} - 1) = 0. \quad (4.5)$$

When this criterion is satisfied (at point **E**) the gas transitions from a non-self sustaining to a self-sustaining discharge, i.e. the discharge becomes independent of the external source I_0 when $\gamma e^{\alpha L} = \gamma + 1 \approx 1$. Physically, $\gamma e^{\alpha L}$ represents the number of secondary electrons emitted per primary electron; hence $\gamma e^{\alpha L} = 1$ implies that every electron emitted from the cathode produces another to replace it. The corresponding voltage at which this process occurs is called the breakdown voltage (V_b). Fig.4.3 displays how the current and voltage changes through the Townsend regime.

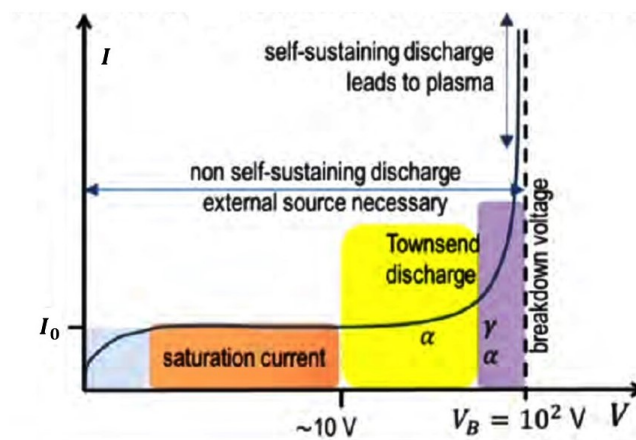


Fig. 4.3 Current-voltage evolution throughout the Townsend regime.

The current may increase by a factor of $10^4 - 10^8$ after the breakdown voltage V_b , however, the increase in current is largely dependent on the internal resistance of the power supply. If this resistance is too high, the discharge tube will be unable to draw sufficient current to initiate breakdown. In contrast, if the internal resistance is relatively low, the gas will breakdown at the voltage V_b .

4.1.2 Paschen's law

Recall Townsend's first ionisation coefficient, α , which describes the number of ionising collisions per electron, per unit length along E . It can be shown that:

$$\alpha = Ap \exp\left(-\frac{Bp}{E}\right) = Ap \exp\left(-\frac{BpL}{V}\right), \quad (4.6)$$

where p is the gas pressure and E represents the electric field (for two parallel electrodes: $E = V/L$). The coefficients A and B are experimentally determined and remain roughly constant over a range of pressures and fields for a specific gas type (refer to [9]).

Now, considering the criterion for electrical breakdown of a gas: $\gamma e^{\alpha L} = \gamma + 1 \implies \alpha L = \ln\left(1 + \frac{1}{\gamma}\right)$ and substituting α (at $V = V_b$) into this expression yields:

$$ApL \exp\left(-\frac{BpL}{V_b}\right) = \ln\left(1 + \frac{1}{\gamma}\right), \quad (4.7)$$

an expression for the breakdown voltage is obtained by rearranging equation (4.7):

$$V_b = \frac{B \cdot pL}{\ln(A \cdot pL) - \ln[\ln(1 + 1/\gamma)]}. \quad (4.8)$$

The expression above shows that for a particular gas and electrode material, the breakdown voltage V_b depends on the product of the gas pressure p and the distance L between the electrodes. This is known as Paschen's law. Fig. 4.4 shows Paschen's law for some common gases (with $\gamma = 0.1$).

Equation (4.8) holds true only if the radius of the electrodes is much larger than the inter-electrode distance (i.e. when $L/R \rightarrow 0$) [62]. However, many gas discharge devices, including the thruster concept to be studied here, have inter-electrode gaps comparable to the electrode radii. In these cases the loss of charged particles to the lateral walls of the tube must be con-

sidered when characterising the breakdown criteria for the working gas. Taking these losses into consideration, one obtains an expression for the breakdown voltage V_b that depends not only on L and R independently but also on the ratio L/R . Consequently, the breakdown voltage is expressed as a function of pL and L/R , i.e. $V_b = f(pL^*, \frac{L}{R})$, where L^* also depends on L/R , as demonstrated in equation (6) in [62].

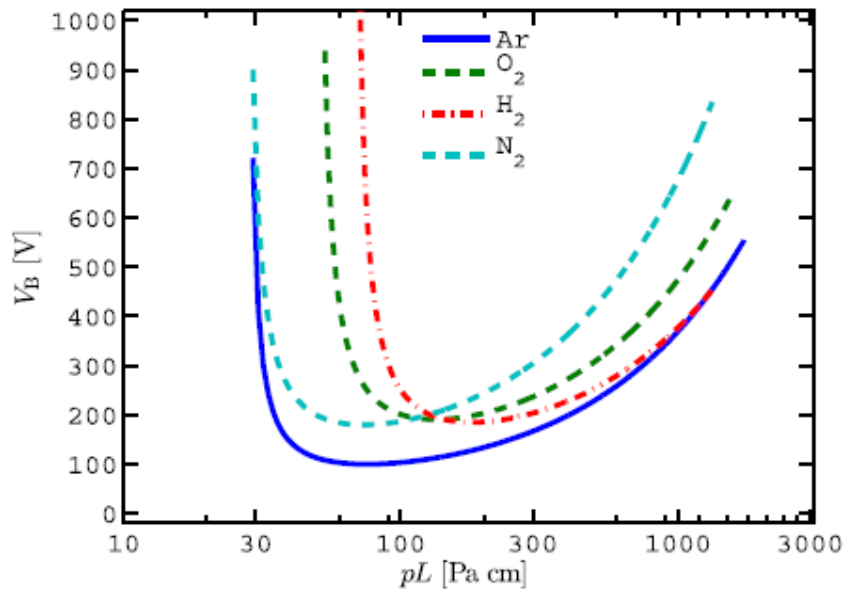


Fig. 4.4 Relationship between the breakdown voltage and the product of pressure and distance in a discharge tube for various gases [9].

The Paschen curves shown above demonstrate that for a fixed discharge length L there exists an optimum pressure where breakdown can occur. Each gas displays a unique Paschen curve however, a general trend is observed for all gas types.

4.1.3 Anatomy of normal glow discharge

After electrical breakdown has occurred the gas transitions into the normal glow discharge regime (region **F- G** in Fig.4.2). The ionised gas becomes luminous (hence the word "glow") as the electron energy and number density is now high enough to produce visible light through excitation collisions. The characteristic colour of the discharge depends strongly on the working gas, gas pressure, applied voltage and the electrode material. In this region the voltage is almost entirely independent on the current over many orders of magnitude. At lower currents the plasma is only in contact with a small fraction of the cathode's surface. As the current is increased the plasma occupies a greater fraction of the cathode's surface until

the entire cathode surface is covered by the plasma (at point **G**).

The low pressure glow discharge displays visual features consisting of several distinct regions with variations in both colour and luminosity as seen in Fig.4.5.

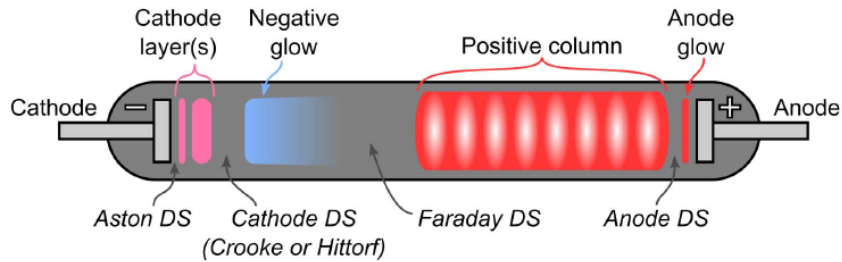


Fig. 4.5 Schematic showing the visual features of a low pressure glow discharge [9].

- The vast majority of the tube is filled with a uniform intensity glow called the **positive column**. This region consists of a quasi-neutral plasma which acts as a conducting path from the negative glow region to the anode.
- There are also regions near each electrode where the light intensity is non-uniform. At the cathode end there may be several alternating light and dark layers depending on the current and gas pressure.
- The first layer next to the cathode is called the **Aston dark space** [9]. Secondary electrons, emitted from the cathode, accumulate in this region creating a negative space charge and a strong electric field within the region.
- The **cathode glow** region follows the Aston dark space and is characterised by its relatively high ion density. In this region the secondary electrons are accelerated to high velocities towards the anode.
- The **cathode dark space** consists predominantly of ions which are accelerated towards the cathode. The space charge is positive and the electric field is moderately high in this region.
- The **negative glow** region follows the cathode dark space and displays the highest light intensity across the entire discharge. In this region excitation and ionisation collisions occur, resulting in a high electron density but a relatively low electric field.
- The negative glow is followed by the **Faraday dark space** where the electron energy is too low for atom excitations and recombination with ions, which leads to the characteristic darkness observed.

- At the anode, a region called the **anode glow** exists and has a brighter intensity than the positive column. A dark layer called the **anode dark space** occurs between the end of the anode glow and positive column. It has a negative space charge due to the flow of electrons from the positive column to the anode.

Abnormal Glow and Glow-to-Arc Transition (GAT)

Within the normal glow region of the glow discharge, the discharge voltage (otherwise called the cathode fall) remains constant as current increases substantially, however, at some point the cathode fall needs to increase to supply additional current. When this happens the discharge moves into the **abnormal glow region (G- H)**, where the discharge current is again dependent on the voltage. Further increases in current leads to a transition into the **arc discharge regime**. At **H** the **glow-to-arc** transition occurs, where the cathode fall goes from a cold discharge, depending primarily on Townsend ionisation processes, to a hot cathode discharge where thermionic emission from the cathode becomes significant.

4.2 Argon Glow Discharge Simulation

As discussed in the previous chapter, collisional processes occurring within a plasma involve three major species; electrons, ions and neutrals. These collisional processes are rather complex and difficult to describe analytically. Computer simulations are therefore required to extract useful information on the various plasma properties of interest.

A simple one-dimensional DC glow discharge simulation was created using COMSOL Multiphysics 5.5 [63]. The purpose of the simulation was to identify the spatial variation of the plasma potential, the particle densities and current densities along the axis of a DC glow discharge. These plasma properties are of significance since they determine the electric field characteristics across the discharge gap, which subsequently affects the net thrust of the system. Furthermore, these plasma characteristics can be used as a guideline for optimal thruster design.

Simulation parameters

Argon will be used as the working gas for all experimental tests to be conducted in this research. High purity argon is easily accessible and exhibits a lower breakdown voltage relative to other gases like nitrogen and oxygen. Furthermore, argon is frequently employed as the filling gas in many glow discharge experiments, hence there is an extensive body of

literature on argon glow discharges which may be used to develop insights on the various experiments to be conducted.

Table 4.1 summarises the key parameters used to generate the simulation. These simulation parameters were chosen as they were similar to the actual parameters applied in the preliminary experiments (see chapter 6).

Table 4.1 Plasma parameters used in Argon glow discharge simulation

Variable	Expression	Unit
Electron mobility (μ_e)	1.0×10^{24}	$(V \cdot m \cdot s)^{-1}$
Applied voltage (V_0)	750	V
Pressure (p_0)	0.9	Torr
Discharge length (L)	4	cm
Surface work function	5	-
Secondary electron coefficient (γ_e)	0.35	-

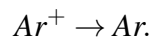
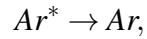
Neutral gas atoms (Ar) are the most abundant species in a low pressure argon glow discharge. This simulation takes into account the dominant collisional processes which occur between electrons (e), neutral argon atoms (Ar), excited argon neutrals (Ar*) and argon ions (Ar⁺). A summary of the reactions considered is provided in Table 4.2. For simplicity, it is assumed that only singly charged ions are present within the plasma.

Table 4.2 Collisional reactions modelled in the simulation [12]

Reaction	Description	$\Delta \epsilon$ (eV)
$e + \text{Ar} \rightarrow 2e + \text{Ar}^+$	Direct Ionisation	15.8
$e + \text{Ar}^* \rightarrow 2e + \text{Ar}^+$	Stepwise Ionisation	4.24
$e + \text{Ar} \rightarrow e + \text{Ar}^*$	Excitation	11.5
$e + \text{Ar} \rightarrow e + \text{Ar}$	Elastic Scattering	0
$e + \text{Ar}^* \rightarrow e + \text{Ar}$	Superelastic Scattering	-11.5
$\text{Ar}^* + \text{Ar}^* \rightarrow e + \text{Ar} + \text{Ar}^+$	Penning Ionisation	-
$\text{Ar}^* + \text{Ar} \rightarrow \text{Ar} + \text{Ar}$	Metastable Quenching	-

The collision frequency for the stepwise ionisation, elastic and superelastic scattering is deduced from cross section information, whereas Townsend coefficients are used to determine the collisional frequency in the case of the excitation and direct ionisation reactions. Lastly, forward rate coefficients are used to characterise the final two reactions in Table 4.2.

In addition to the reactions listed above, the following surface reactions are also considered:



These surface reactions characterise the interactions between the species and the boundaries of the discharge (the walls).

Simulation Results

Plasma potential

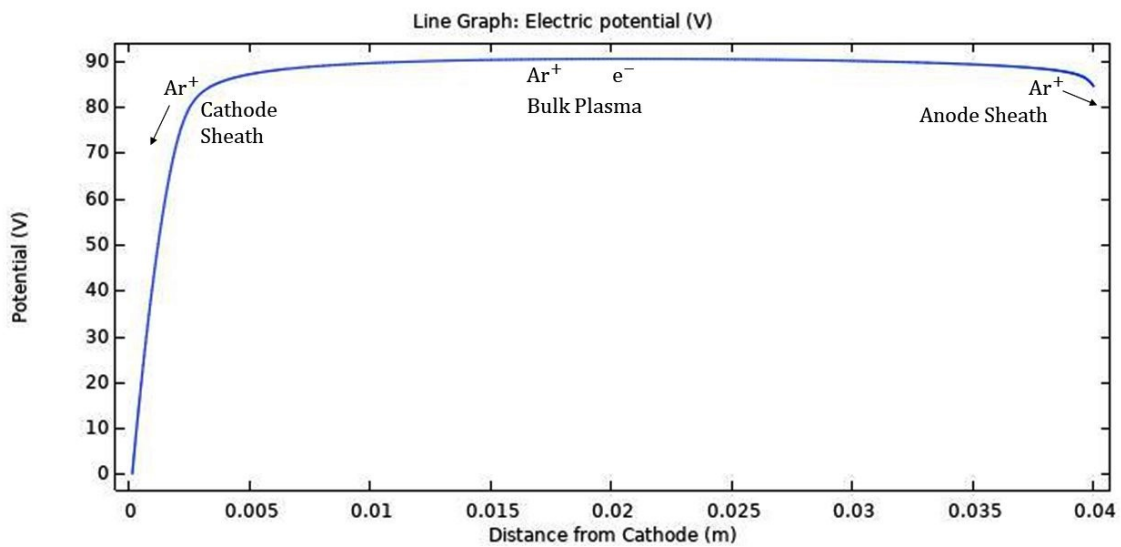


Fig. 4.6 Spatial variation of the plasma potential from the argon glow discharge simulation.

Fig.4.6 shows the steady-state plasma potential along the axial length of the discharge. Three important regions can be discerned from the figure, these are:

1. **The cathode sheath:** The positive argon ions entering this region are pulled towards the cathode and impact its surface with high energies. This region carries all of the potential difference V_0 between the electrodes [64]. The presence of ion-neutral collisions prevents the ions from gaining the full potential energy eV_0 .
2. **The bulk plasma:** Electrons are confined within this region due to the slight elevation in potential. It is here where the condition for quasi-neutrality is met.
3. **Anode sheath:** This region shares similarities with the cathode sheath but has a lower potential difference. Ions bombard the anode with lower energies than at the cathode.

The plasma potential profile indicates the presence of a large electric field in the cathode sheath region. It is due to this strong electric field that ions are able to bombard the cathode with high energies resulting in secondary electron emission. If the ions bombarding the cathode reach sufficiently high energies they can cause the cathode surface to heat up and emit electrons through thermionic emission.

Particle densities

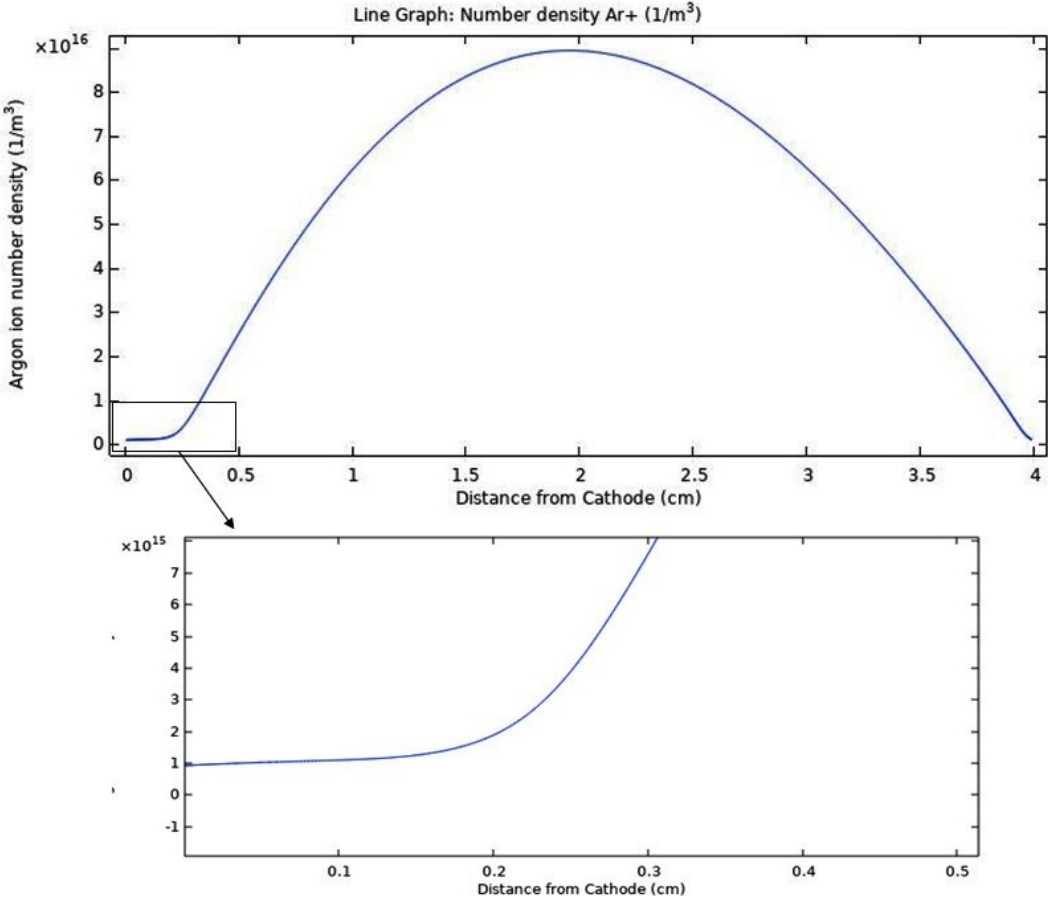


Fig. 4.7 Spatial variation of the argon ion number density from the argon glow discharge simulation.

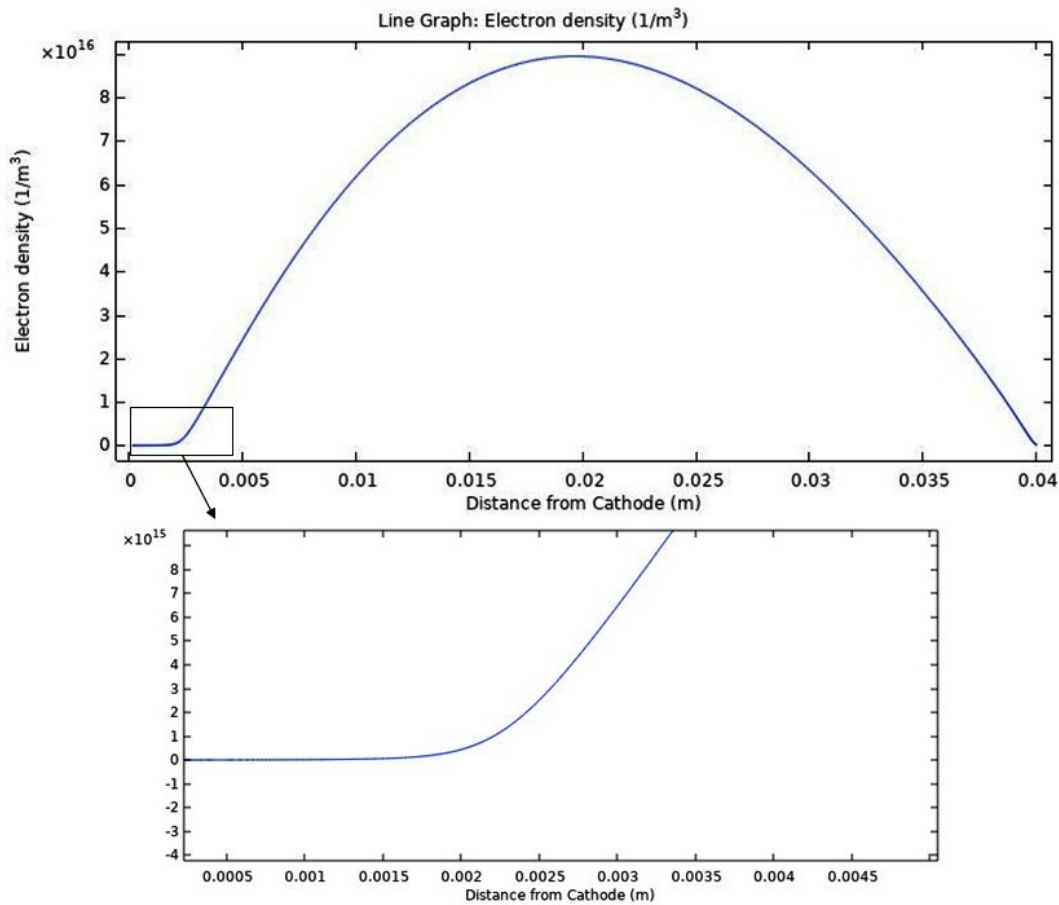


Fig. 4.8 Spatial variation of the electron number density from the argon glow discharge simulation.

Fig.4.7 and Fig.4.8 reveal the origin of the strong electric field within the cathode sheath region. Although not visible in the initial plot, a closer inspection into the cathode sheath region reveals a significantly higher ion density ($\sim 10^{15}$ particles per m^3) in comparison to the depleted electron density in the same region. This variation in particle densities results in a net-positive space charge within the sheath.

The ion and electron number densities within the bulk plasma are identical, satisfying the quasi-neutrality condition. Both the electron and ion densities peak halfway along the axial length of the discharge. This most likely corresponds to the region between the cathode fall and positive column ¹

¹Note that this simulation did not account for the diffusive loss of electrons to the walls, and the surface charge accumulation on the walls of the discharge was not modelled.

Excited argon mass fraction

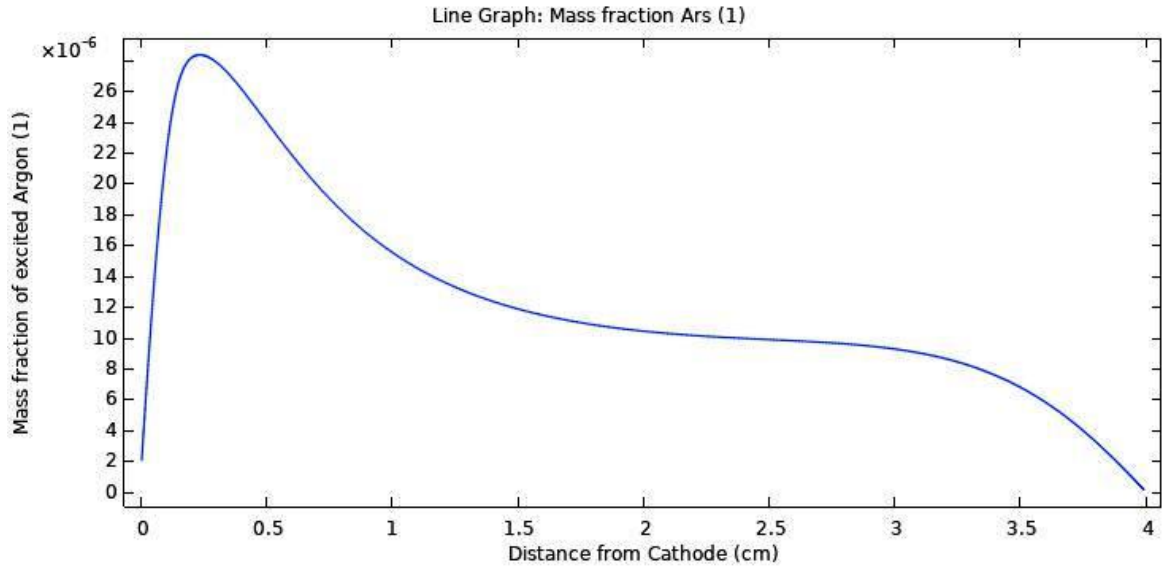


Fig. 4.9 Spatial variation of the argon mass fraction (denoted as Ars) from the argon glow discharge simulation.

According to data for the collision cross sections generated by Phelps [65], the cross sections for electron impact ionisation and argon excitation occur within the same energy envelope [64]. It can then be inferred that regions with high degrees of ionisation coincide with regions of high excitation. Since high degrees of excitation result in light emission, it is expected that regions with high levels of electron impact ionisation should also be optically visible. Fig.4.9 shows how the excited argon mass fraction varies spatially along the discharge. The peak is observed to occur within the cathode sheath region.

Electron temperature

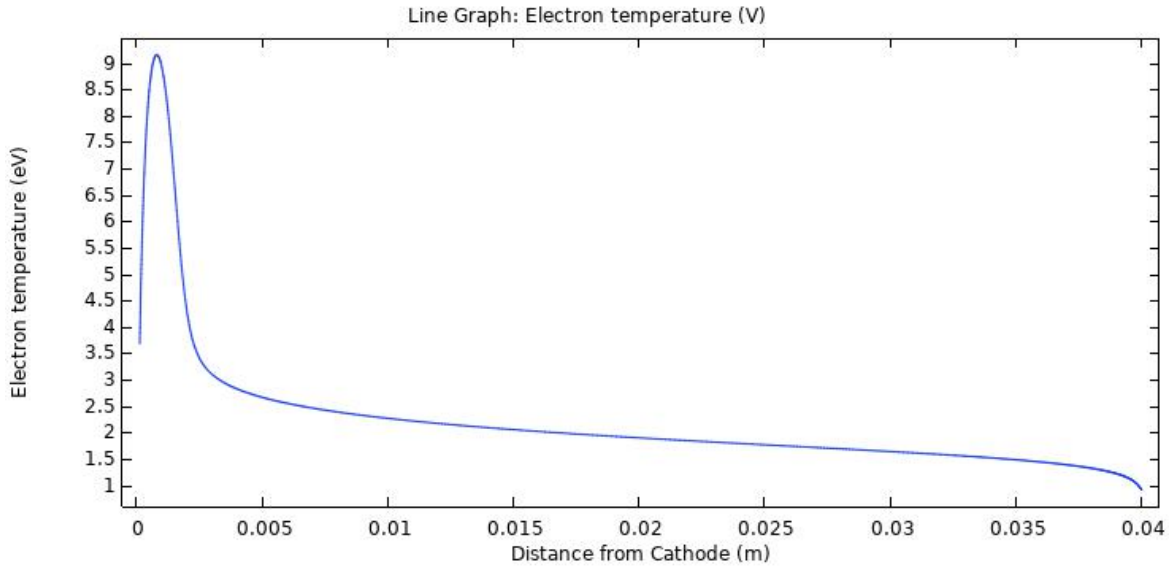


Fig. 4.10 Spatial variation of the electron temperature from the argon glow discharge simulation.

Fig.4.10 shows how the electron temperature varies along the axial length of the discharge. Electrons emitted from the cathode are accelerated to high velocities towards the bulk plasma. A high intensity cathode glow region forms when the electrons have reached the optimum energy for excitation/ionisation. The electric field then begins to decline and the electron temperature begins to fall. This causes the excitation/ionisation rate to decrease, resulting in the formation of the Crookes/cathode dark space. Once the electrons enter the bulk plasma the electric field is too weak to accelerate them further (as verified by the low electron temperature observed in this region). At this point elastic scattering between the electrons and neutrals dominates and causes the electrons to be attenuated, producing an intensely bright negative glow region. Another dark region, called the Faraday dark space, then follows the negative glow. This region also has a low electron energy. As the electrons are unable to excite the argon atoms they begin to recombine with the ions. The electric field and electron energy continue to diminish along the positive column as electrons continue to flow towards the anode. Near the anode a negative space charge forms as the electrons are attracted towards the positive electrode, and ions are repelled. The accelerated electrons are capable of exciting argon atoms within the vicinity resulting in the formation of the anode glow region.

Ion and electron current densities

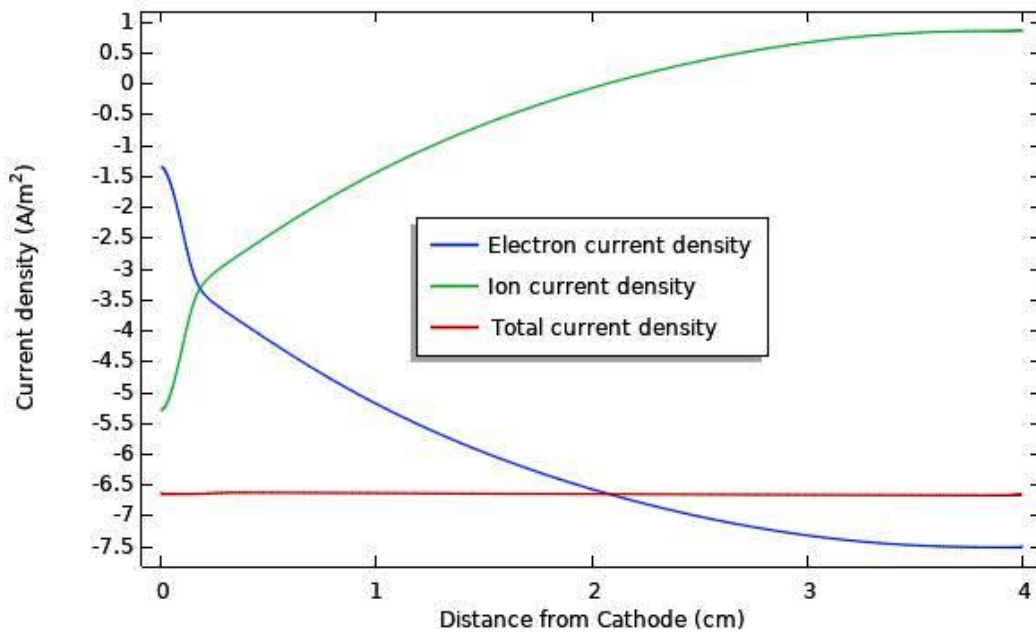


Fig. 4.11 Spatial variation of the electron, ion and total current density from the argon glow discharge simulation. The current densities are negative as the current vector and electrode surface normal are in opposite directions.

The current density of electrons and ions is shown in Fig.4.11. The ion current density is large in the cathode region and sharply increases in the cathode fall region. Secondary electrons released from ion bombardment at the cathode produce a small electron current. The total electron current then increases in the cathode fall region as more electrons are produced from the high electron temperature in this region. Each secondary electron needs to produce some minimum threshold of ions to maintain the discharge. This largely depends on the secondary electron emission coefficient γ_e . The total discharge current I_d at the cathode is the sum of the ion current I_i and electron current I_e :

$$I_d = I_i + I_e = I_i(1 + \gamma_e). \quad (4.9)$$

This equation verifies that the ion current makes up the greater fraction of the total discharge current at the cathode, however, beyond the cathode fall region the electron current density rises, due to the generation of new electrons from impact ionisation with argon atoms.

Therefore, in all of the other regions of the discharge the current is almost entirely carried by electrons.

Summary and concluding statements

The basic theory of glow discharges and the underlying mechanisms involved in the breakdown of low pressure gases was introduced. Paschen's law, an expression relating the breakdown voltage with the product of the electrode separation distance and working gas pressure was then deduced. The anatomy of a typical glow discharge was studied in detail through computer simulations of an argon glow discharge. These simulations gave insight into how the various plasma parameters; like the plasma potential, particle number density, excited argon mass fraction, electron temperature, and particle current density, varied along the axial length of the discharge. The information gathered from these simulations are vital towards understanding the plasma characteristics within the discharge channel of the thruster and will serve to provide insights into the behaviour of the system in the experimental sections of this research (chapters 6 and 7). Although these simulations were conducted on a closed discharge the fundamental characteristics of the profiles should not be greatly influenced when orifices are introduced at the electrodes. Characterising the exact behaviour of the discharge with open electrodes, including the V-I relationship, and determining the thruster's suitability to be used as a micropropulsion mechanism will be the main scope of this research. The next chapter will introduce the materials selection and apparatus used in the experimental tests which follow.

Chapter 5

Materials and Experimental Apparatus

Having laid the foundations for the operating mechanism of the modified DC discharge microthruster concept as introduced in Chapter 1 (refer to Fig.1.5) it is now time to introduce the materials and apparatus used in this research.

Optimal thruster design parameters

Four factors that are of crucial importance in the design of the thruster are:

1. The electrode and thruster body material.
2. The overall geometry of the electrodes and thruster body.
3. The type of working gas (propellant) to be used.
4. The pressure of the working gas.

5.1 Materials

5.1.1 Electrode and thruster body material selection

Stainless steel was selected as the electrode material for its proven durability in harsh environments. Previous tests on the DC discharge microthruster utilised polylactic acid (PLA) as the material for the thruster body. It was hypothesised that the high temperatures from the discharge or the grounded electrode had caused the interior of the discharge channel to heat up, which led to the blocking of the channel from the subsequent build-up of debris. The author in [2] noted that the use of PLA as a construction material was not the most appropriate

choice especially in the context of space propulsion systems. In this research the thruster body was constructed from aluminium oxide ceramic material to mitigate the aforementioned problems. Ceramics are used extensively in aerospace design and manufacturing applications and provide many favourable features, including hardness, high resistance to abrasion, and the ability to withstand high temperatures without damage or deformation [66].

5.1.2 Geometric considerations

The thruster needs to be small enough to meet the size constraints of small satellites, it also has to have a large enough radius to facilitate the addition of apertures on the surfaces of the electrodes. A tube length of 40 mm and an inner diameter of 10 mm was found to be appropriate to meet these requirements. Additionally, a 4 mm hole was drilled halfway along the length of the tube to allow for the gas to enter the tube. Two teflon endcaps, both 10 mm in length, were constructed to shield the outer surface of the electrode to prevent unwanted arcing on the outside of the tube and to allow for easier attachment of the high voltage (HV) cables to the electrodes. The electrodes were cut into octagonal geometries and measured to be 15 mm in length and width. The octagonal geometry was selected to facilitate the attachment of the electrodes to the open ends of the tube using a vacuum compatible adhesive. In the case of the open electrodes, extreme care was taken to ensure that the orifices were symmetrically aligned with each other on both ends of the tube.

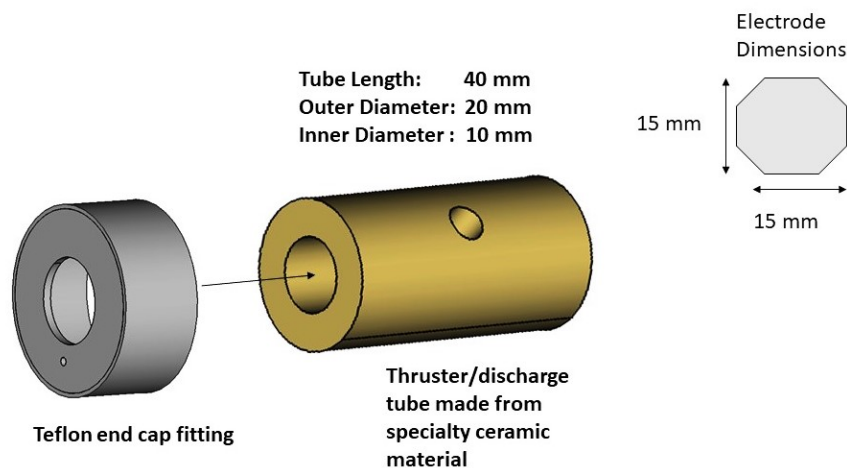


Fig. 5.1 Geometry of the discharge tube (thruster body), end cap fittings and electrode dimensions used in this research. Note that the dimensions were measured using a vernier caliper which gives a reading error of 0.05 mm and thus the actual dimensions are accurate to ± 0.05 mm to those quoted above.

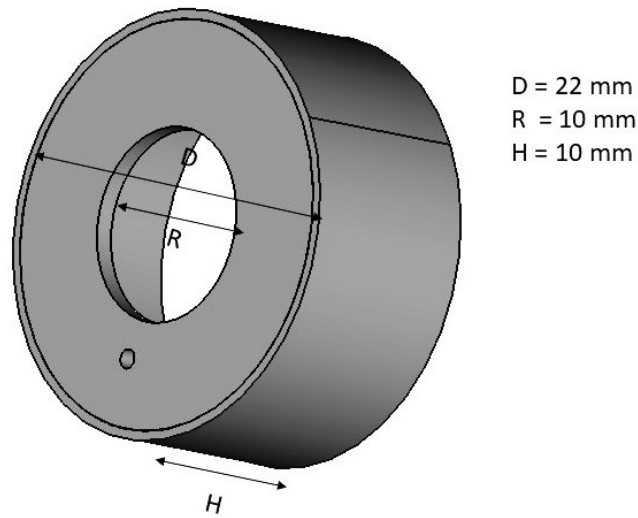


Fig. 5.2 Dimensions of the teflon endcaps used to shield the outside of the electrodes from unwanted electrical arcing.

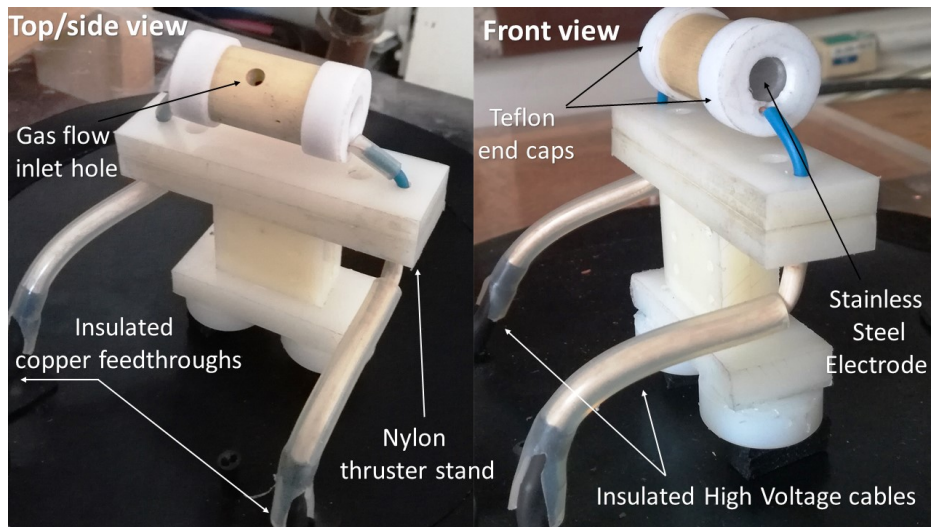


Fig. 5.3 Image of the thruster mounted on the thruster stand.

To allow for charged particles to escape the thruster and generate the desired thrust, the addition of apertures at each of the electrodes is required. In the preliminary experiments, four different sized apertures were tested to ascertain the relation between the electrode aperture size and the behaviour of the thruster. Using a larger orifice would allow more ions to escape and therefore produce greater thrust. However, it would also result in a decreased electrode surface area which would subsequently decrease the secondary electron emission rate and thus negatively impact the ionisation efficiency of the system.

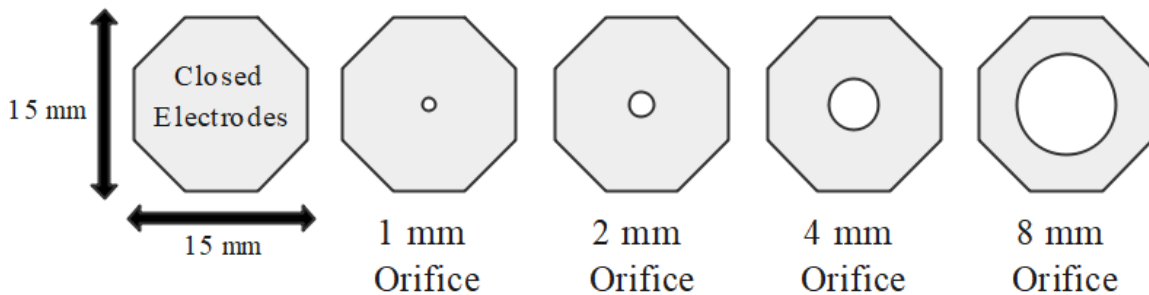


Fig. 5.4 The various electrode configurations used in the preliminary experiments. The error in the orifice diameter is estimated to be ± 0.1 mm, arising from the machining process.

5.1.3 Selection of propellant gas

Generally, electric propulsion systems utilise propellant gases that are inert, to limit degradation of the thruster body and the electrodes through corrosion, ones that have high mass densities, to generate greater thrust, and those that have low ionisation energies, allowing for ease in the ionisation of neutral propellant atoms are desired [19]. In most cases xenon is used, as it fits all of the above criteria. However, xenon is expensive and not easily accessible. Therefore, argon was used as the working gas for all experimental tests to be conducted in this research. Argon gas is easily accessible and exhibits a lower breakdown voltage relative to other gases like nitrogen and oxygen. Furthermore, argon is frequently employed as the filing gas in many glow discharge experiments and hence there is an extensive body of literature on argon glow discharges which may be used to develop insights on the various experiments to be conducted.

5.2 Experimental Apparatus

5.2.1 Vacuum chamber

The preliminary experiments were conducted inside a 270 mm wide x 200 mm high glass vacuum chamber, placed on top of an acrylic base plate. Several holes of varying sizes were drilled through the plate to facilitate the necessary vacuum connections, i.e. the vacuum pipe connection, gas flow inlet connection and the copper feedthrough connections. The copper feedthroughs were sealed with silicone and high voltage cable insulation to prevent electrical leakage. A rubber o-ring/vacuum gasket, lubricated with vacuum grease, was used to secure the glass chamber to the base plate and to prevent gas leakage when evacuating the chamber down to low pressures.

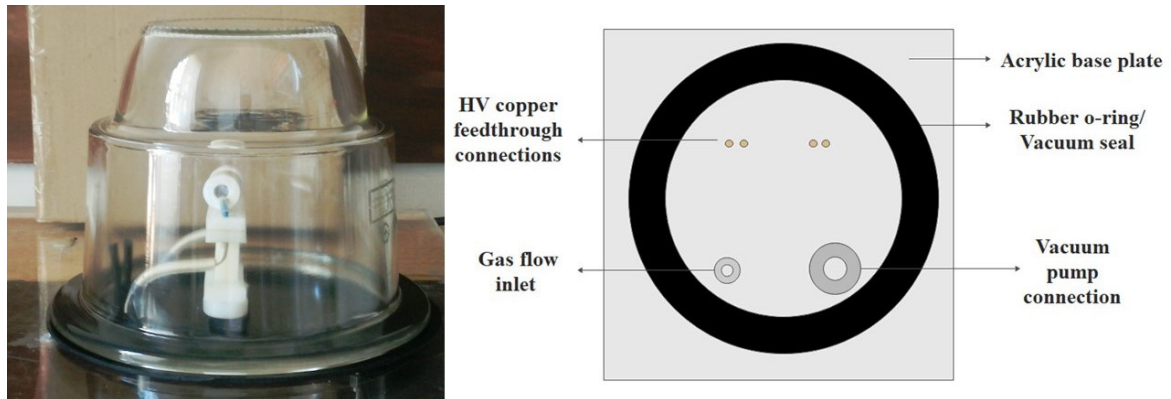


Fig. 5.5 Glass vacuum chamber used in preliminary experiments (left) and base plate design (right).

The subsequent experimental tests were conducted in a larger (760 mm diameter x 200 mm high) stainless steel ring vacuum chamber. The chamber's hemispherical lid was easily opened and sealed with the aid of a mechanical hoist. Anti-vibration pads, located at the base of the chamber and the frame, allowed the entire structure to be mechanically isolated. A series of access ports were located along the circumference of the chamber. These ports allowed for easy access into the interior of the chamber through various interfaces.

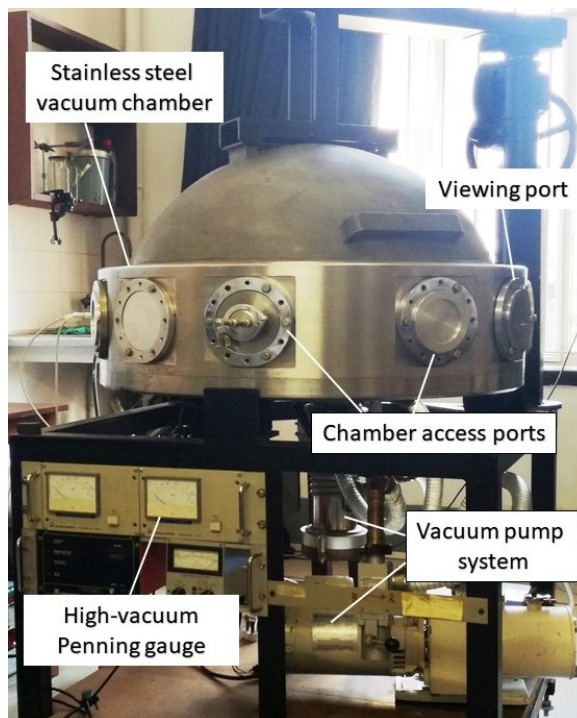


Fig. 5.6 Stainless steel vacuum chamber used in the experimental tests proceeding the preliminary studies.

5.2.2 Vacuum pump system

A vacuum pump system was used to create an artificial space environment within the chamber. The system was comprised of an Alcatel dual stage rotary roughing pump and a Leybold-Heraeus water cooled diffusion pump.¹ Initially, the roughing pump was used to obtain a soft vacuum (~ 0.05 Torr) within the chamber, after which, the diffusion pump was used to pump the chamber down to $\sim 10^{-5}$ Torr. A Kurt J. Lesker 275i digital vacuum gauge was used to monitor the pressure of the soft vacuum and a Leybold-Heraeus PM 41 Penning vacuum gauge was used for the high vacuum pressure measurements.

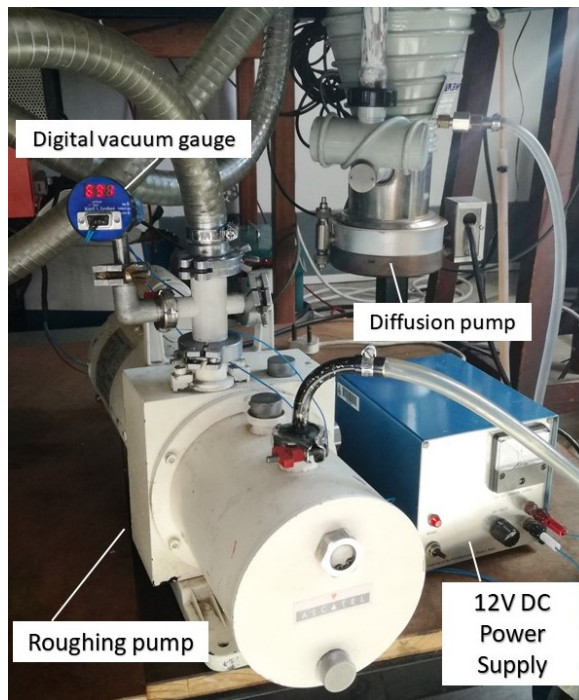


Fig. 5.7 Vacuum pump system used to obtain an artificial space environment.

5.2.3 Power supply

A Hivolt T1EP 100 605 p high voltage power supply was used to initiate and sustain the electrical discharge. The power supply was able to deliver a maximum output voltage of 10 kV and a maximum current of 6 mA. The control dials on the front panel were used to regulate the applied voltage and discharge current and allowed for voltage and current limits to be set independently. The HV toggle switch, acting as a current restricting resistor, on the front panel allowed for the fast deactivation of the high voltage when required.

¹The preliminary experiments only utilised the roughing pump.



Fig. 5.8 High voltage DC power supply used in all experimental tests conducted in this research.

5.2.4 Oscilloscope

Measurements of the ion current density emanating from the thruster were made using a Rigol DS5022M 2-channel digital oscilloscope. This was accomplished by measuring the voltage drop across a resistor connected to an aluminium plate located along the path of the ejected ion beam current. More details on this procedure can be found in chapter 7.



Fig. 5.9 Oscilloscope used to indirectly measure the ion beam current density.

5.2.5 Micro-controller and current sensor board

In all experiments conducted in the larger vacuum chamber, a micro-controller coupled with an INA2019 current sensor breakout board was used to facilitate a higher accuracy in the measurements of the discharge current at the cathode. The sensor consisted of a precision amplifier, with a maximum input difference of ± 320 mV, which measured the voltage drop across a 0.1Ω (1%) sense resistor. The sensor was capable of measuring a maximum current of ± 400 mA with a resolution of 0.1 mA.

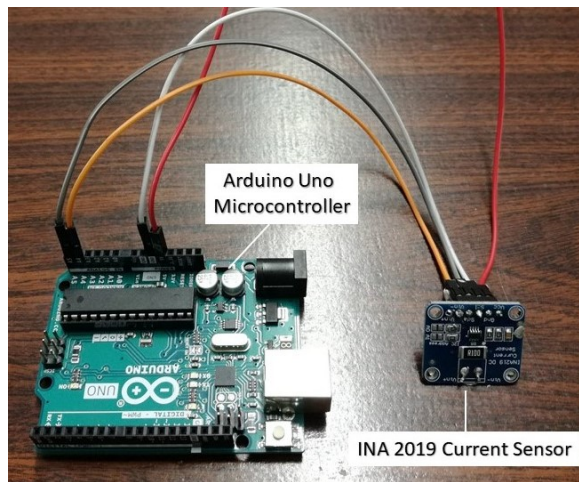


Fig. 5.10 Micro-controller and current sensor setup used to obtain more accurate measurements of the the discharge current.

5.2.6 Mass flow measurement system

For the experiments in the larger chamber, an in-house mass flow measurement system, inspired by the orifice flow meter concept [67], was developed to measure very small propellant mass flow rates to the thruster. This system consisted of two hollow aluminium chambers separated by an aluminium plate. Rubber gaskets were placed on both sides of the aluminium (orifice) plate to ensure an airtight seal. Two pipes were attached to the opposite ends of the chambers. The inlet pipe was connected directly to the gas flow pipe running to the argon cylinder, while the outlet pipe was attached to a micrometer needle valve. This valve was used to control the downstream flow rate of the gas into the chamber, and subsequently connected to the vacuum chamber through one of the chamber's access ports. A small aperture, 0.5 mm in diameter, was made at the centre of the aluminium plate. The low pressure vacuum from the chamber established a pressure difference (ΔP) between the two chambers, on either side of the orifice plate, and facilitated gas flow through the system. This pressure difference was then measured using an Extech HD750 Differential

Pressure Manometer. The relation between the mass flow rate and differential pressure was deduced from the following equation:

$$\dot{m} = C_f A_0 \sqrt{2\rho\Delta P}, \quad (5.1)$$

where C_f is the orifice flow coefficient, A_0 is the aperture area and ρ is the density of the propellant gas at room temperature ($\sim 300\text{K}$). See Appendix C for a detailed derivation of equation (5.1).

The above expression was then used to produce a calibration curve that allowed for the mass flow rate to be determined from a measured pressure differential. This was accomplished by measuring the time taken for the vacuum to displace a fixed amount of argon gas from a 50 ml burette upturned in a beaker of water. The method measured the mass flow rate in ml/s, which was then multiplied by the density of argon at room temperature to produce a mass flow rate in kg/s. The exact details and results of this procedure can be found in Appendix C.

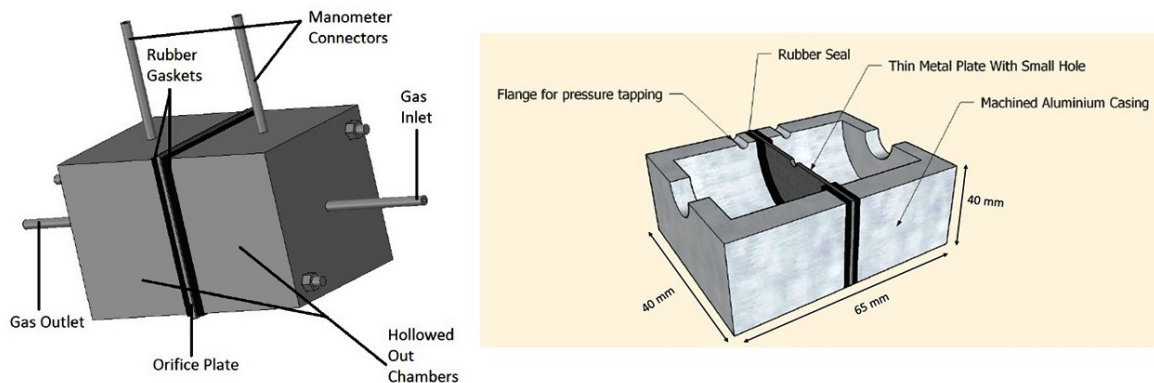


Fig. 5.11 Schematic and cross section through the orifice plate box used in the mass flow rate calibration process. Images taken from [10] and [2].

5.2.7 Optical Microscope

A SteREO discovery V8 optical microscope, with parfocalled achromatic optics and a maximum magnification of 8X, was used to obtain images of the electrode surfaces to assess the damage and erosion resulting from the experimental tests. Images were obtained through the ZEN imaging software package.

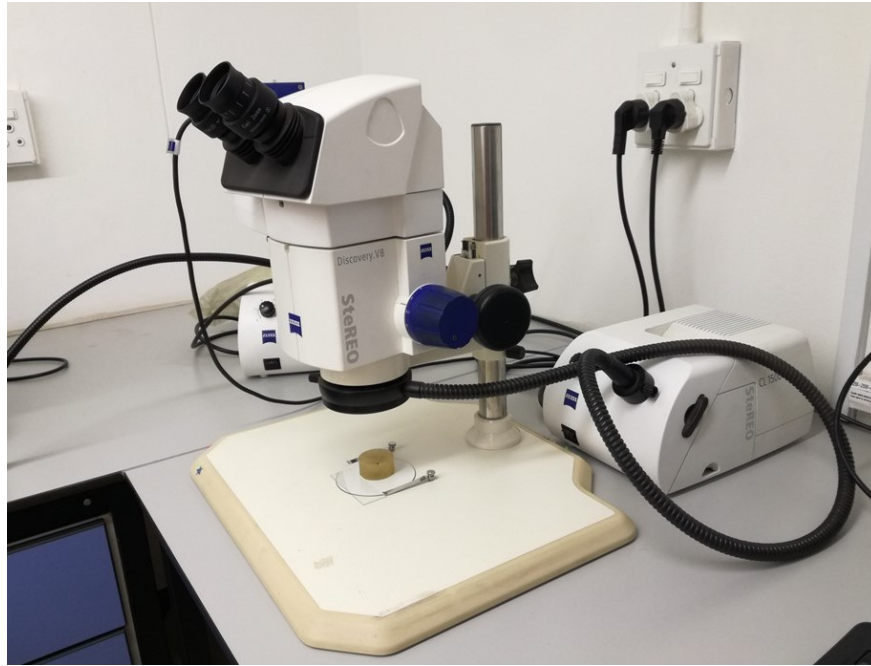


Fig. 5.12 SteREO V8 microscope used to study the surface features of the electrodes after conducting the experiments.

This concludes the list of materials and experimental apparatus used throughout this research. The next chapter covers the theory and results of the preliminary experimental tests.

Chapter 6

Preliminary Experimental Tests

6.1 Introduction

Prior to studying the proposed thruster concept in detail (for example conducting plasma diagnostics and thrust measurements) one first needs to verify the system's working principle and identify any major challenges or drawbacks that the system may have. It is therefore important to conduct preliminary studies to simulate the working conditions and to identify the system's stable operating parameters. These preliminary experiments were conducted inside a smaller glass vacuum chamber. The smaller chamber allowed for faster evacuation, and its high transparency gave a clearer view of the thruster, making it easier to characterise the qualitative features of the discharge. A direct gas feed into the thruster was not required in these preliminary tests as the smaller chamber was meant to simulate the pressure of the working gas inside the thruster tube. From this, the optimal working gas pressure could be deduced.

In the preliminary experiments, four different sized apertures were tested to investigate the relation between the electrode aperture size and the electrical behaviour of the thruster. Two competing hypotheses are presented below for which the experiments that follow will either support or refute:

1. Increasing the size of the electrode aperture significantly influences the system's electrical characteristics. The system's V-I characteristics change in proportion to changing the aperture size.
2. Alternatively, the increase in aperture size may have no significant effect on the electrical characteristics of the system, i.e. the thruster will display identical voltage-current behaviour regardless of the aperture size used.

6.2 Theory

The thruster concept studied here can be viewed as a quintessential ion source consisting of a plasma and an accelerator (more commonly called an extractor). The plasma is produced through the electrical breakdown of a gas between an anode and a cathode, with the cathode acting as the ion accelerator/extractor in this context. Full details of this process was presented in Chapter 4 and the optimal design parameters, along with the material selection, for the thruster concept was presented in Chapter 5.

The ions produced from the plasma flow towards the extractor, producing an energetic ion beam. To produce an ion beam of energy E_i , the plasma source must be biased to a positive voltage. A high voltage power supply provides the means for biasing the plasma. This power supply can also be called the accelerator supply, as it determines the ion acceleration voltage V_a (or discharge voltage). Fig.6.1 illustrates this concept.

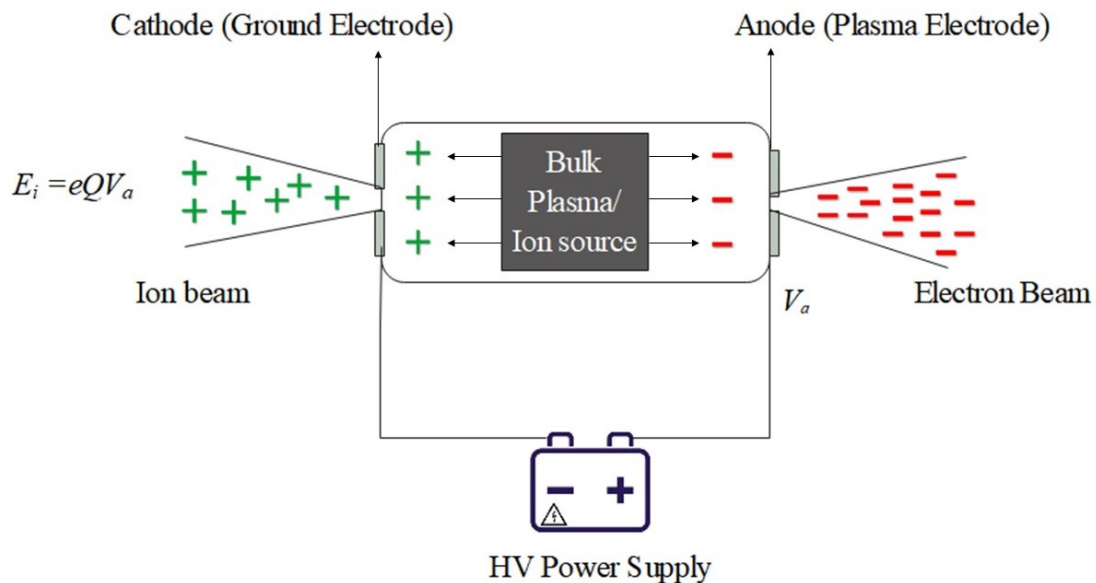


Fig. 6.1 Thruster concept viewed as a quintessential ion source.

The anode (also called the *plasma electrode*), is biased with a positive high voltage, the acceleration voltage, while the cathode (the *ground electrode*) is fixed at ground potential. The resulting electric field between the electrodes acts as the acceleration mechanism, allowing the ions to flow to the extractor.

Ion beam properties

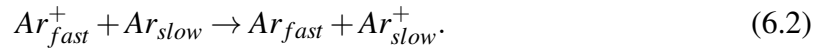
The parameters of the beam are dependent on the plasma source, the extractor electrode and the overall system geometry. The size and shape of the ion beam is largely determined by the geometry of the extractor electrode. Usually circular single aperture extractors are used to generate narrow focused beams and larger or multiple apertures are used for broader beams [11].

The ion beam current and ion beam energy are parameters of great interest. The energy per ion in the extracted beam is given, to good approximation, by the product of the ion charge state Q and the acceleration voltage:

$$E_i = eQV_a. \quad (6.1)$$

In the context of low energy ion sources, the ions may be produced at a potential that is offset from V_a by the plasma potential V_{plas} (i.e. the potential of the plasma relative to its boundaries). Typically, when the acceleration voltage is of the order of a few kV the plasma potential can be neglected to a good approximation [11].

In high vacuum conditions ($> 10^{-6}$ Torr) the ions within the beam may propagate without significant losses in energy through collisions with ambient gas particles. However, in the experimental setup that follows the vacuum chamber pressure is much softer ($\sim 10^{-1}$ Torr) and it is expected that the ions within the beam will collide with the neutral background gas and subsequently lose some energy. The ambient gas pressure may also significantly affect the total ion current within the beam. In this case, the argon ions pass through a region of neutral argon atoms and experience charge-exchange collisions. These collisions between fast ions and neutral atoms produce fast neutrals and cold ions:



The ion beam current is also influenced by the electrons formed from the ambient ion-neutral collisions and the secondary electrons emitted from the extractor electrode surface. These low energy electrons form a background sea which remains in the positive space charge region formed by the beam. The sea of background electrons neutralises the repulsive forces of the positively charged ions and thus aids the propagation of the beam.

The size and quality of the extracted ion beam can be characterised by its emittance. The beam emittance gives a measure for the average spread of particle coordinates in position-and-momentum phase space. The authors in [68] have derived an expression for the normalised 4 rms emittance for 89% of a beam, emanating from a round aperture of radius r , as follows:

$$\epsilon_{norm,4rms,89\%} = 0.0653r\sqrt{\frac{kT_i}{m_i}} \sim 0.0653r\sqrt{\frac{E_i}{m_i}}, \quad (6.3)$$

where, r is the aperture radius in mm, T_i is the Maxwellian ion temperature and m_i is the ion mass in atomic mass units. Equation (6.3) shows that for a fixed beam energy, the beam emittance increases with an increasing aperture size.

Ionisation/energy efficiency

To ensure that the ion source remains energy efficient, one needs to maximise the extracted ion current relative to the current arriving at the cathode surface [11]. However, the ion source (discharge plasma) is sustained only through the emission of secondary electrons from ion bombardment at the cathode. Therefore, a trade-off exists between effective ion extraction and stable glow discharge operation [11].

For a uniform distribution of the ion current on the cathode surface, the ion extraction efficiency can be approximated by the ratio of the surface areas of the discharge plasma S_p and the cathode S_c [69]:

$$\alpha \sim \frac{S_p}{S_c}. \quad (6.4)$$

If S_p remains fixed while S_c decreases (as would be the case when increasing aperture size and or aperture number) the discharge voltage and gas pressure would need to be increased to compensate for this effect. The higher gas pressures required to sustain the discharge at high α values limits the extraction capabilities and energy efficiency of the system.

Sputtering and heavy ion bombardment

Inevitably, the cathode will experience heavy ion bombardment from the incident ions, resulting in the of sputtering of its surface. According to *Danilin et al.* this sputtering may result in a 10% energy loss for the accelerated ions. In addition, 70-90% of the ion's energy will be released as heat. In some metallic cathodes the sputter yield, for argon ions with

energies ranging from 400-800 eV, is usually between 0.5-1.0 atoms per ion [70]. Prolonged sputtering may cause electrode erosion and could significantly reduce the lifetime of the system. It is therefore important to select electrode materials that have a low sputtering yield.

6.3 Aims

- To verify whether the thruster concept works as hypothesised, according to the ionisation-acceleration coupling mechanism.
- To deduce the optimal operating parameters for a stable discharge and thruster operation.
- To investigate the effect of changes in electrode aperture size on the voltage-current characteristics of the system.
- To investigate any drawbacks and potential pitfalls in the current system design and experimental setup.

6.4 Apparatus

- Glass bell jar (vacuum chamber)
- Acrylic base plate fitted with various vacuum connections
- Hivolt T1EP: High voltage power supply
- High voltage cables
- Afrox Argon gas (propellant) Baseline 5.0
- Micrometer needle valve: for fine adjustment of pressure inside the chamber
- Gas shut-off valve
- Alcatel dual stage rotary vane roughing pump
- Kurt J.Lesker 275i low pressure vacuum gauge
- Carl Zeiss SteREO V8 Optical Microscope

6.5 Methodology

Experimental Setup

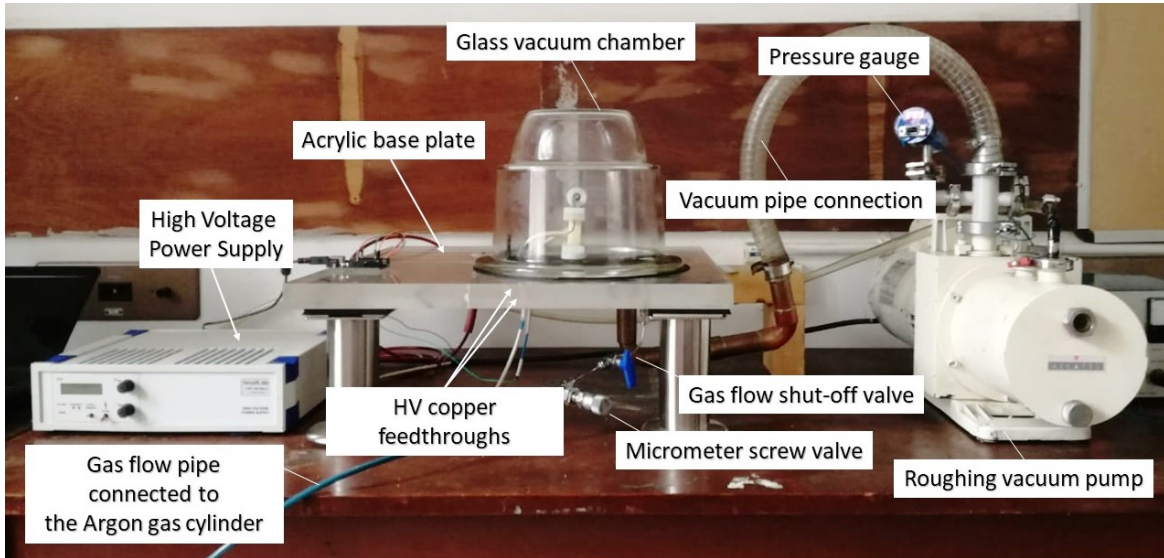


Fig. 6.2 Preliminary Experimental Setup.

The experimental setup is shown in Fig.6.2. The electrodes at each end of the thruster were connected to the high voltage power supply through high voltage cables via the copper feedthroughs from the base plate. A gas flow pipe, from the argon cylinder, ran to the gas flow inlet of the chamber. The pipe was connected to a micrometer needle valve, which was used to regulate the gas flow into the chamber along with a gas shut-off valve, that when closed would completely stop the flow of gas into the chamber. The roughing pump was connected through a vacuum pipe connection and used to evacuate the chamber. The pressure within the chamber was monitored using the low pressure vacuum gauge.

Creating a high purity argon atmosphere

To simulate the working gas pressure within the tube, an argon rich atmosphere was required to fill the entire chamber. This was accomplished by flushing the chamber with high purity (> 99.9 %) argon gas. Initially, the gas inlet valves were kept shut and the chamber was pumped down to low pressures (50 ± 5 mTorr). The pump was then switched off as the gas was allowed to flow into the chamber until the entire chamber was filled with argon gas and the pressure had reached equilibrium (i.e. the pressure inside the chamber was equal to atmospheric pressure). Once equilibrium pressure was obtained, the gas inlet valve connected

to the chamber was shut. At this point the chamber contained approximately 99% argon and 1% air. To get a higher purity argon atmosphere, the flushing procedure above was repeated for a second time. After flushing the chamber for the second time, the chamber contained approximately 99.9% argon and 0.01% air. This was deemed sufficient for the preliminary experiments.

Identifying the optimal stable operating pressure range

Since a high electrical efficiency is desirable, it is beneficial to exploit Paschen's law to obtain the optimal breakdown voltage of the gas at a particular pressure range. The authors of [62] had demonstrated a method to determine a breakdown curve for various gases (including argon) contained in a discharge vessel of arbitrary dimensions. Using this method, an experimental breakdown curve for argon gas in a cylindrical tube, with fixed dimensions: $L = 40.00 \pm 0.05$ mm and $R = 5.00 \pm 0.05$ mm, was produced by measuring the breakdown voltage within a confined discharge over a specific pressure range. For higher accuracy, the curve was produced by taking the average measurements from a number of trials. Thereafter, the optimal pressure range for stable discharge operation was deduced, and this was used as the operating pressure in all subsequent tests.

Measuring the V-I characteristics of a confined discharge in the optimal pressure range

Prior to investigating the effect of changing aperture size on the electrical behaviour of the system, one first needs to establish a baseline metric for comparison. In this context, the baseline is taken to be the voltage-current characteristics in a confined discharge tube with closed electrodes (i.e. no apertures).

After the high purity argon atmosphere had been established, the chamber was evacuated down to 0.05 Torr and the pump was left to run. The HV power supply was switched on and the output voltage was set to 1.20 ± 0.01 kV. The current was set to its minimum (0 mA). The argon gas flow was introduced and the pressure within the chamber was regulated using the micrometer needle valve. Once the desired pressure range was obtained where breakdown had occurred within the tube, as indicated by the voltage drop observed on the front panel of the HV power supply, the current was then slowly increased in increments of 0.500 ± 0.001 mA until the maximum current limit of 6.000 ± 0.001 mA was achieved. At each increment the discharge voltage (displayed on the front LCD panel of the power supply) was monitored for a period of 30 seconds. The gas flow was then shut and the current was adjusted back to zero. This procedure was repeated five times for averaging and

error analysis. The voltage-current characteristics in three different pressure ranges were measured.

Measuring the V-I characteristics of the discharge with open electrodes

The final set of preliminary experiments involved characterising the V-I relationship for a discharge with open electrodes (i.e. electrodes with apertures). These experiments were conducted to determine the optimal electrode aperture size for stable operation and to investigate the effect of changing aperture size on the electrical behaviour of the thruster. The above procedure for measuring the V-I characteristics for a confined discharge was repeated, only this time the electrodes had apertures ranging from 1, 2, 4 and 8 mm in diameter.

6.6 Results and Discussion

The results from the preliminary experiments are presented below. A detailed error analysis, including the origin of the uncertainties in measured quantities and the calculation of error bars can be found in the error analysis section of Appendix E.

The optimal stable operating pressure range

Fig.6.3 shows the data obtained from measuring the breakdown curve of the argon discharge with a fixed discharge gap and radius. The experimental curve demonstrates the general trend of breakdown curves in accordance with Paschen's law, namely that:

- At low pressures the electron mean free path is large; hence, the electron-neutral collision probability is low. Consequently, a higher voltage is required to generate enough electrons to initiate breakdown, resulting in a higher breakdown voltage V_b .
- At higher pressures the electron mean free path is shorter, resulting in more frequent electron-neutral collisions. The electrons do not gain sufficient energy, from the electric field, for the ionisation of gas atoms (or molecules) due to the prevalence of elastic collisions. Therefore, the breakdown voltage increases with increasing pressure.
- The curve displays a minimum value (or range of values) which corresponds to the minimum voltage at which electrical breakdown occurs ($V_{b,min}$).

According to Fig.6.3, the optimal breakdown voltage should occur between 2.0-4.0 Torr·cm, i.e. between 0.50 ± 0.05 Torr to 1.00 ± 0.10 Torr. When testing the discharge characteristics

in this pressure range it was found that in the 0.50-0.75 Torr pressure range the discharge did not remain stable (there were large fluctuations in current and voltage). Hence only pressures ranging from 0.80 ± 0.08 Torr to 1.0 ± 0.1 Torr were used for further investigations as the discharge seemed relatively stable within this range.

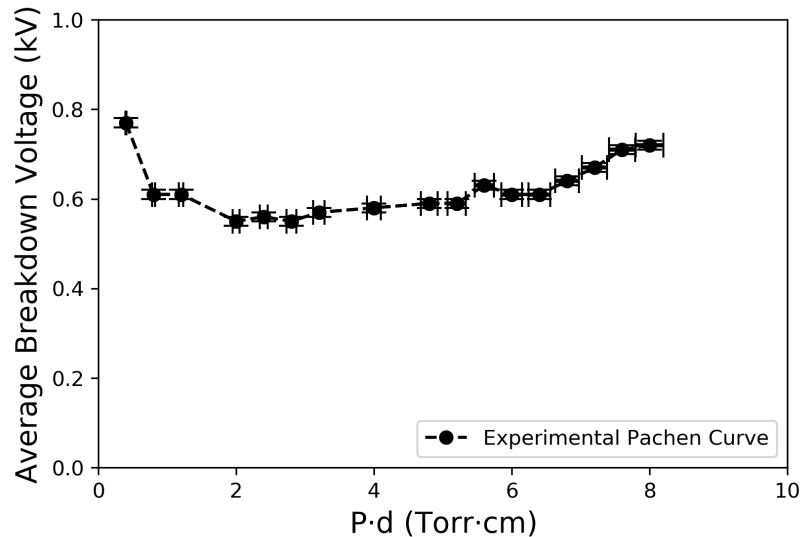


Fig. 6.3 Experimentally determined Paschen curve for argon discharge.

Closed discharge tube V-I characteristics

Fig.6.4 displays the results of the average measured discharge voltage, over 5 trials, as a function of changing current for a confined discharge (closed electrodes). At ~ 400 V, current began to flow as the gas reached the breakdown voltage. A dim purplish glow was observed through the gas flow opening. From that point onward the voltage-current relationship was strongly linear. This was expected as the discharge transitioned from the normal to abnormal glow region when the discharge current was in the milli-Ampere range, and according to the theory of glow discharges, the abnormal glow region is characterised by a slightly linear relationship between the current and voltage (see Fig.4.2). Visually, a violet/lavender discharge appeared to glow with greater intensity as the discharge current was increased. An increase in pressure causes the V-I curve to shift downwards (i.e. a higher discharge current is obtainable at a particular voltage with increasing pressure). This effect may be attributed to an increase in the number density of argon neutrals available for ionisation. However, the change becomes negligible between 0.85-0.95 Torr. The discharge appeared to be most stable and showed better repeatability in the 0.9-0.95 Torr pressure range.

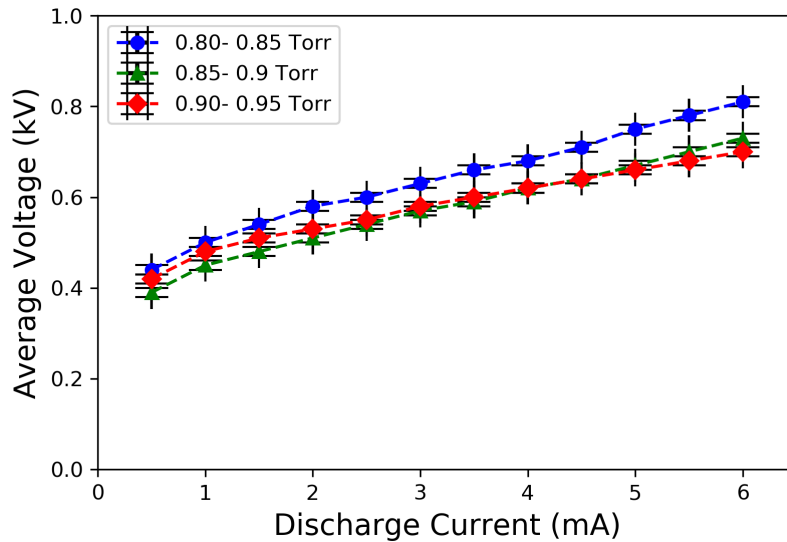


Fig. 6.4 Discharge voltage as a function of current in the pressure range 0.8-0.95 Torr.

V-I characteristics from the discharge with open electrodes

The next set of experiments involved the introduction of apertures at each of the electrodes. The apertures would allow for some of the current arriving at the electrodes to be ejected out of the thruster, generating the desired thrust. The discharge voltage was measured as a function of varying current for each of the four aperture sizes under investigation (i.e. 1 mm, 2 mm, 4 mm, and 8 mm). A total of four trials were conducted for each aperture size, to check for repeatability. The operating pressure was kept steady between 0.90 ± 0.09 Torr and 0.95 ± 0.10 Torr across all trials. The results of these experimental tests are presented in Fig.6.5 and Fig.6.6.

The results show a strong positive correlation (> 0.9) between the discharge current and voltage in all the aperture sizes explored. From Fig.(6.4), it was expected that an increase in aperture size, and subsequently a decrease in electrode surface area, would result in a higher voltage required to initiate and sustain the discharge due to the greater loss of charged particles to the ambient atmosphere. However, no observable relationship between the aperture size and the voltage-current characteristics of the discharge can be deduced from the data. The 2 mm and 8 mm apertures seem to display the most stable discharge characteristics with relatively good repeatability over the four trials conducted. Furthermore, the 2 mm and 8 mm aperture electrodes, along with the closed electrodes, exhibit almost identical electrical behaviour (see Fig.6.7 and Fig.6.8), with only a slight deviation occurring at higher currents (> 4 mA).

The V-I characteristics in the 1 mm and 4 mm aperture configurations were found to deviate significantly from that observed in the other configurations. Moreover, these aperture sizes exhibited unstable discharge behaviour with relatively large fluctuations in voltage-current characteristics across all four trials. The exact reasons for this abnormal behaviour are not known. As noted by [19], in gridded ion thrusters, careful attention needs to be afforded towards the sizing of the extractor apertures in the acceleration grid. In general the aperture diameter should not exceed the sheath width. This is to ensure that the quasi-neutral plasma does not penetrate through the apertures and subsequently lead to a loss in ion focusing power. According to the COMSOL simulation of the axial variation in plasma potential (see Fig.4.6), in this instance, the accelerator (cathode) sheath width is estimated to be between 2-2.5 mm. Thus, using an aperture diameter greater than 2.5 mm may have allowed the quasi-neutral plasma to penetrate through the aperture and caused the sheath potential surrounding the inner surface of the orifice to drop substantially. This could potentially explain the irregular voltage-current scaling, as a function of aperture diameter, observed in these experiments.

Alternatively, the underlying cause may be attributed to excessive sputtering of heavy ions on the cathode surface resulting in high erosion rates. The resulting erosion may have led to electrode surface deformation which in turn could have altered the electric field and thus the plasma characteristics of the discharge. The changes in the electric field properties would then have led to the large voltage fluctuations observed across subsequent trials. The high temperature plasma had also come into contact with the openings of the teflon endcaps when exiting the thruster. This had resulted in burning and discoloration of the endcaps and may have caused some carbon deposits to enter the tube and cause the observed sporadic behaviour.

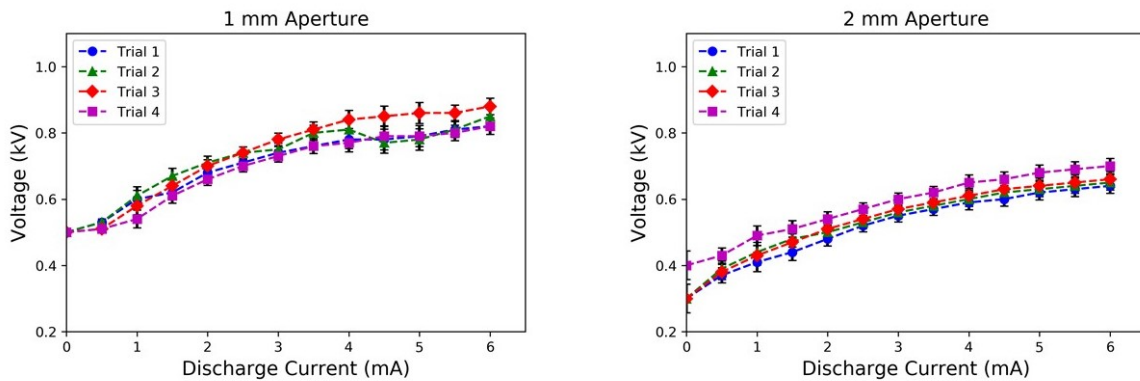


Fig. 6.5 V-I characteristics of the 1 mm and 2 mm aperture configurations.

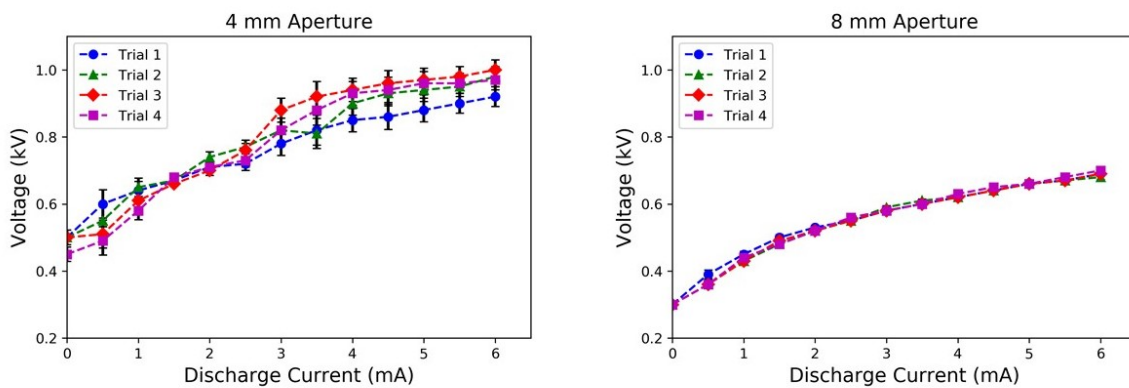


Fig. 6.6 V-I characteristics of the 4 mm and 8 mm aperture configurations.

Fig.6.7 and Fig.6.8 shows the clear discrepancy between the 1 mm and 4 mm aperture configurations relative to the 2 mm, 8 mm and closed electrode configurations. The almost identical behaviour exhibited by the 2 mm, 8 mm and closed electrode configurations provides some support for the hypothesis that the electrical characteristics of the system are independent of the aperture size. However, a more thorough investigation is required to conclude this with greater certainty.

The energy efficiency of the discharge plasma describes the total cost in energy of producing ions. It is a key metric used in the assessment of an electric thruster's overall performance. Fig.6.8 shows that the 2 mm and 8 mm apertures require the least amount of input power to produce a particular number of ions (discharge current). This indicates that the 2 mm and 8 mm aperture thruster configurations have the lowest ion production costs, relative to the other electrode geometries explored.

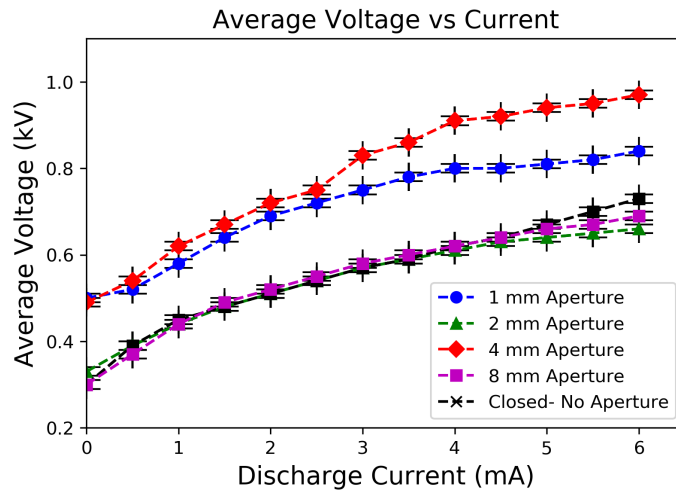


Fig. 6.7 Average voltage (over four trials) vs discharge current for various aperture sizes.

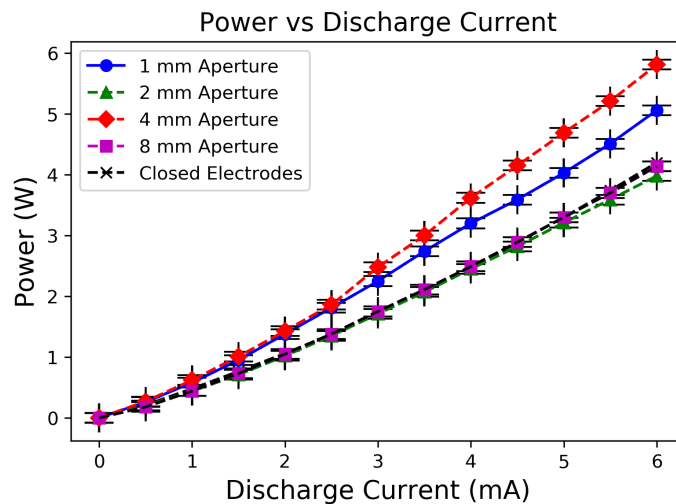


Fig. 6.8 Power vs discharge current for different aperture sizes.

Plume formation

Fig.6.9 show the plume formation for the 2 mm and 8 mm apertures from different angles. When the discharge current was < 1 mA, the discharge within the tube was dim and there was no noticeable plume formation at either electrode. At 1 mA the discharge became bright and a small plume began to form at the ground electrode opening. The plume size and intensity scaled with increases in discharge current.

In all cases, the beam emanating from the cathode opening was not tightly focused and

this is most probably an artefact of the charge exchange collisions occurring between the ejected ions and neutral background gas, as discussed in section 6.2. Furthermore, the average particle spread (beam emittance) was observed to increase with the increase in aperture size, in accordance with equation (6.3). Nevertheless, the existence of the ion plume is a strong indication that the ionisation-acceleration coupling mechanism works as intended.

It is worth mentioning here that, the space-charge limited current, introduced in equation (3.35), sets an upper bound on the ion current emission. Beyond this upper bound, the emitted ions within the plume could stall within their own space charge and would tend to repel back towards the cathode. This may result in neutralisation problems which could affect the thruster's operation. Even though ejected electrons, from the anode opening, may traverse around the thruster and neutralise the ion plume, it is also likely that the electrons could be re-accelerated into the thruster chamber resulting in a significant power drain. This needs to be investigated further.

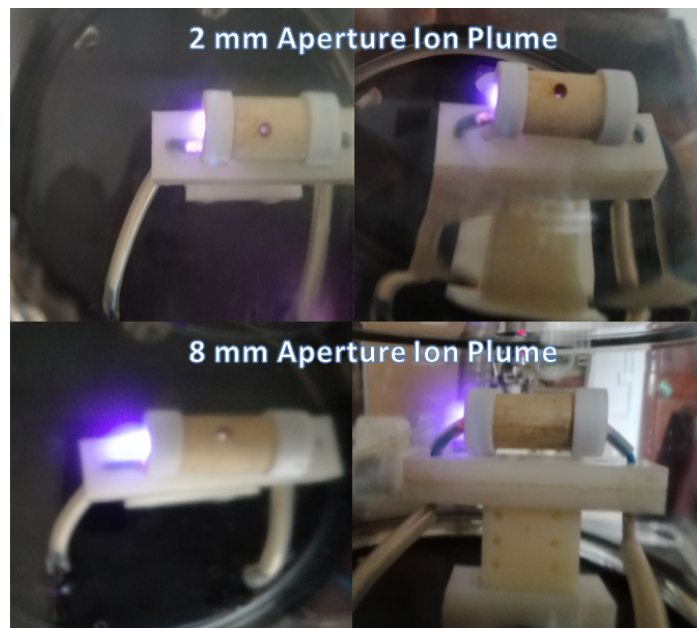


Fig. 6.9 Plume formation of 2 mm and 8 mm apertures at a discharge current of 6 mA.

Erosion and damage to the electrodes

Fig.6.10 and Fig.6.11 show images of the electrodes taken before and immediately after conducting the preliminary experiments. Each of the electrodes was exposed to the discharge plasma for roughly 2 hours in total. Upon completion of the preliminary studies, the electrodes were cleaned, with acetone, in an ultrasonic bath to remove the remaining adhesive

and any other unwanted dirt from its surface. Thereafter, the electrodes were placed under an optical microscope to assess the surface damage in more detail.

Erosion and damage to the electrodes are the major life-limiting factors that must be considered when developing new electric propulsion systems. Observations under the optical microscope revealed significant visual evidence of erosion and the formation of cathode spots in the 1 mm and 4 mm aperture cathodes (see Fig.6.12 and Fig.6.13). In contrast, these features were not visually discernible in the 2 mm and 8 mm aperture electrodes (see Fig 6.14). The release of energy from electronic or ionic bombardment on the cathode surface may be the primary cause of erosion and the observed cathode spots (more details on this can be found elsewhere, see [71]).

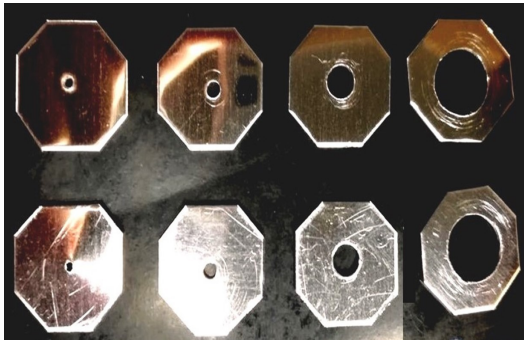


Fig. 6.10 Image of the electrodes taken before running the preliminary experiments. (1 mm, 2 mm, 4 mm and 8 mm aperture sizes).

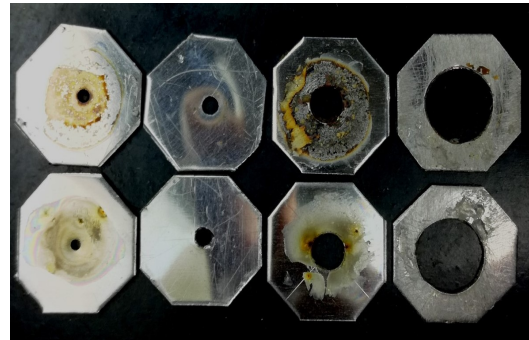


Fig. 6.11 Image of electrodes taken after conducting the preliminary experiments. Top: ground electrodes (cathodes), bottom: plasma electrodes (anodes).

The 8 mm aperture configuration did not show significant electrode damage or deformation. This was probably due to the 8 mm aperture having a smaller electrode area that was exposed to the discharge plasma and therefore exhibiting a lower sputtering probability. The 2 mm aperture configuration displayed anomalous behaviour as it did not exhibit any noticeable damage or erosion (apart from a slight discoloration observed at the cathode around the orifice) despite having a higher sputtering probability relative to the 4 mm aperture. These visual observations provide some support for the hypothesis that the irregular discharge behaviour exhibited by the 1 mm and 4 mm aperture configurations may have been due to sputtering and high electrode erosion rates.

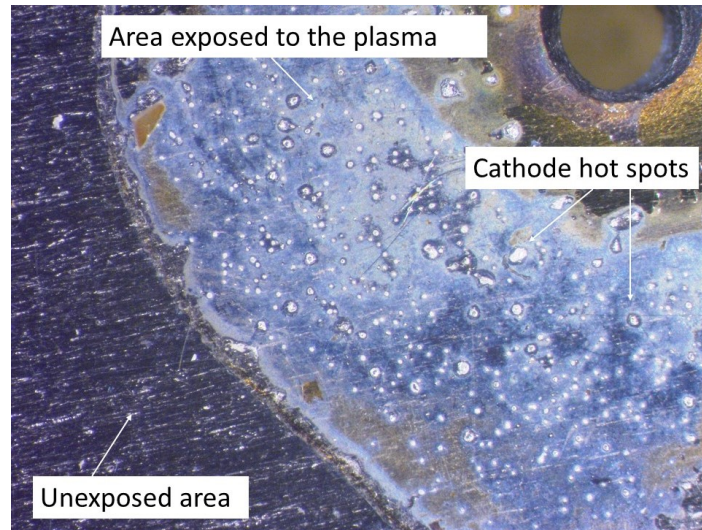


Fig. 6.12 Stereo microscopic image of the inner surface of the 1 mm aperture cathode after it was cleaned in an ultrasonic bath.

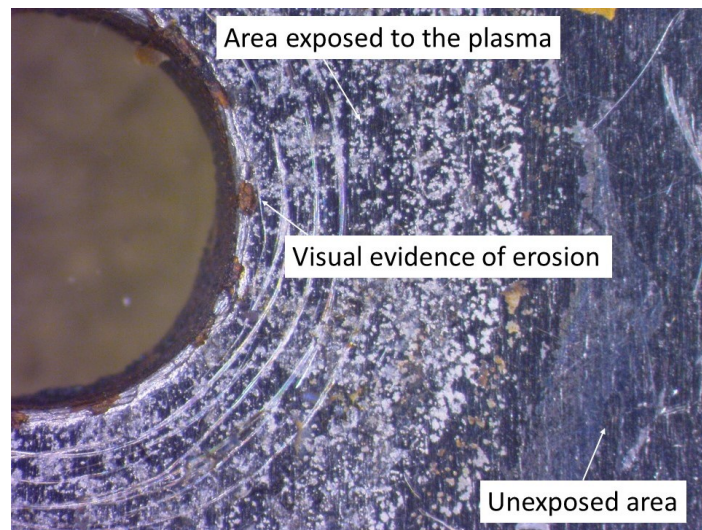


Fig. 6.13 Stereo microscopic image of the inner surface of the 4 mm aperture cathode after it was cleaned in an ultrasonic bath. The concentric rings are an artefact of the machining process.

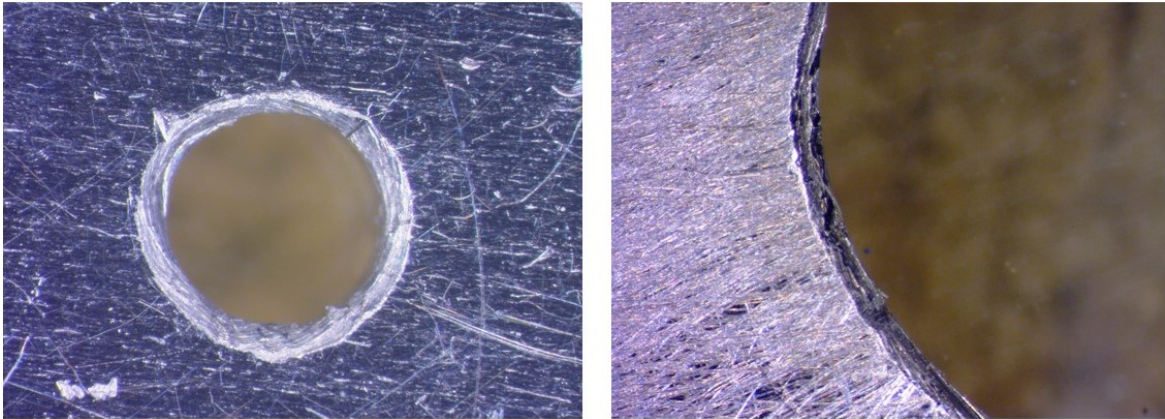


Fig. 6.14 Optical microscope image of the 2 mm (left) and 8 mm (right) aperture cathodes. The scratches on the surface are artefacts of the machining process.

6.7 Conclusions

Preliminary studies were conducted on the proof of concept thruster inside a glass vacuum chamber. The main goals of these studies were to confirm if the system worked as hypothesised, and to deduce the optimal parameters for its stable operation. Moreover, these preliminary studies served to identify any pitfalls or major drawbacks of the system in the hopes of mitigating any issues that may arise when studying the system in greater detail.

Results from the preliminary experiments found that, for a 40 mm long and 10 mm diameter thruster chamber, the optimal working gas pressure (across all aperture sizes explored) for stable discharge operation is between 0.90 ± 0.09 Torr and 0.95 ± 0.10 Torr. No observable relationship between the aperture size and the electrical characteristics of the system was found in these studies, although the near identical voltage-current behaviour observed in the 2 mm, 8 mm aperture and closed electrode configurations suggests that the system's electrical characteristics may not be dependent on the electrode aperture size. However, this requires a more detailed investigation. The most stable operation occurred when electrode apertures of 2 mm and 8 mm were used (as evidenced by the relatively smoother curves seen in Fig.6.7). Moreover, 2 mm and 8 mm apertures display the most favourable discharge characteristics, including relatively good repeatability, low ion production costs (high energy efficiencies) and very little erosion and damage when compared with the other aperture sizes investigated.

The cause of highly sporadic behaviour observed when using the 1 mm and 4 mm elec-

trode aperture configurations is inconclusive, however the irregular behaviour may be due to electrode erosion and surface deformation resulting from heavy ion sputtering at the cathode. Another plausible explanation for the fluctuations in V-I characteristics may be due to carbon deposits from the teflon endcaps entering the discharge plasma. This is likely since the endcaps (and the discharge tube) were reused across successive trials. To improve the validity of the results one would need to fabricate and assemble a new thruster for each trial conducted. However, due to time constraints and limited resources, this approach was not undertaken here. Lastly, increasing the electrode aperture diameter may have caused the quasi-neutral plasma to escape from the thruster and this may have impacted the sheath potential on the inner surface of the cathode. This could also be a reasonable explanation for the strange scaling results observed with an increasing aperture size.

The formation of plasma plumes at the open ends of the thruster indicates that charged particles are exiting the thruster and the ionisation-acceleration coupling mechanism appears to work as expected. Since the plume at the cathode end visually appears to be significantly larger than that at the anode, it is expected that the system should exhibit a net thrust in the direction opposite to the cathode plume, implying that the system works as hypothesised. However, it is noteworthy to mention that, the positive ions within the plume may stall in their own space charge and be reflected back into the thruster if not sufficiently neutralised by the ejected electrons. This could negatively impact the functioning of the system and needs to be investigated further.

Despite some unexpected results, the main goals of these preliminary studies were met. It must be noted, however, that the preliminary experiments may not have been conducted in the most suitable manner and this may have led to some of the anomalous behaviour observed. It will therefore be necessary to repeat these experiments with greater care in the future to obtain more accurate results. Some recommendations and improvements for future experiments include the following:

- Ensure that the electrodes, endcaps and thruster body are replaced with a new set after each successive trial.
- Use a higher temperature resistant insulation (like silicone) in place of the teflon endcaps on the outside of the electrodes. Ideally, the entire thruster should be built from the same ceramic material.

Considering the positive observations, the 2 mm aperture was taken to be the most optimal aperture size to be used for further studies. Even though the 8 mm aperture exhibited

favourable characteristics, this aperture diameter appears to exceed the cathode sheath width and thus may not be able to confine the quasi-neutral plasma effectively. As mentioned earlier, this could lead to issues with the thruster's operation. Using a 2 mm aperture also allows for the possibility to explore how changes in the aperture number (i.e. adding multiple apertures) would affect the operating parameters and whether the addition of multiple apertures would produce any emergent phenomena that may be desirable for a propulsion system.

Chapter 7

Ion Beam Current Measurements and Thrust Estimation

7.1 Introduction

After the completion of the preliminary studies, further testing on the 2 mm electrode aperture was conducted inside the larger stainless steel ring vacuum chamber. In these experiments the chamber was evacuated down to lower pressures using a water cooled diffusion pump, to better simulate the space environment. Unlike the preliminary studies, in these experiments the gas was directly fed into the thruster through a silicone tube securely fitted to the thruster opening via a nylon thread. This experimental setup provided a more accurate representation of an actual thruster that could be used on-board a spacecraft.

The following experiments were aimed at understanding what the effect of directly feeding the gas into the thruster would have on the discharge characteristics of the system and what influence the number of extraction apertures may have on the system's performance metrics (efficiency and thrust). As such, the discharge characteristics were measured as a function of changing aperture number. Another important goal of these experiments was to characterise the ion beam current emanating from the thruster and use the measurements to infer an estimate for the system's thrust. It is initially hypothesised that there exists a proportional relationship between the number of apertures and the V-I characteristics of the system as well as the extracted ion beam current, one would intuitively expect the beam current to increase proportionally with the addition of apertures. However, the results from the preliminary experiments seem to indicate that the system's behaviour is not trivial and hence such a

proportional relationship may not be observed. The following studies aim to clarify this matter.

7.2 Theory

Recall the diode extraction system presented in Fig.6.1. The electric field strength E between the plasma and ground electrode depends on the applied voltage V_a and the separation gap between the electrodes d , expressed as:

$$E = \frac{V_a}{d}. \quad (7.1)$$

The plasma meniscus (see Fig.7.1) is defined as the emission surface of the ions at the plasma boundary [72]. As the electrons move towards the plasma electrode, they are reflected at the meniscus if their energies are lower than the potential drop between the electrodes. The actual gap distance, denoted by d^* , is the distance from the plasma meniscus to the ground electrode. The magnitude of d^* changes to ensure that the electric field strength at the plasma meniscus is zero [11].

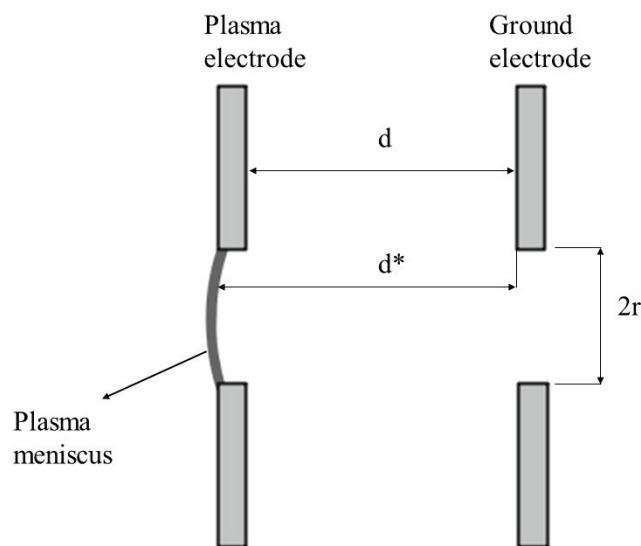


Fig. 7.1 Plasma meniscus formed in a diode extraction system.

Single aperture extraction systems

Consider Fig.7.2, which illustrates a cylindrically symmetric diode extraction system with a single extraction aperture of radius r and emission area $F = \pi r^2$. The total current that this system can extract is either limited by emission or space charge effects. In the case of the latter, the space charge limited current is the maximum transportable steady state current density through a one dimensional gap of distance d under an applied DC voltage [73].

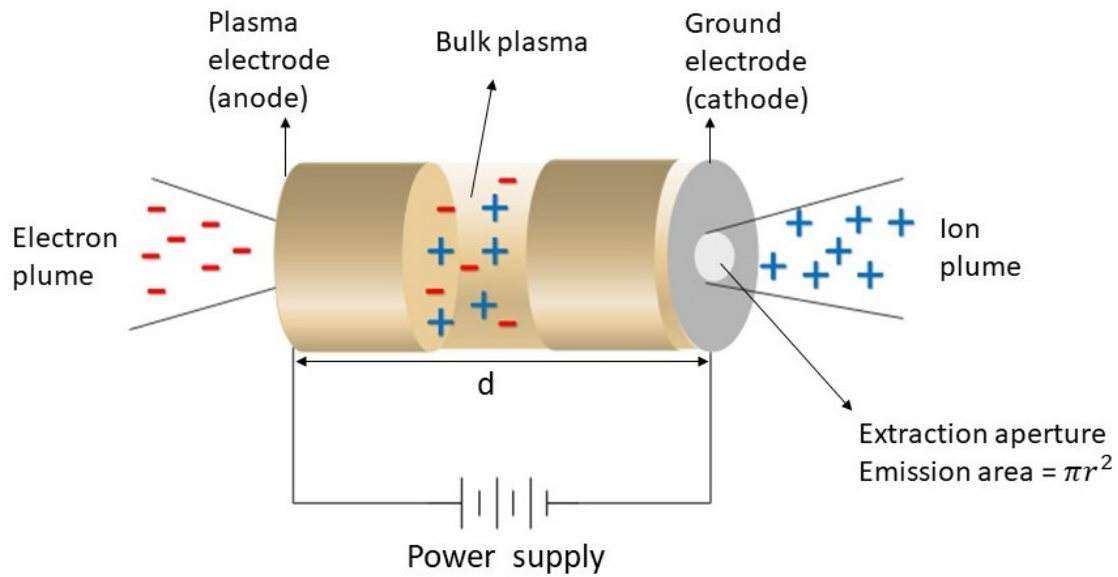


Fig. 7.2 A single aperture cylindrically symmetric ion beam extraction system.

Assuming that the ion beam current is space charge limited and that the emission area is planar and infinite, the ion current density J_i arriving at the ground electrode, with surface area A_c , can be determined from the Child-Langmuir law [74] and [75]:

$$J_i = \frac{I_i}{A_c} = \frac{4}{9} \epsilon_0 \sqrt{\frac{2e}{m_i}} \frac{V_a^{3/2}}{d^2}. \quad (7.2)$$

Here ϵ_0 represents vacuum permittivity, e is the electron charge and m_i is the ion mass. The Child-Langmuir law characterises the behaviour of the current density within a vacuum tube diode, i.e. it states that, for a fixed electrode gap distance (d), the current density arriving at the ground electrode is proportional to the acceleration voltage to the three-half power (i.e. $J_i \propto V_a^{3/2}$). Fig.7.3 provides a visual representation of this relationship.

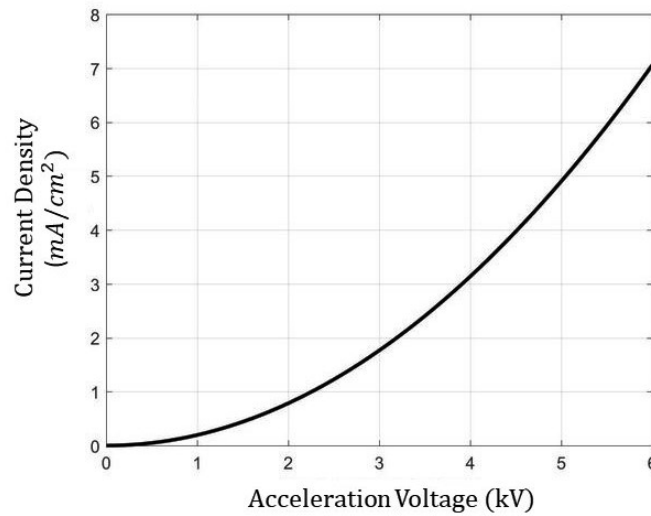


Fig. 7.3 Child-Langmuir law: typical current density vs acceleration voltage relationship in a diode tube.

The total extracted ion beam current, from a cylindrically-symmetric extraction system, can be calculated from equation (7.2) as follows [11]:

$$I_b = \frac{4}{9} \pi \epsilon_0 \sqrt{\frac{2e}{m_i}} S^2 V_a^{3/2}. \quad (7.3)$$

The aspect ratio S is defined as the ratio of the aperture radius to the discharge gap (i.e. $S = r/d$). For a fixed aspect ratio, the extractable ion beam current will be proportional to the acceleration voltage to the three half power. The remaining constant of proportionality is called the perveance P of the extraction system [11]:

$$P = \frac{4}{9} \pi \epsilon_0 \sqrt{\frac{2e}{m_i}} S^2. \quad (7.4)$$

Beam divergence

The ion current density in equation (7.2) is influenced by the plasma density N at the meniscus [11]. Fig 7.4 shows how different plasma densities at the meniscus affects the emission area. At a very low density (N_1) the actual gap distance d^* increases and the resulting emission area is concave shaped. In contrast, if the plasma density is very high (N_3) then d^* decreases and the emission area tends to be planar or convex shaped. If the plasma density is optimised (N_2) then the extracted ion beam should exhibit a minimum divergence angle when exiting through the aperture.

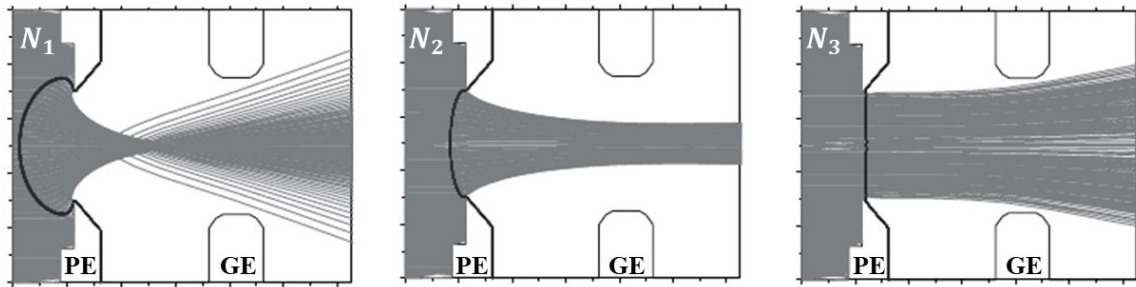


Fig. 7.4 AXCEL-INP simulation of an ion extraction system with three different plasma densities and a fixed potential drop across the electrodes. PE = Plasma electrode, GE = Ground electrode and $N_1 < N_2 < N_3$. Image taken from [11], p.63.

Since the extracted ion beam current largely dictates the magnitude of thrust generated, it is desirable to have the ions extracted into a focused beam with a minimum divergence angle to minimise thrust loss and decrease plume interaction with the other components of the spacecraft. The extracted ion beam satisfies the matched case when more than 80% of the ion beam current is contained within a divergence angle less than ± 20 mrad [11]. The two main factors which prevent the extraction of a focused ion beam are:

1. The ion temperature
2. The thickness and shape of the plasma electrode

In addition to this, it is important to minimise aberrations in the extraction system as this may also contribute to a greater beam divergence.

Maximising the extracted ion current

An important question arises as to what the total extracted ion beam current would be if the aperture radius were to stay fixed while the aperture number, and subsequently the total emission area, were to increase. The experiments to follow will attempt to characterise the relationship between the number of apertures and the total extracted ion beam current.

Thrust estimation

The magnitude of the extracted ion current greatly influences the overall thrust of the system. The net thrust T generated by the system can be deduced from the acceleration voltage and the ion current in the extracted beam as follows [19]:

$$T = \gamma \sqrt{\frac{2m_i V_a}{e}} I_b, \quad (7.5)$$

where γ represents the total thrust correction factor, which accounts for the presence of multiply charged ions within the beam, along with thrust dissipation due to beam divergence [19]. It can be defined mathematically as:

$$\gamma = \alpha_M F_t. \quad (7.6)$$

Here, α_M is characterised by the ratio of multiply charged ions to singly charged ions and accounts for the fact that multiply charged species carries multiple charges but only a single unit of mass. According to Hocart [76], electron ionisation is rarely capable of producing a large abundance of multiply charged ions. This is verified by the authors of [19] (see p.24) who state that multiply charged ions occur in relatively small quantities within the extracted ion beam in electric thrusters. Hence, α can be taken as unity to a good approximation.

The second term, F_t , represents the thrust correction due to beam divergence. If the beam is accelerated by a uniform electric field that exhibits a constant ion current density profile, then the thrust correction can be expressed as:

$$F_t = \cos \theta, \quad (7.7)$$

where θ is the half angle divergence of the beam. For $\theta < 15^\circ$, $F_t = \cos \theta \approx 1$. Hence, for a small θ the thrust dissipation due to beam divergence is negligible. Therefore, if these conditions are met, equation (7.5) can be approximated as:

$$T \sim \sqrt{\frac{2m_i V_a}{e}} I_b. \quad (7.8)$$

Since the system's thrust is proportional to the magnitude of the ion beam current, the ion beam current should be maximised to increase the thrust. This can be accomplished by introducing additional apertures to the extractor electrode. However, the addition of apertures may impact the ion production efficiency of the system as explained below.

Thruster efficiency

Electric thrusters in general are geared more towards efficiency rather than greater thrust production. It is therefore important to identify a thruster's efficiency when assessing it's

overall feasibility. In this regard, the ion production efficiency and the electrical efficiency are important metrics. One can also infer the total thruster efficiency from the ratio of thrust generated per unit of input power.

Ion production efficiency

The ion production efficiency, also referred to as the discharge loss η_d , characterises the energy cost of producing a certain number of ions. It is mathematically expressed as the ratio of the discharge power to the magnitude of ion beam current:

$$\eta_d = \frac{P_d}{I_b} = \frac{I_d V_a}{I_b}, \quad (7.9)$$

where I_d was previously defined as the discharge current. The discharge loss is frequently expressed in units of Watts per Ampere (W/A). Since η_d represents a power loss it is desirable to have it as low as possible.

Electrical efficiency

The thruster's electrical efficiency, denoted as η_e , can be deduced from the fraction of the output beam power P_b and the total input power P_T as:

$$\eta_e = \frac{P_b}{P_T} = \frac{I_b V_a}{I_b V_a + P_d}. \quad (7.10)$$

The effect of increasing the number of apertures on the thrust, the ion production efficiency and the electrical efficiency of the thruster will be investigated in the experiments that follow.

7.3 Aims

- To investigate the effect of changing aperture number on the electrical behaviour of the thruster.
- To determine the ideal propellant mass flow rate for optimal ion beam extraction.
- To investigate the effect of changing aperture number on the magnitude of extracted ion beam current.
- To infer an estimate of the system's overall thrust based on the ion beam current measurements.

- To deduce a relationship between the aperture number, net thrust and the efficiency of the thruster

7.4 Apparatus

- Stainless steel ring vacuum chamber
- Hivolt T1EP high voltage power supply
- High voltage cable
- Alcatel roughing pump
- Leybold-Haraeus water cooled diffusion pump
- High vacuum Penning gauge
- Afrox Argon gas (propellant) Baseline 5.0
- Mass flow measurement system
- Arduino microcontroller and INA219 current sensor
- DS5022 oscilloscope

7.5 Methodology

Experimental Setup

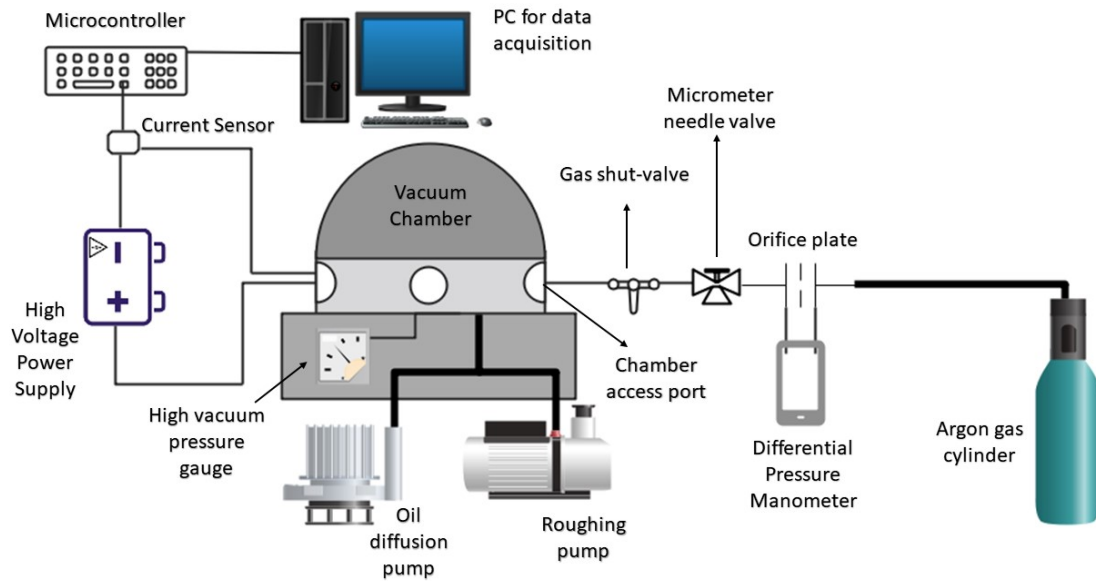


Fig. 7.5 Experimental setup used to measure the influence of changing aperture size/number on the discharge characteristics of the thruster.

Fig.7.5 shows the general experimental setup used to measure the relationship between changing electrode aperture configuration and the electrical behaviour of the thruster. A 760 mm diameter x 200 mm high stainless steel ring vacuum chamber, fitted with multiple access ports, was used to simulate the ambient space environment. The chamber was pumped down to $5 \pm 1 \times 10^{-5}$ Torr with the aid of a roughing pump and an oil diffusion pump. The high vacuum Penning gauge was used to monitor the pressure within the chamber. The propellant gas was directly fed into the thruster through a silicone tube securely connected to the thruster opening via a nylon thread.

Fig.7.6 shows the modified thruster stand setup used in the larger chamber. In this setup, the HV cables were securely connected to the electrode through pressure contacts. An in-house developed mass flow measurement system (see Fig.7.7), based on the orifice plate concept, was used to measure the mass flow rate of the propellant gas into the thruster (refer to Appendix C for more details on the calibration process). The discharge current arriving at the cathode was measured using an Adafruit INA219 current sensor connected to an Arduino

microcontroller. The data was then sent to a PC and recorded using CoolTerm serial port terminal software.

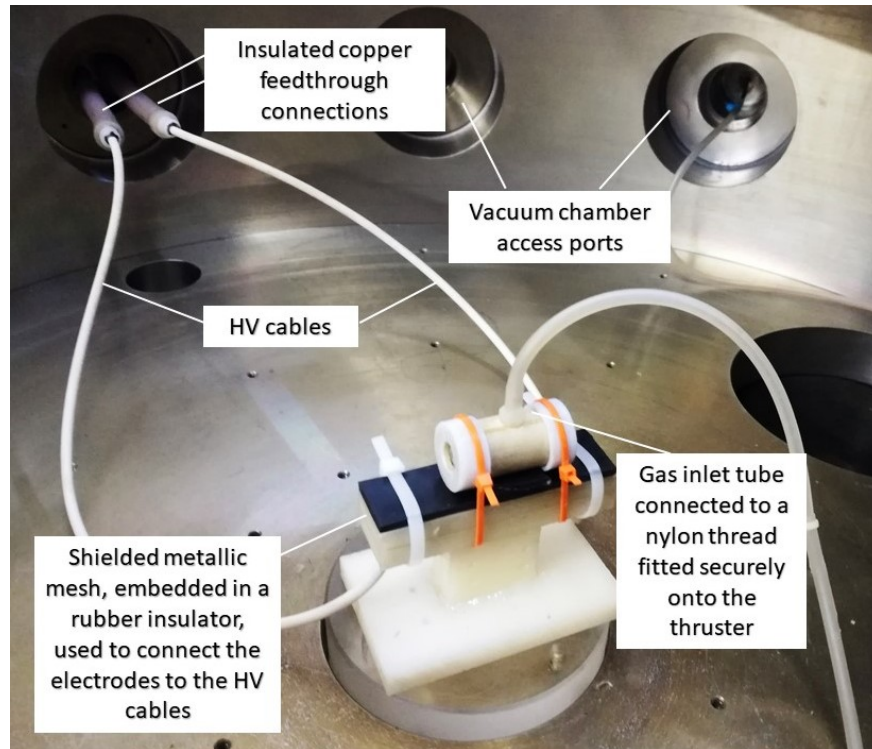


Fig. 7.6 The setup used inside the vacuum chamber. The thruster stand was modified for easier and more secure attachment of the electrodes to the HV cables through the use of pressure contacts. Note that the teflon endcaps were eventually removed and replaced with a silicone shielding.

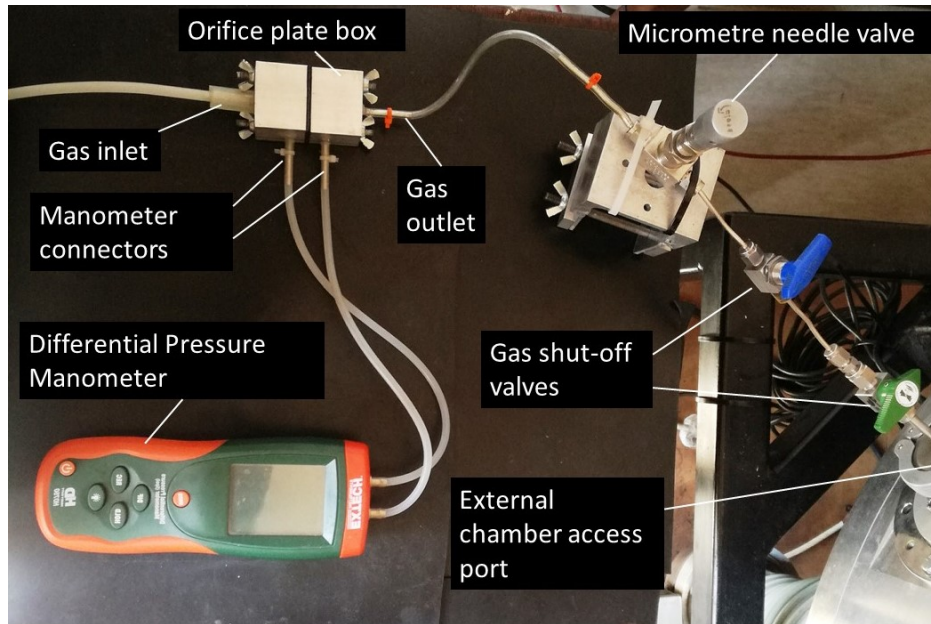


Fig. 7.7 The mass flow rate measurement system setup including the in-house developed orifice plate box.

7.5.1 Measuring the influence of changes in electrode aperture configuration on the discharge characteristics of the system

Once the chamber had been evacuated, the gas flow was activated and the mass flow rate was adjusted using the micrometer needle valve. Mass flows as low as 100 ± 2 ng/s were accurately measured using the procedure highlighted in Appendix C. In these experiments the mass flow rate was kept fixed at 180 ± 4 ng/s. The HV power supply was then switched on and the output current was set to maximum. The output voltage was slowly adjusted using the voltage dial on the front panel. The voltage was increased in increments of 0.50 ± 0.01 kV. At each voltage increment the discharge current was measured using the current sensor. The current was measured every second for a total of 60 seconds. After which the serial port was disconnected, the voltage was increased to the next increment and the serial port was reconnected to take current measurements at the new voltage setting. The procedure was repeated five times for each of the electrode aperture configurations investigated. The average current over the 60 second measurement interval was calculated and used to produce the V-I characteristics in each case.

7.5.2 Characterising the extracted ion beam current as a function of changing electrode configuration

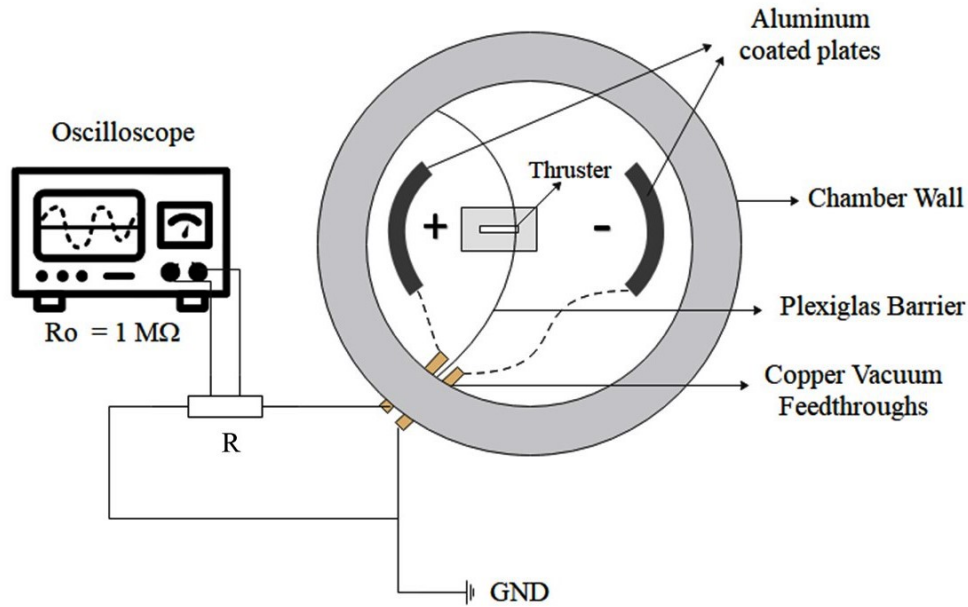


Fig. 7.8 The experimental setup used to measure the extracted ion beam current.

The second part of the experiment involved measuring the ion beam current emanating from the thruster. In this regard, two aluminum collector plates were used to measure the extracted ion beam current. The plates were positioned 90 ± 10 mm and 180 ± 10 mm from the cathode and anode respectively and were separated by an insulating plexiglas barrier. The barrier was put in place to mitigate charge transfer between the plates, which would have led to inaccuracies in the measured beam current. The plate at the anode end was connected directly to ground, while the ion beam collecting plate was connected to a resistor, of resistance R , and then to ground. An oscilloscope was used to measure the voltage drop V_R across the resistor. The oscilloscope itself added a parallel resistance $R_0 = 1$ MΩ to the circuit which had to be accounted for. Thus, the true resistance was taken as:

$$R_{true} = \frac{R_0 R}{R_0 + R}. \quad (7.11)$$

Subsequently, the ion beam current was calculated from Ohm's law as follows:

$$I_b = \frac{V_R}{R_{true}}. \quad (7.12)$$

Note that in this setup the measured voltage drop can be adjusted by changing the resistance. Thus, a wide range of ion currents can be measured. In these experiments, three different resistors, ranging from $0.82 \pm 0.01 \text{ M}\Omega$, $1.64 \pm 0.01 \text{ M}\Omega$ and $2.45 \pm 0.01 \text{ M}\Omega$, were utilised. In each instance, the oscilloscope measured the average voltage drop over 60 seconds. Multiple trials were conducted for averaging and to check for repeatability.

7.6 Results and Discussion

The results obtained from the the experiments mentioned above are presented below. A detailed error analysis, including the origin of the uncertainties in measured quantities and the calculation of error bars can be found in the error analysis section in Appendix E.

The initial intention had been to study the system's electrical behaviour using a an $n \times 2$ mm aperture configuration (where $n = 1, 2, 4, 5, 7$). To accommodate for the addition of a large number of apertures, the thruster's dimensions were increased to $L = 52$ mm and $R = 13$ mm (refer to Fig.7.9). Note that even though the dimensions had changed, the ratio L/R was kept the same as that from the preliminary tests.

In practice, given the limited output power of the supply, the discharge did not initiate, even at the maximum applied voltage of 10 kV, when more than 4×2 mm apertures were used. This may potentially be due to the fact that the multi-aperture configurations could not confine the gas within the thruster long enough for electrical breakdown to occur. The gas likely diffused from the thruster into the ambient atmosphere within the chamber through the multiple orifices. Attempts to remedy the problem involved reducing the discharge gap between the electrodes, as this was expected to drop the minimum breakdown voltage, along with increasing the propellant flow rate. Although the discharge had initiated in some of these cases, the system failed to operate in a stable manner. After numerous failed attempts, further studies of the $n \times 2$ mm aperture (where $n > 4$) systems had been abandoned. Therefore, the results presented henceforth only show the V-I characteristics of $n \times 2$ mm aperture configurations where $n = 1, 2$ and 4 respectively.

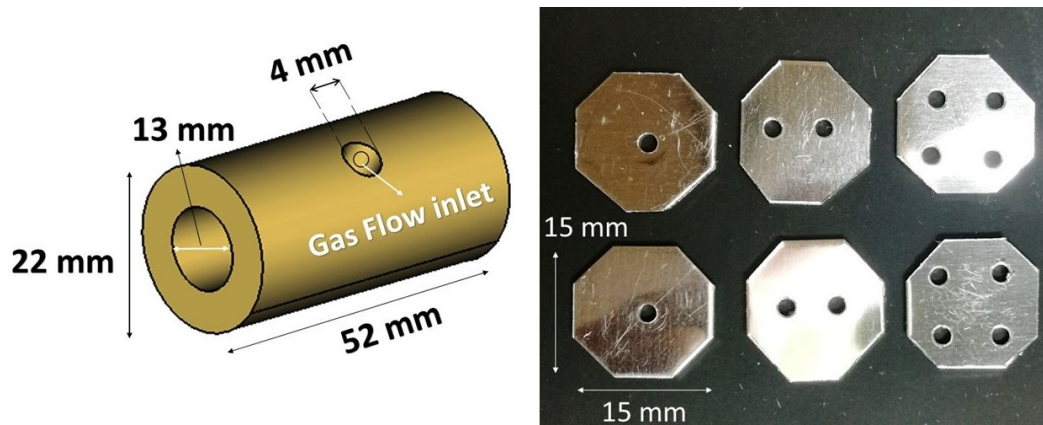


Fig. 7.9 Modified thruster tube geometry and the different electrode aperture configurations used in the experimental tests.

7.6.1 Voltage-current characteristics as a function of changing electrode aperture number and propellant flow rate

Fig.7.10 and Fig.7.11 shows the thruster's voltage-current behaviour for changing aperture number at a constant propellant flow rate of 180 ± 4 ng/s. Although all configurations showed good repeatability, the 1x2 mm configuration displayed relatively better repeatability over all five trials conducted. The authors of [77] had measured the V-I characteristics of a DC plasma discharge with a similar inter-electrode gap. The V-I characteristics observed in Fig.7.10 and Fig.7.11 follow the same general behaviour as those presented in [77]. The observed non-linear behaviour between the discharge current and applied voltage is a characteristic of the abnormal glow region (see Fig.4.2). In this region of the glow discharge, the electrodes are completely covered by the plasma and thus the cathode fall increases with increasing discharge current in accordance with the space charge limited form of the Child-Langmuir equation (i.e. $I \propto \frac{V^{3/2}}{d^2}$).

The breakdown voltage tended to increase when more apertures were added. The additional orifices had reduced the total surface area of the electrodes thereby decreasing the number of primary electrons from photoemission. Moreover, the reduced electrode surface area may have resulted in a lower secondary electron emission yield and thus a higher supply voltage was required to both initiate and sustain the discharge. Although the propellant flow rate had been kept constant, the actual pressure within the tube may have been significantly influenced by the addition of apertures. This change in pressure may have also contributed to the observed shift in breakdown voltage. The plot on the right of Fig.7.11 shows the average discharge current, over 5 trials, as a function of applied voltage and changing aperture number.

The V-I characteristics for closed electrodes was also measured, at the same propellant flow rate, and plotted for comparison. A downward shift in the V-I curves was observed when the number of apertures were increased. The addition of apertures resulted in lower discharge current at higher applied voltages (as measured between the electrodes), however, this is to be expected as a larger fraction of the discharge plasma had been ejected out of the thruster into the ion beam when additional apertures had been employed. The greater loss of charged particles would have resulted in the need for a higher applied voltage to sustain the discharge explaining the observed behaviour.

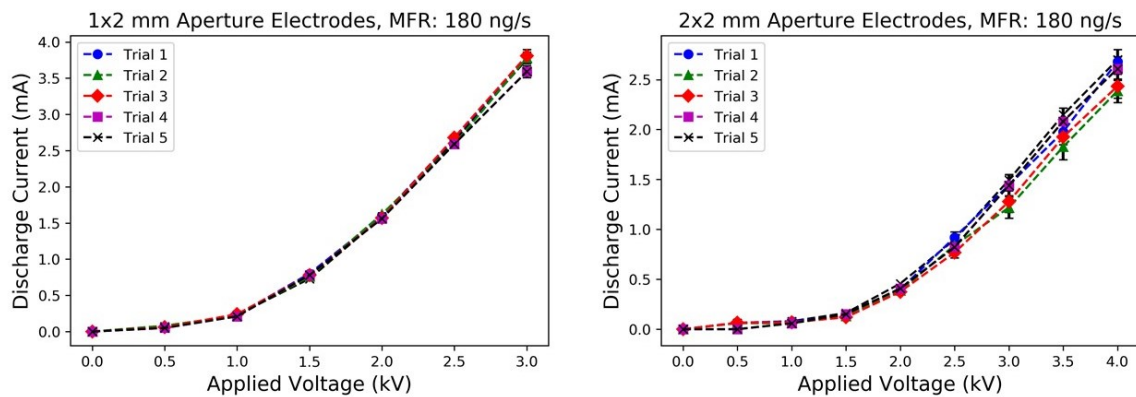


Fig. 7.10 Thruster V-I characteristics with a 1x2 mm and 2x2 mm aperture electrodes.

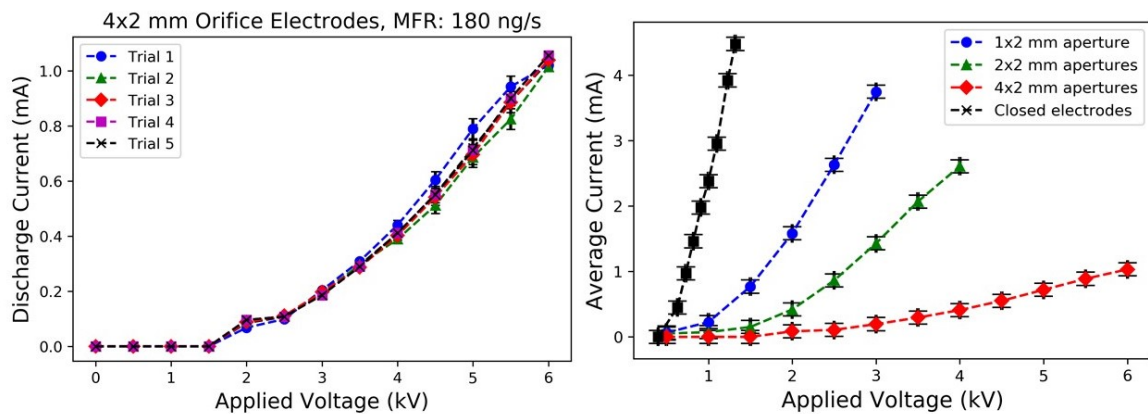


Fig. 7.11 Left: Thruster V-I characteristics with 4x2 mm aperture electrodes. Right: Average discharge current (over 5 trials) as a function of applied voltage and changing electrode aperture number.

Fig.7.12 displays the effect of increases in the propellant flow rate on the V-I characteristics of the system. It was found that at a higher flow rate of 300 ± 10 ng/s the the

breakdown voltage, for the same aperture number, had decreased since the increase in neutral argon number density within the discharge vessel resulted in a greater ionisation rate. This is because the electron mean free path λ_e decreases with the increase in neutral gas density, see equation (3.25). In essence, for a fixed aperture number, the voltage current curve tends to shift upwards at higher propellant flow rates, i.e. a particular discharge current is obtainable at a lower applied voltage when the flow rate is increased. This is only the case if the gas pressure between the electrodes remains below the optimal pressure range, where the minimum breakdown voltage is achieved, according to Paschen's law. It must be noted that the system begins to behave in an unstable manner when the propellant flow rate is set too high (> 300 ng/s in this case). This unstable behaviour may be attributed to the large number of elastic collisions, which may occur when the electron mean free path is significantly reduced. In this instance, an intense plasma plume, most probably consisting of electrons, forms at the anode opening and grows in intensity as the propellant flow rate is increased further (see Fig.7.13).

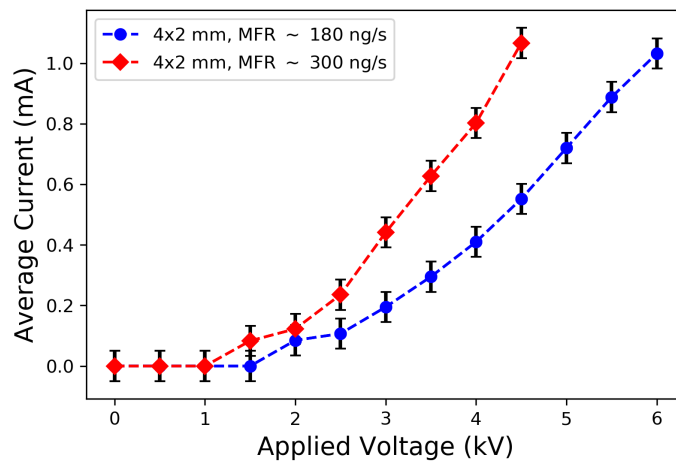


Fig. 7.12 V-I characteristics for the 4x2 mm aperture system at different propellant flow rates.



Fig. 7.13 Plume formation observed at the anode when the propellant flow rate was set above 300 ng/s. The thruster did not operate stably when the propellant flow rate was set higher than this. Despite its dramatic appearance, it is hypothesised that this plume consists predominately of electrons which do not contribute significantly to thrust.

In each of the configurations investigated, the discharge was observed to be stable up to a particular voltage. Further increases in voltage beyond this operating point led to unstable and sporadic thruster behaviour. The 1x2 mm configuration displayed stability at higher discharge currents in comparison to the other configurations. When the thruster was fired in the stable operating range, a continuous focused ion beam was observed at the cathode opening in all of the configurations explored. A bright plume emanated spontaneously, and lasted for less than a second, from the live electrode at irregular intervals. This however did not significantly impact the discharge behaviour.

The ion beam emanating from the thruster visually appeared to be of higher intensity when multiple orifices were used. This suggests that a significant amount of ion current was leaving the thruster, which would have resulted in an increased thrust, since the thrust that the system produces is proportional to the ejected ion beam current.

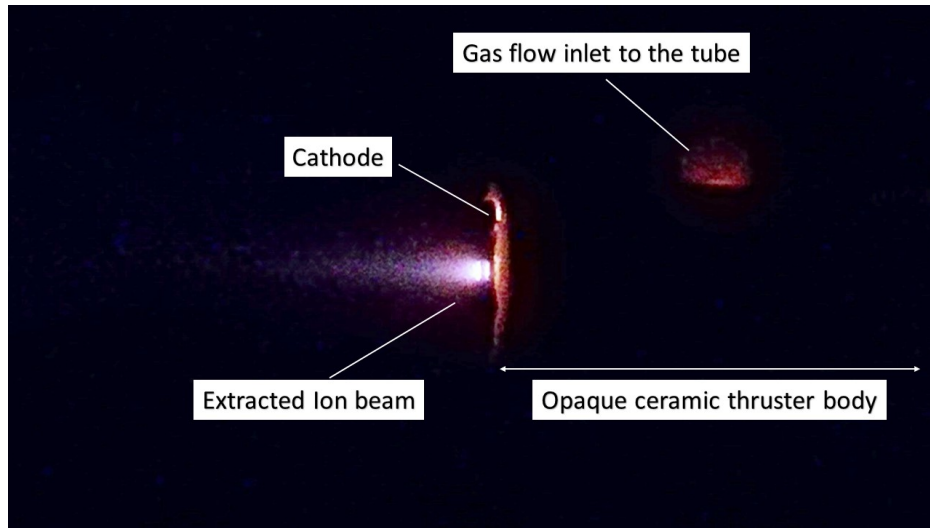


Fig. 7.14 Image taken from the vacuum chamber viewing port of the extracted ion beam generated at the 2x2 mm aperture cathode.

7.6.2 Measuring the ion beam current as a function of applied voltage and discharge current

Fig.7.15 shows the measured ion beam current, for a 1x2 mm electrode aperture configuration, as a function of applied voltage and discharge current measured at the cathode. The propellant flow rate was kept steady between $180\text{-}200 \pm 6$ ng/s in all cases. Increasing the applied/acceleration voltage between the two electrodes results in an increase in the discharge current and subsequently translates to a higher ion current density within the extracted beam.

Moreover, increasing the resistance results in a higher measured ion beam current at a particular voltage or discharge current. This effect can be attributed to the greater impedance of the resistor, which prevents electrons from flowing through the circuit and neutralising the positive charge on the collector plate. Since the electron temperature exceeds the ion temperature, the electrons are expected to leave the plasma at a faster rate than the ions. Consequently, a net positive charge build-up occurs within the bulk plasma. The resulting positive potential then sets up a retarding electric field which slows down the electrons and confines them within the plasma. In this way, the quasi-neutrality condition is satisfied (see section 3.3). The quasi-neutrality condition also implies that the ejected ion and electron current will be approximately the same. Hence, for every ion ejected at the cathode aperture, an electron is ejected at the anode aperture. The ions and electrons then impact their respective collector plates and subsequently the plates become positively/negatively charged. The

electrons from the negatively charged plate flow through the circuit towards the positively charged plate to neutralise the positive charge. The resistor impedes the flow of electrons to the plate. A greater resistance results in a greater impedance and thus a higher measured voltage drop across the resistor. Consequently, this leads to a higher measured ion beam current, in accordance with equation (7.12).

The authors of [78] had conducted ion beam current measurements from a cold conical cathode ion source using a copper collector plate and cathode exit aperture of 7 mm. The relationship between the ion beam current and discharge voltage observed, in Fig.7.15, when using a $2.45 \pm 0.01 \text{ M}\Omega$ resistor is in agreement with that presented in [78], which provides some support for the validity of these results. However, the ion beam currents measured in [78] are an order of magnitude larger potentially, due to the use of a larger cathode exit aperture.

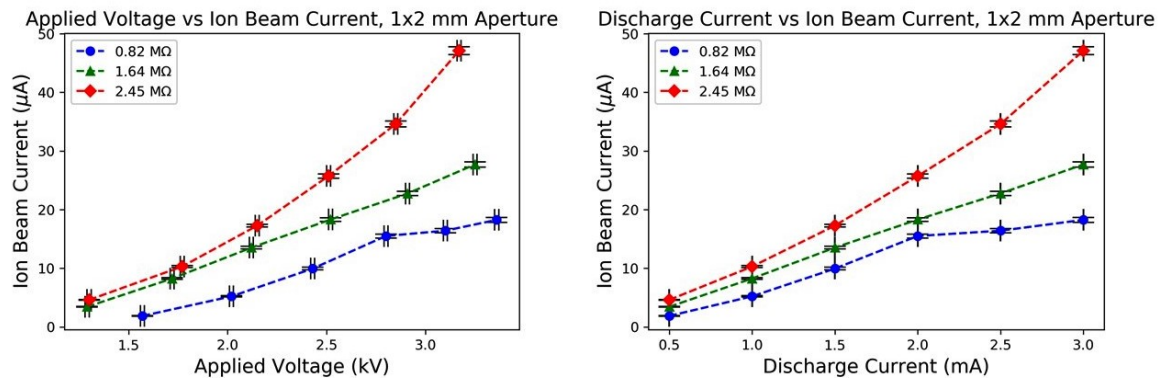


Fig. 7.15 Measured ion beam current, calculated from the voltage drop across a 0.82, 1.64 and $2.45 \pm 0.01 \text{ M}\Omega$ resistor, as a function of applied voltage and discharge current across the plasma source. Note that the parallel resistance of the oscilloscope has been taken into account when calculating the beam current, see equation (7.11).

Ion beam current and estimated thrust as a function of changing aperture number

The measured extracted ion beam current, for a single, double and quadruple 2 mm aperture electrode configuration is shown in Fig.7.16. Measurements were made using three different resistors. In each case, the discharge current was kept fixed at $1.000 \pm 0.001 \text{ mA}$ for comparison. The value of 1 mA discharge current was chosen as it was observed to be a common stable operating point in all configurations. As expected, increasing the resistance results in a higher measured beam current. Ion beam currents on the order of tens to hundreds of

micro-Amperes were measured when a $2.45 \pm 0.01 \text{ M}\Omega$ resistor was employed.

The results show that for a fixed aperture diameter of 2 mm and a discharge current of $1.000 \pm 0.001 \text{ mA}$, increasing the number of apertures increases the total extracted ion beam current as expected. The measured ion beam current ranges from $5.21 \pm 0.11 \mu\text{A}$ to $10.29 \pm 0.15 \mu\text{A}$, for each of the resistors, when a single aperture is used. The addition of a second 2 mm aperture causes the ion beam current, for each aperture configuration, to increase by ~ 10 fold. Thereafter, the measured beam current appears to plateau with the addition of subsequent apertures. The underlying reason for the plateau is not well understood and goes against the hypothesis of a linear increase in beam current with increasing aperture number. Secondary electrons resulting from ion bombardment at the collector plate may be recombining with the ions, as they move towards the positively charged ion beam, thus reducing the total current arriving at the plate, which could be an explanation for the observed plateau. This effect can be mitigated by using a Faraday cup, which suppresses secondary electron emission, instead of a metallic collector plate. However, this will likely decrease the resolution of the current measurement.

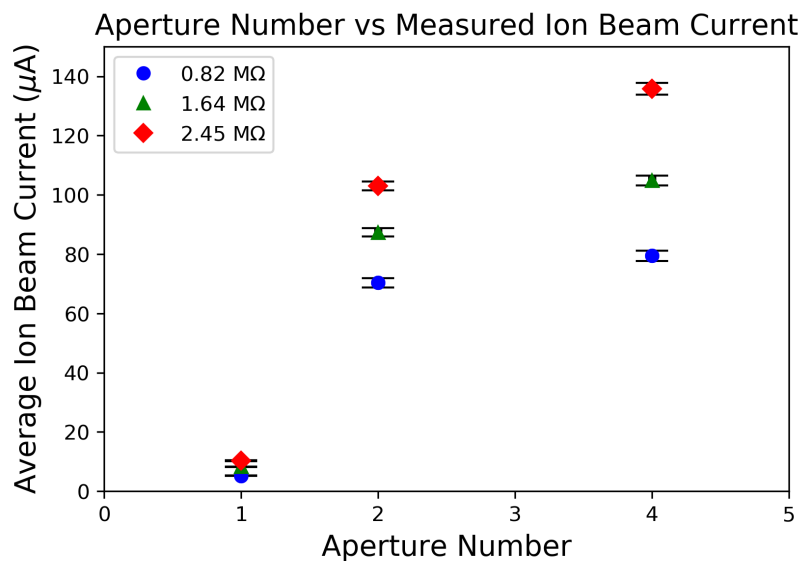


Fig. 7.16 Measured ion beam current (obtained using a $2.45 \pm 0.01 \text{ M}\Omega$ resistor) as a function of aperture number. The discharge current was kept fixed at $1.000 \pm 0.001 \text{ mA}$ and the MFR was set to $180\text{-}200 \pm 6 \text{ ng/s}$.

The measured ion beam current for each system configuration, in conjunction with the corresponding acceleration voltage, can be used to obtain estimates for the system's thrust.

Table.7.1 presents the estimated thrust, calculated using equation (7.8), for single, double and quadruple apertures.

Table 7.1 The relationship between the number of apertures, the average ion acceleration voltage, the measured ion beam current (from the $2.45 \pm 0.01 \text{ M}\Omega$ resistor) and the estimated thrust for a fixed aperture radius of 2 mm. The discharge current was kept constant at $1.000 \pm 0.001 \text{ mA}$ across all aperture configurations.

Aperture No.	V_a (V)	δV_a (V)	I_b (μA)	δI_b (μA)	T (μN)	δT (μN)
1	1765	± 10	10.29	± 0.15	0.13	± 0.02
2	2340	± 10	102.98	± 1.45	1.43	± 0.12
4	3435	± 10	135.79	± 1.91	2.29	± 0.13

The required acceleration voltage to obtain a discharge current of 1 mA had increased with an increase in the aperture number. This was expected since increasing the number of apertures resulted in a greater loss of neutral propellant and charged particles from the discharge chamber. Subsequently, a higher voltage is required to initiate and sustain the discharge.

The thrust is estimated to be less than one micro-Newton when a single aperture is used and increases rapidly with the addition of a second aperture, resulting from the 10 fold increase in beam current, but exhibits a diminishing return with the addition of subsequent apertures. One may naively expect the "thrust" to increase linearly with the number of apertures, but the system is likely much more complex. These early results seem to indicate that the apertures "interact" non-trivially with each other. The experiments need to be repeated more carefully with a more sophisticated setup. Moreover, it is recommended that a much larger sample size of apertures be studied, with aperture numbers ranging from 1 to > 20 , in order to make a pattern more apparent. This will most likely require a power supply with an output voltage greater than 10 kV and an output current greater than what is currently available in the laboratory where the experiments were conducted.

Comparisons with theoretical predictions

Table 7.2 shows a comparison between the theoretical ion beam current and the measured ion beam current, at the given acceleration voltages, when a $2.45 \pm 0.01 \text{ M}\Omega$ resistor was used. The values of I_b^{Theo} were obtained using equation (7.3) under the assumption that the beam current would increase linearly with the number of apertures, i.e. assuming that $I_n = n \times I_1$, where n denotes the number of apertures.

Table 7.2 Comparison between the theoretical ion beam current I_b^{Theo} , the measured ion beam current I_b^{Exp} , as a function of changing aperture number.

Aperture No.	V_a (V)	δV_a (V)	I_b^{Theo} (μA)	δI_b^{Theo} (μA)	I_b^{Exp} (μA)	δI_b^{Exp} (μA)
1	1765	± 10	2.35	± 0.02	10.29	± 0.15
2	2340	± 10	7.19	± 0.02	102.98	± 1.45
4	3435	± 10	25.57	± 0.03	135.79	± 1.91

Table. 7.2 show a large discrepancy between the theoretical and measured ion current, suggesting the measured beam current is much greater than theoretically predicted. It must be noted that I_b^{Theo} gives the total current exiting the thruster. However, the current measured at the plate may not be the same as the total current leaving the thruster. As noted by [11], the measurement of the ion beam current is affected by the presence of secondary electrons generated from ion impacts on the collector plate, as well as the presence of ambient neutral gas particles along the beam path. Collisions between the various particle species may have generated the excess ion current observed. Moreover, the ion plume may have had an excess of electrons, generated from collisional and surface processes, and since the ion collector plate was not negatively biased to reflect these electrons, the measured current may have been a combination of both ion and electron currents. This would suggest that the current experimental setup may not be ideal for producing exact measurements of the ion beam current.

7.6.3 Characterising the thruster efficiency as a function of changing aperture number

Ion production efficiency

As mentioned previously, the ion production efficiency (or discharge loss), denoted as η_d , indicates the energy cost of ion production. Fig.7.17 shows the calculated values of η_d using the data gathered from the experiments. The discharge loss for a single aperture system configuration is found to be 0.170 ± 0.003 W/ μA . This indicates that 170 ± 3 mW of discharge power is required to produce 1 μA of ion current or roughly 170 000 eV is required to produce a single ion in the extracted beam. This is significantly larger than the ion production cost observed in most gridded ion engines (about 250-1000 eV per ion [19]). The discharge loss decreases substantially with the addition of the second aperture and then rises slightly when four apertures are used. Note that it is desirable to have η_d as low as possible, as this would indicate a minimum amount of discharge power required to produce a

single μA of beam current. From Fig.7.17, the 2x2 mm configuration appears to display the best ion production efficiency, i.e. it requires the least amount of discharge power, at roughly $23.0 \pm 0.4 \text{ mW}$, to produce $1 \mu\text{A}$ of ion beam current.

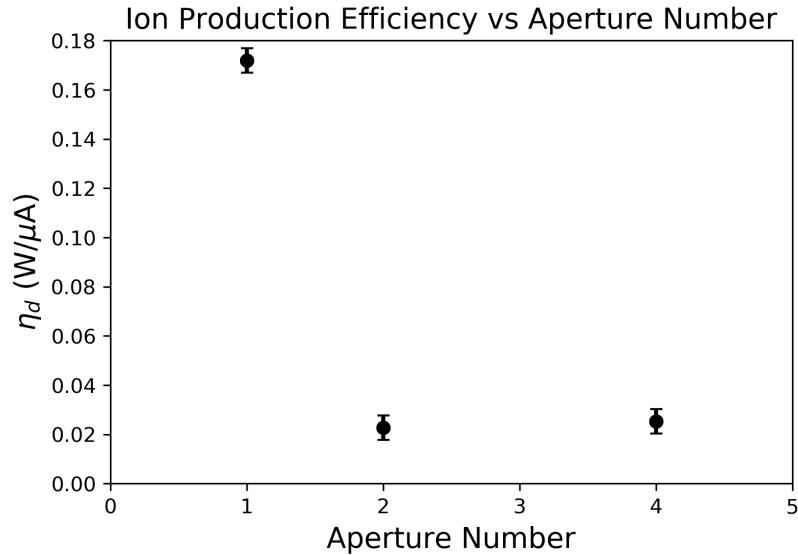


Fig. 7.17 The ion production efficiency vs aperture number at 1 mA discharge current.

Electrical efficiency

The thruster's electrical efficiency, denoted as η_e , can be calculated using the measured data and equation (7.10). It represents the efficiency of converting the input power into useful beam power that then contributes to thrust. Fig.7.18 shows how the thruster's electrical efficiency varies with additional apertures. For a single aperture system the electrical efficiency is relatively low at just 1% ($\pm 0.02 \%$). This implies that the power of the extracted beam (the useful power) is far less than the total power consumption. The electrical efficiency is observed to increase significantly with the addition of a second aperture but then starts to plateau at four apertures. The 4x2 mm configuration displays the highest electrical efficiency at roughly 11% ($\pm 0.17 \%$). This is still considerably lower than the efficiencies of most electric micropropulsion systems (refer to Appendix A for examples). Note however that at higher discharge currents the electrical efficiency is expected to increase based on equation (7.18).

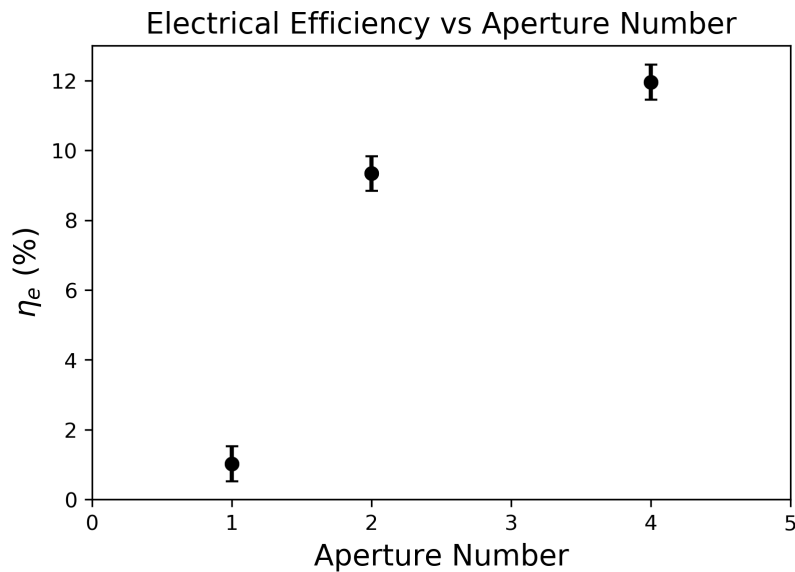


Fig. 7.18 The electrical efficiency vs aperture number at 1 mA discharge current.

Thrust-to-power ratio

Fig.7.19 provides an indication of the estimated thrust per unit input power as a function of aperture number at a constant discharge current of 1 mA. The ratio is observed to increase rapidly from a single to a double aperture configuration and begins to plateau at four apertures. In the four aperture configuration, the thrust-to-power ratio reaches $0.60 \pm 0.03 \mu\text{N/W}$, which implies that the system generates $0.60 \pm 0.03 \mu\text{N}$ of thrust for every Watt of total input power. The typical thrust-to-power ratio for various electric micropropulsion concepts is provided in Fig.A.2. Resistojets are found to exhibit the highest thrust-power-ratios with some systems exceeding $200 \mu\text{N/W}$. Pulsed Plasma Thrusters exhibit the lowest thrust-power ratios (ranging from 2- $20 \mu\text{N/W}$). This is still significantly higher than the inferred thrust-to-power ratios for the proof-of-concept studied in this work and alludes to fact that the system requires some serious modifications if it is to be developed into a working micropropulsion device.

It is worth noting that the figures shown here do not give an accurate representation of the actual thrust-power ratio of the system but serve as an indication of the potential relationship between the number of apertures and the estimated thrust-power ratio of the system. From these observations, it appears that the thrust per unit of input power does not increase linearly with the number of apertures. As mentioned previously, a larger sample set of apertures is required to establish a true pattern.

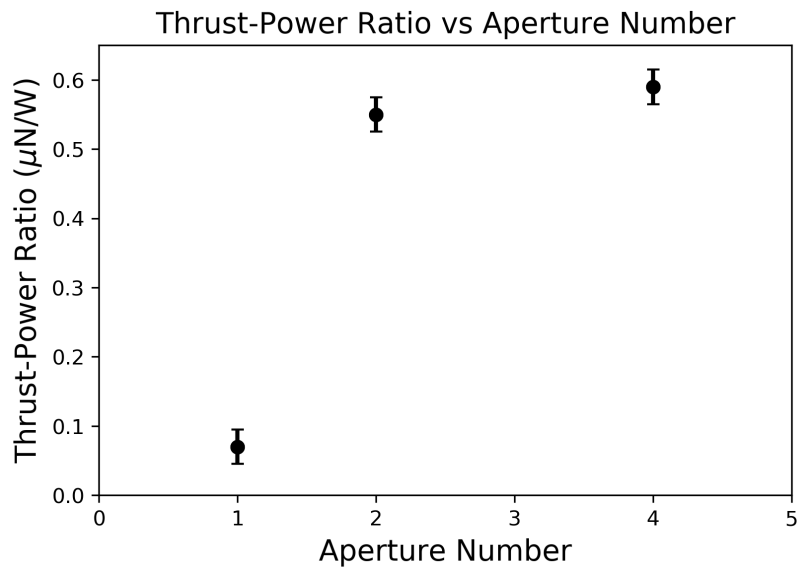


Fig. 7.19 The thrust-to-power ratio vs aperture number at 1 mA discharge current.

Experimental Aftermath

Damage to the thruster's discharge chamber and the electrodes contribute greatly towards the decline of the operational lifetime of the thruster. It is therefore worthwhile assessing the damage to the various thruster components, after all of the experiments have been conducted, to determine what the major contributors of this damage are and to potentially mitigate these detrimental effects from occurring in future iterations of the thruster concept.

After numerous experimental tests conducted on the 1x2 mm and 2x2 mm thruster configurations, the thrusters eventually ceased to operate in a stable manner (i.e. a stable discharge was not obtainable). The nylon gas feed inlet thread was removed and observed to have been significantly damaged (see Fig.7.20). It appears that the end of the thread had burnt out from being in direct contact with the discharge plasma. From the cross section of the tube, seen in Fig.7.20, it is evident that the debris from the nylon thread had spread across the walls of the tube more so towards the cathode end (see Fig.7.21). There also seems to be a large concentration of blackened debris at the openings of the thruster, and on the outer surface of the electrodes, particularly at the cathode end. This is most probably the result of the discharge plasma interacting with the adhesive used to bond the electrodes to the thruster openings.

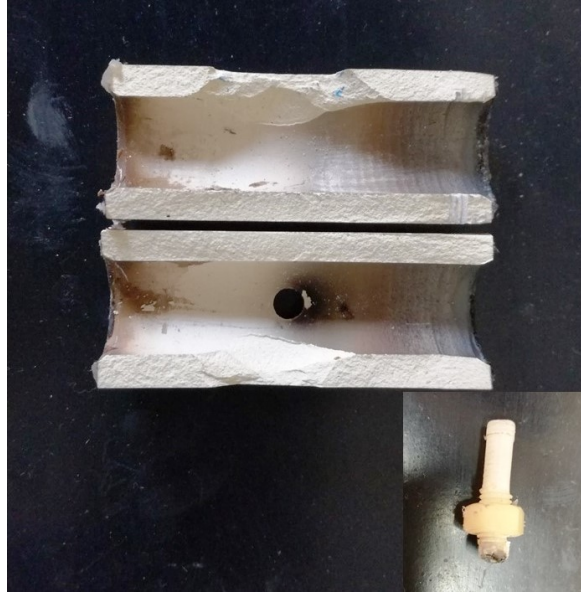


Fig. 7.20 The cross section of the 2x2 mm electrode aperture thruster discharge tube reveals the formation of debris collected on the walls of the discharge channel. The debris may be a result of the burnt out residue from the nylon gas feed inlet thread (bottom right).

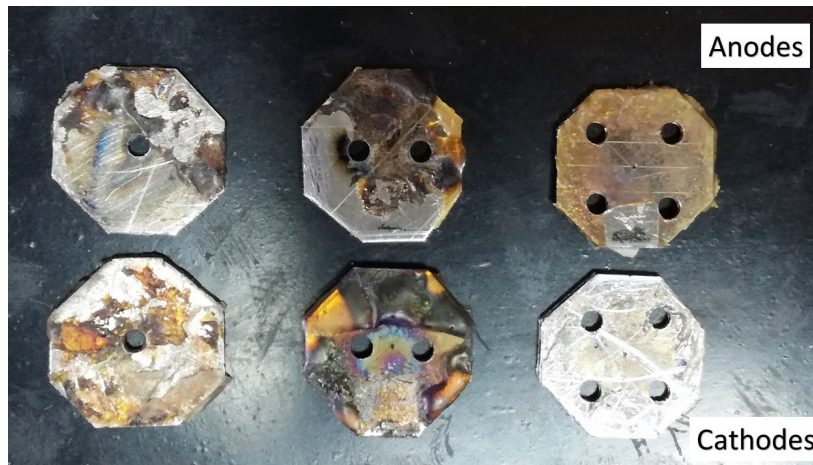


Fig. 7.21 The formation of black debris on the outer surface of the electrodes, most likely caused by the interaction of the discharge plasma and the adhesive used to bond the electrodes to the thruster. Top: plasma electrodes. Bottom: extractor electrodes.

The U-shaped DC discharge microthruster studied in [2] had experienced a similar issue of debris build-up in the discharge channel of the thruster. There it was hypothesised that the debris could have formed from the interaction of the high temperature discharge plasma with the materials of the thruster's components. Wright [2] notes that the blocking of the thruster channel by debris may be a significant contributor to thruster failure. It is therefore

vital for one to meticulously select the appropriate construction materials to mitigate such effects. In this case, it is recommended that the gas inlet thread be made of some ceramic material instead of a synthetic polymer like nylon. The Al_2O_3 ceramic used for the discharge channel appears to withstand the high temperature plasma relatively well. Moreover, one should limit, or completely eradicate, the use of adhesives when connecting the electrodes to the thruster openings. The electrodes should be securely placed through narrow slits or clamped at the ends of the thruster without the need for adhesive bonding.

7.7 Conclusions

Experimental tests were conducted on the thruster concept, including investigations on how the system's electrical characteristics changed with changes in the number of extraction apertures, as well as measurements of the extracted ion beam current as a function of changing aperture number. These experiments were conducted with a direct propellant feed into the thruster.

In each of the configurations explored, the thruster was observed to operate stably within a very narrow range of input parameters, i.e. the applied voltage and the propellant mass flow rate. Further increases in the applied voltage and/or propellant flow rate beyond the stable operating point led to unstable discharge behaviour. In all of the aperture configurations explored, the V-I curves tend to follow the relationship dictated by the Child Langmuir law (i.e. $I_d \propto V_a^{3/2}$) and are found to be in good agreement with the literature. Increasing the number of apertures on the electrodes results in a downward shift in the characteristic V-I curves (i.e. a higher applied voltage is required to obtain a particular discharge current with the addition of subsequent apertures). This is probably attributed to the loss of charged particles from the discharge channel to the ion beam as a result of increasing orifices. The ideal propellant flow rate for optimal ion beam extraction is found to be between $\sim 180\text{-}300$ ng/s across all aperture configurations. When the flow rate is increased (within this stable operating range) the ionisation rate within the discharge channel increases and a lower acceleration voltage is required to obtain a particular discharge current for a fixed aperture number.

The second part of these experiments involved characterising the magnitude of the extracted ion current as a function of aperture number. The measured beam current tends to increase drastically (~ 10 fold) from a single to a double aperture system, but then begins to plateau with the addition of subsequent apertures. These measurements seem to refute the initial hypothesis which predicted that the ion current would increase in proportion to

the aperture number. Furthermore, the measured ion current was found to be in excess of the theoretical prediction by the Child-Langmuir equation. This discrepancy may be attributed to a non-ideal experimental setup. It will therefore be necessary to use a more sophisticated measuring apparatus, for example, a Faraday cup probe, to make more accurate measurements of the ion beam current. Note, however, that using a Faraday cup may lead to a reduction in resolution.

The ion beam current measurements were then used to obtain estimates of the system's performance metrics, namely: the ion production efficiency, electrical efficiency, estimated thrust and the expected thrust per unit of input power, at a constant discharge current of 1 mA. It must be emphasised that these calculated performance metrics may not be entirely accurate due to inaccuracies in the measurement of the ion beam current. Nevertheless, they provide useful insights on how the system's performance changes with changes in electrode aperture number. Findings suggest that the 2x2 mm aperture configuration produces the best ion production efficiency (lowest discharge loss), however, the 4x2 mm aperture configuration displays a slightly better electrical efficiency. These experiments have verified that a microthruster based on an ionisation-acceleration coupling mechanism can work in principle and can produce a thrust on the order of a few micro-Newtons. Direct measurements of the system's thrust can be conducted to confirm if this is in fact the case. The main purpose of these experiments, namely to determine ion beam (and related thrust) production, and estimated thruster efficiency with various electrode apertures, was successfully demonstrated. These results justify a more in-depth investigation as being required.

After numerous experimental tests, the thruster containing the 1x2 mm and 2x2 mm aperture electrodes eventually failed to fire. Upon analysing both discharge tubes, a small amount of debris had been found scattered across the discharge channel and on the electrode's surface. It is hypothesised that this debris had originated from the burnt out nylon gas inlet thread, after interacting with the discharge plasma. It is recommended that future iterations of the thruster concept be void of any adhesives or plastic components, as these materials may contribute significantly to the degradation and eventual failure of the thruster.

Chapter 8

Research Summary and Conclusions

In this work, a DC discharge-based microthruster concept was developed to meet the growing demand for reliable, energy efficient propulsion systems on the nanosatellite (CubeSat) platform. The system is hypothesised to work in a similar way to a glow discharge tube with openings at each electrode. The orifices allow for charged particles (ions and electrons), generated from an electrically induced plasma, to escape the system and provide a net thrust. A notable advantage of this system is that it utilises the same electric field to generate and accelerate the charged species of the plasma for thrust production. This ionisation-acceleration coupling mechanism aims to address the tight energy and mass budget restrictions imposed on the nanosatellite platform and could potentially lead to a reliable, versatile, and energy efficient thruster that may favourably compete with other systems on the market.

In the context of CubeSat science missions, on-board micropropulsion systems would enhance both the lifetimes and operational capabilities of CubeSats and will be mandatory for constellation missions that require swarms of CubeSats flying in formation. Such CubeSat missions may contribute to major advancements in space science and particularly particle cosmology by allowing for observations to be made across portions of the EM spectrum not accessible to ground based observatories on Earth [79].

The early chapters of this dissertation covered the main principles of propulsion and provided an overview of the various types of micropropulsion systems available on the market, and in some cases systems with a proven flight heritage, along with novel concepts that are yet to be developed and tested. This was followed by a discussion on the basic plasma physics required to understand the underlying mechanisms of the DC discharge microthruster concept. A comprehensive theoretical description of the processes governing DC glow discharges was presented. The theory was further strengthened through an argon glow discharge simulation

which aimed to understand the axial variation of plasma parameters along the discharge length. The results of the simulation provided a deeper insight into the electric field characteristics across the discharge plasma, which to a large extent determines the system's thrust.

The bulk of this research involved subjecting the thruster concept to various experimental tests which served to characterise the system's electrical behaviour under different operating parameters. These included: tests to verify the system's hypothesised operating mechanism, to determine the system's optimal set of operating parameters, along with tests of the system's stability and repeatability characteristics, and measurements of the total extracted ion beam current under different system configurations. Overall, the main objectives of this research have been met, namely:

- The system's hypothesised mechanism of operation (i.e. ionisation-acceleration coupling) has been verified and an optimal set of stable operating parameters, under the cylindrical geometry, has been identified.
- The thruster's discharge characteristics, i.e. the discharge current as a function of applied voltage and changing aperture number, were studied and are found to be in good agreement with theory.
- The extracted ion beam current had been measured from which various performance metrics, i.e. thrust and efficiency, of the thruster under various electrode aperture configurations had been estimated. These measured values deviated significantly from the theoretical values and the discrepancy may largely be due to a non-ideal experimental setup.

From the results obtained in these studies, no conclusive statements can be drawn about the overall feasibility of the thruster concept, and it is evident from these early results that the system requires many modifications before it can be fully adapted into a working micropropulsion device. One major critique of this system is that it utilises gaseous propellant from a propellant tank as fuel. Since the propellant tank is usually the largest subsystem on the spacecraft, this could be a major disadvantage that prevents the further development of the thruster concept into a fully functioning prototype. Furthermore, results from the experiments conducted thus far seem to indicate that the system has poor lifetime characteristics which is a highly undesirable trait for propulsion systems. Nonetheless, the experiments presented in this research may act as an important stepping-stone towards more detailed studies of the thruster concept.

Recommendations and Future Outlook

Some recommendations for future studies to be conducted on the system are presented below:

- Firstly, the thruster should be reconstructed and should not consist of any plastic components or require any adhesives to attach the electrodes to its open ends. These components should be manufactured from companies specialising in such components. A "cleaner" system is likely to produce more accurate results and improve the operational lifetime of the thruster.
- Once a "cleaner" system is developed, studies should be conducted on what effect variations in the geometry of the system (i.e the discharge length and radius) would have on the operation of the thruster.
- A larger sample set of extraction apertures should be experimented with. One may also investigate the effect of using a different number of apertures on the extractor electrode in relation to the plasma electrode. One can also investigate how the system behaves under a pulsed mode of operation.
- A power supply with a higher output voltage and current should be utilised to maximise the available discharge current and subsequently the extracted ion current in the thrust beam.
- Measurements of the extracted ion beam current should be done more carefully with the use of Faraday cup probe. Using a Faraday cup would also allow for the ion current density distribution to be determined.
- A highly sensitive thrust measurement stand, capable of measuring forces on the order of a few micro-Newtons, should be developed and utilised to directly measure the thrust of the system and compare the measured values to the estimates obtained in this research.
- Three dimensional simulations can be developed to better understand the underlying mechanisms of the thruster and to gain more insight into its expected behaviour under varying conditions.
- Measurements of the plasma potential, electron density and electron temperature can be conducted with the aid of a Langmuir probe and can be compared to the results of simulations.

References

- [1] NASA CubeSat Launch Initiative et al. Cubesat 101: Basic concepts and processes for first-time cubesat developers. *no. October*, page 96, 2017.
- [2] William Patrick Wright. *Characterization of direct current discharge based electric microthrusters*. PhD thesis, 2017.
- [3] J Douglas Liddle, Antony P Holt, Susan J Jason, Kathryn A O'Donnell, and Edward J Stevens. Space science with cubesats and nanosatellites. *Nature Astronomy*, 4(11): 1026–1030, 2020.
- [4] Charles D Norton, Sergio Pellegrino, Michael Johnson, Manan Arya, John Steeves, Shri Kulkarni, and Christopher D Martin. *Small satellites: a revolution in space science*. 2014.
- [5] Akshay Reddy Tummala and Atri Dutta. An overview of cube-satellite propulsion technologies and trends. *Aerospace*, 4(4):58, 2017.
- [6] B Ripin, R Decoste, G Doschek, U Feldman, R Lehmborg, E McLean, and J Stamper. Optical diagnostics of laser-fusion plasmas. *IEEE Journal of Quantum Electronics*, 13(9):846–846, 1977.
- [7] Michael A Lieberman and Alan J Lichtenberg. *Principles of plasma discharges and materials processing*. John Wiley & Sons, 2005.
- [8] Carlos Sánchez Lara. Design and performance analysis study of an ion thruster. B.S. thesis, Universitat Politècnica de Catalunya, 2016.
- [9] Jon Tomas Gudmundsson and Ante Hecimovic. Foundations of dc plasma sources. *Plasma Sources Science and Technology*, 26(12):123001, 2017.
- [10] M Krommenhoek. *Modelling of the propulsion mechanism for a miniaturized corona ionization thruster*. PhD thesis, Master's thesis, University of the Witwatersrand, 2015.
- [11] Ian G Brown. *The physics and technology of ion sources*. John Wiley & Sons, 2004.
- [12] EA Bogdanov, SF Adams, VI Demidov, AA Kudryavtsev, and JM Williamson. Influence of the transverse dimension on the structure and properties of dc glow discharges. *Physics of Plasmas*, 17(10):103502, 2010.
- [13] John Allmen and Andrew Petro. Small spacecraft technology. In *Proc. of the 28th Annu. AIAA/USU Conf. on Small Satellites, Logan, UT*, 2014.

- [14] Arash Mehrparvar, D Pignatelli, J Carnahan, R Munakat, W Lan, A Toorian, A Huputanasin, and S Lee. Cubesat design specification rev. 13. *The CubeSat Program, Cal Poly San Luis Obispo, US*, 1(2), 2014.
- [15] Ryan Hevner, Walter Holemans, Jordi Puig-Suari, and Robert Twiggs. An advanced standard for cubesats. 2011.
- [16] Jakob Fromm Pedersen. Cubesat educational payload on the vega maiden flight. *Interface Control Document*, 2009.
- [17] Juergen Mueller and Juergen Mueller. Thruster options for microspacecraft-a review and evaluation of existing hardware and emerging technologies. In *33rd joint propulsion conference and exhibit*, page 3058, 1997.
- [18] Chiara Palla and Jennifer Kingston. Forecast analysis on satellites that need de-orbit technologies: future scenarios for passive de-orbit devices. *CEAS Space Journal*, 8(3): 191–200, 2016.
- [19] Dan M Goebel and Ira Katz. *Fundamentals of electric propulsion: ion and Hall thrusters*, volume 1. John Wiley & Sons, 2008.
- [20] James Sovey, Vincent Rawlin, and Michael Patterson. A synopsis of ion propulsion development projects in the united states-sert i to deep space 1. In *35th Joint Propulsion Conference and Exhibit*, page 2270, 1999.
- [21] P Ferrer and MP Tchonang. Miniaturization of electrostatic ion engines by ionization and acceleration coupling. *Journal of Physics D: Applied Physics*, 44(33):335204, 2011.
- [22] Marius Tchonang Pokaha. *Modeling of the corona ionization space propulsion system*. PhD thesis, Citeseer, 2011.
- [23] CR Dougherty, TD Foulke, JD Harden, TL Hewitt, FN Peters, RD Smith, and JW Tuttle. Glow lamp manual, 1966.
- [24] JA Tauber, ESA, the Planck Scientific Collaboration, et al. The planck mission. *Advances in Space Research*, 34(3):491–496, 2004.
- [25] Ewan S Douglas, Kerri L Cahoy, Mary Knapp, and Rachel E Morgan. Cubesats for astronomy and astrophysics. *arXiv preprint arXiv:1907.07634*, 2019.
- [26] NASA SBIR. Phase i solicitation. *H3 Life support and habitation systems*, pages 1–4, 2016.
- [27] Philip Kaaret, A Zajczyk, DM LaRocca, R Ringuette, J Bluem, W Fuelberth, H Gulick, K Jahoda, TE Johnson, DL Kirchner, et al. Halosat: a cubesat to study the hot galactic halo. *The Astrophysical Journal*, 884(2):162, 2019.
- [28] Paul J McMillan. Mass models of the milky way. *Monthly Notices of the Royal Astronomical Society*, 414(3):2446–2457, 2011.
- [29] TM Dame. The distribution of neutral gas in the milky way. In *AIP Conference Proceedings*, volume 278, pages 267–278. American Institute of Physics, 1992.

- [30] Jonás Chaves-Montero, Carlos Hernández-Monteagudo, Raúl E Angulo, and JD Emberson. Measuring the evolution of intergalactic gas from $z=0$ to 5 using the kinematic sunyaev–zel’dovich effect. *Monthly Notices of the Royal Astronomical Society*, 503(2): 1798–1814, 2021.
- [31] FABRIZIO Nicastro, J Kaastra, Y Krongold, STEFANO Borgani, E Branchini, R Cen, MAURO Dadina, CW Danforth, M Elvis, Fabrizio Fiore, et al. Observations of the missing baryons in the warm–hot intergalactic medium. *Nature*, 558(7710):406–409, 2018.
- [32] K Belov, A Branch, S Broschart, J Castillo-Rogez, S Chien, L Clare, R Dengler, J Gao, D Garza, A Hegedus, et al. A space-based decametric wavelength radio telescope concept. *Experimental Astronomy*, 46(2):241–284, 2018.
- [33] David Krejci and Paulo Lozano. Space propulsion technology for small spacecraft. *Proceedings of the IEEE*, 106(3):362–378, 2018.
- [34] Edward Beshore, Dante Lauretta, William Boynton, Christopher Shinohara, Brian Sutter, David Everett, Jonathan Gal-Edd, Ronald Mink, Michael Moreau, and Jason Dworkin. The osiris-rex asteroid sample return mission. In *2015 IEEE Aerospace Conference*, pages 1–14. IEEE, 2015.
- [35] Yuichi Tsuda, Makoto Yoshikawa, Masanao Abe, Hiroyuki Minamino, and Satoru Nakazawa. System design of the hayabusa 2—asteroid sample return mission to 1999 ju3. *Acta Astronautica*, 91:356–362, 2013.
- [36] P McNamara, S Vitale, Karsten Danzmann, LISA Pathfinder Science Working Team, et al. Lisa pathfinder. *Classical and quantum gravity*, 25(11):114034, 2008.
- [37] Robert G Jahn and Edgar Y Choueiri. Encyclopedia of physical science and technology. *Academic Press*, 3:125–141, 2002.
- [38] John Slough, Samuel Andreason, Timothy Ziemba, and JJ Ewing. Micro-discharge micro-thruster. In *41st AIAA/ASME/SAE/ASEE Joint Propulsion Conference & Exhibit*, page 4074, 2005.
- [39] Christopher Ogunlesi, Angelo Grubisic, Federico Romei, Matthew Robinson, Paul Aimone, Francois Dary, Dave Gibbon, Mike Curtis-Rouse, et al. Novel non-destructive inspection of the star additively manufactured resistojet. 2018.
- [40] Andrew D Ketsdever, Dean C Wadsworth, and EP Muntz. Gas-surface interaction model influence on predicted performance of microelectromechanical system resistojet. *Journal of Thermophysics and Heat Transfer*, 15(3):302–307, 2001.
- [41] Kazuya Yaginuma, Jun Asakawa, Yuichi Nakagawa, Yoshihiro Tsuruda, Hiroyuki Koizumi, Kota Kakihara, Kanta Yanagida, Yusuke Murata, Mikihiro Ikura, Shuhei Matsushita, et al. Aqt-d: Cubesat demonstration of a water propulsion system deployed from iss. *TRANSACTIONS OF THE JAPAN SOCIETY FOR AERONAUTICAL AND SPACE SCIENCES, AEROSPACE TECHNOLOGY JAPAN*, 18(4):141–148, 2020.

- [42] Riki H Lee, AM Bauer, Miles D Killingsworth, TC Lilly, JA Duncan, and AD Ketsdever. Free-molecule-microresistojet performance using water propellant for nanosatellite applications. *Journal of Spacecraft and Rockets*, 45(2):264–269, 2008.
- [43] Hans Leiter, Hartwig Ellerbrock, Marcel Berger, Michael Boss, Davar Feili, Benjamin Lotz, and Davina Di Cara. Development of a miniaturized rf ion engine system for commercial and scientific applications. In *47th AIAA/ASME/SAE/ASEE Joint Propulsion Conference & Exhibit*, page 6070, 2011.
- [44] Michael Tsay, John Frongillo, Jurg Zwahlen, and Lenny Paritsky. Maturation of iodine fueled bit-3 rf ion thruster and rf neutralizer. In *52nd AIAA/SAE/ASEE Joint Propulsion Conference*, page 4544, 2016.
- [45] Edwin H Hall et al. On a new action of the magnet on electric currents. *American Journal of Mathematics*, 2(3):287–292, 1879.
- [46] Käthe Dannenmayer and Stéphane Mazouffre. Elementary scaling relations for hall effect thrusters. *Journal of Propulsion and Power*, 27(1):236–245, 2011.
- [47] David Krejci, Fernando Mier-Hicks, Robert Thomas, Thomas Haag, and Paulo Lozano. Emission characteristics of passively fed electrospray microthrusters with propellant reservoirs. *Journal of Spacecraft and Rockets*, 54(2):447–458, 2017.
- [48] Michael Keidar, Iain D Boyd, and Isak I Beilis. Model of particulate interaction with plasma in a teflon pulsed plasma thruster. *Journal of Propulsion and Power*, 17(1):125–131, 2001.
- [49] Pavlos Mikellides and P Turchi. Modeling of late-time ablation in teflon pulsed plasma thrusters. In *32nd Joint Propulsion Conference and Exhibit*, page 2733, 1996.
- [50] Kurt A Polzin. Comprehensive review of planar pulsed inductive plasma thruster research and technology. *Journal of Propulsion and Power*, 27(3):513–531, 2011.
- [51] Michael Keidar. Micro-cathode arc thruster for small satellite propulsion. In *2016 IEEE Aerospace Conference*, pages 1–7. IEEE, 2016.
- [52] James E Polk, Michael J Sekerak, John K Ziemer, Jochen Schein, Niansheng Qi, and Andre Anders. A theoretical analysis of vacuum arc thruster and vacuum arc ion thruster performance. *IEEE Transactions on Plasma Science*, 36(5):2167–2179, 2008.
- [53] Jonathan Kolbeck, Joseph Lukas, George Teel, Michael Keider, Edward Hanlon, Jacob Pittman, Morgan Lange, and Jin Kang. μ cat micro-propulsion solution for autonomous mobile on-orbit diagnostic system. 2016.
- [54] Les Johnson, Mark Whorton, Andy Heaton, Robin Pinson, Greg Laue, and Charles Adams. Nanosail-d: A solar sail demonstration mission. *Acta Astronautica*, 68(5-6):571–575, 2011.
- [55] Y Tsuda, Osamu Mori, Ryu Funase, H Sawada, T Yamamoto, T Saiki, T Endo, and Jun'ichiro Kawaguchi. Flight status of ikaros deep space solar sail demonstrator. *Acta Astronautica*, 69(9-10):833–840, 2011.

- [56] Rex W Ridenoure, Riki Munakata, Stephanie D Wong, Alex Diaz, David A Spencer, Douglas A Stetson, Bruce Betts, Barbara A Plante, Justin D Foley, and John M Bellardo. Testing the lightsail program: Advancing solar sailing technology using a cubesat platform. *Journal of Small Satellites*, 5(2):531–550, 2016.
- [57] Jae-Hoon Kim, Mi-Ae Lee, Geum-Jun Han, and Byeong-Hoon Cho. Plasma in dentistry: a review of basic concepts and applications in dentistry. *Acta Odontologica Scandinavica*, 72(1):1–12, 2014.
- [58] LA Artsimovich. Tokamak devices. *Nuclear Fusion*, 12(2):215, 1972.
- [59] Francis F Chen et al. *Introduction to plasma physics and controlled fusion*, volume 1. Springer, 1984.
- [60] Paul Harding Rutherford. *Introduction to plasma physics*. Inst of Physics Pub Incorporated, 1995.
- [61] Merle Hirsh. *Gaseous electronics*, volume 1. Elsevier, 2012.
- [62] VA Lisovskiy, SD Yakovin, and VD Yegorenkov. Low-pressure gas breakdown in uniform dc electric field. *Journal of Physics D: Applied Physics*, 33(21):2722, 2000.
- [63] COMSOL Multiphysics and CMHT Module. Comsol multiphysics user’s guide. *Version: COMSOL Multiphysics*, 3, 2014.
- [64] Casper V Budtz-Jorgensen. *Studies of electrical plasma discharges*. PhD thesis, Faculty of Science, Aarhus University, 2000.
- [65] Av V Phelps. Cross sections and swarm coefficients for nitrogen ions and neutrals in n₂ and argon ions and neutrals in ar for energies from 0.1 ev to 10 kev. *Journal of Physical and Chemical Reference Data*, 20(3):557–573, 1991.
- [66] J Temple Black and Ronald A Kohser. *DeGarmo’s materials and processes in manufacturing*. John Wiley & Sons, 2017.
- [67] Roger C Baker. *Flow measurement handbook: industrial designs, operating principles, performance, and applications*. Cambridge University Press, 2005.
- [68] P Allison, JD Sherman, and HV Smith. Report la-8808-ms, los alamos nat, 1981.
- [69] SP Nikulin. The effect of ion emission on the characteristics of a glow discharge with a hollow cathode. *Technical Physics*, 45(10):1351–1353, 2000.
- [70] Hans Henrik Andersen, HL Bay, MT Robinson, and HE Roosendaal. *Sputtering by Particle Bombardment: Physical Sputtering of Single-element Solids*. Springer, 1981.
- [71] F Llewellyn-Jones. The mechanism of electrode erosion in electrical discharges. *Platinum Metals Review*, 7(2):58–65, 1963.
- [72] Sidney A Self. Exact solution of the collisionless plasma-sheath equation. *The physics of Fluids*, 6(12):1762–1768, 1963.

- [73] Peng Zhang, Yee Sin Ang, Allen L Garner, Ágúst Valfells, JW Luginsland, and LK Ang. Space-charge limited current in nanodiodes: Ballistic, collisional, and dynamical effects. *Journal of Applied Physics*, 129(10):100902, 2021.
- [74] CD Child. Discharge from hot cathode. *Physical Review (Series I)*, 32(5):492, 1911.
- [75] Irving Langmuir and Karl T Compton. Electrical discharges in gases part ii. fundamental phenomena in electrical discharges. *Reviews of modern physics*, 3(2):191, 1931.
- [76] Charles H Hocart. 9.10 mass spectrometry: An essential tool for trace identification and quantification. *Comprehensive Natural Products II*, pages 327–388, 2010.
- [77] Mohammed K Khalaf, Oday A Hammadi, and Firas J Kadhim. Current-voltage characteristics of dc plasma discharges employed in sputtering techniques. *Iraqi Journal of Applied Physics*, 12(3), 2016.
- [78] H El-Khabeary. Study of the parameters affecting ion beam emerging from cold conical cathode ion source. *Brazilian Journal of Physics*, 40:327–332, 2010.
- [79] Dayton L Jones. Cubesat missions for low frequency radio astronomy. In *American Astronomical Society Meeting Abstracts# 221*, volume 221, pages 350–01, 2013.
- [80] Ian Coxhill and David Gibbon. A xenon resistojet propulsion system for microsattellites. In *41st AIAA/ASME/SAE/ASEE Joint Propulsion Conference & Exhibit*, page 4260, 2005.
- [81] Philip Davies, Phil Whittaker, Rachel Bird, Luis Gomes, Ben Stern, Martin Sweeting, Martin Cohen, and David Hall. Novasar—bringing radar capability to the disaster monitoring constellation. 2012.
- [82] DLJM Carroll, RLB Cardin, RL Burton, GF Benavides, N Hejmanowski, C Woodruff, K Bassett, D King, J Laystrom-Woodard, L Richardson, et al. Propulsion unit for cubesats (puc). In *Proceedings of the 62nd JANNAF Propulsion Meeting (7th Spacecraft Propulsion)*, Nashville, TN, USA, pages 1–5, 2015.
- [83] Robert S Legge, Emily B Clements, and Adam Shabshelowitz. Enabling microsatellite maneuverability: A survey of microsatellite propulsion technologies. In *2017 IEEE MTT-S International Microwave Symposium (IMS)*, pages 229–232. IEEE, 2017.
- [84] Kristina Lemmer. Propulsion for cubesats. *Acta Astronautica*, 134:231–243, 2017.
- [85] Natasha Bosanac, Andrew D Cox, Kathleen C Howell, and David C Folta. Trajectory design for a cislunar cubesat leveraging dynamical systems techniques: The lunar icecube mission. *Acta Astronautica*, 144:283–296, 2018.
- [86] H Leiter, C Altmann, R Kukies, et al. Evolution of the airbus ds gmbh radio frequency ion thruster family. In *Proceedings of the Joint Conference of 30th ISTS, 34th IEPC and 6th NSAT, Kobe-Hyogo, Japan*, pages 4–10, 2015.
- [87] Garrett D Reed, William A Hargus, and Douglas B VanGilder. Comparison of numerical and experimental near-field plasma properties of the bht-200-x3 hall thruster (preprint). Technical report, AIR FORCE RESEARCH LAB EDWARDS AFB CA PROPULSION DIRECTORATE, 2006.

-
- [88] V Salvatore, F Battista, D Ricci, and M Invigorito. Cira development activities in electric propulsion testing. In *Proceedings of the 66th International Astronautical Congress, Jerusalem, Israel*, pages 12–16, 2015.
- [89] Juergen Mueller, John Ziemer, Richard Hofer, Richard Wirz, and Timothy O’Donnell. A survey of micro-thrust propulsion options for microspacecraft and formation flying missions. In *5th Annual CubeSat Developers Workshop San Luis Obispo, CA*, 2008.
- [90] David Krejci, Fernando Mier-Hicks, Corey Fucetola, Paulo Lozano, Andrea Hsu Schouten, and Francois Martel. Design and characterization of a scalable ion electro-spray propulsion system. 2015.
- [91] Douglas Spence, Eric Ehrbar, Nathan Rosenbald, Nathaniel Demmons, Thomas Roy, Samuel Hoffman, Wallace D Williams, Michael Tsay, Jurg Zwahlen, Kurt Hohman, et al. Electro-spray propulsion systems for small satellites and satlets. In *AIAA SPACE 2013 Conference and Exposition*, page 5329, 2013.
- [92] John Ziemer, Manuel Gamero-Castaño, Vlad Hruby, Doug Spence, Nate Demmons, Ryan McCormick, Tom Roy, Chas Gasdaska, John Young, and Bill Connolly. Colloid micro-newton thruster development for the st7-drs and lisa missions. In *41st AIAA/ASME/SAE/ASEE Joint Propulsion Conference & Exhibit*, page 4265, 2005.
- [93] Mark Campbell, Adam Bruckner, Ralph Ewig, Emilio Beltran, Esther Carlson, Kirsten Carpenter, Seung Chung, Benjamin Davenport, Farshad Forouhar, John Halligan, et al. Uw dawgstar: One third of ion-f-an element of the ionospheric observation nanosatellite formation (ion-f). 1999.
- [94] Joseph B Robinson and David J Richie. Stabilization and attitude determination methods for falconsat-3. *Journal of Spacecraft and Rockets*, pages 507–519, 2016.

Appendix A

Performance Comparison of Electric Thruster Varieties

Table A.1 Table showing the performance parameters for various thruster varieties

Thruster Type	Engine name	Thrust (mN)	Specific Impulse (s)	Power (W)	Propellant
Resistojet	LPR [80, 81]	18	48	30	Xe
	PUC [82, 83]	5.4	65	15	SO ₂
	FMMR [42]	0.129	79.2	~ 15	Water
RF Ion Engine	BIT-1 [84, 44]	0.1- 0.18	2150- 3200	28	Xe, Iodine
	BIT-3 [44, 85]	1.15	2500	75	Iodine
	RIT-muX [86]	0.05-0.5	300- 3000	< 50	Xe
Hall Thruster	BHT-200 [87]	12.8	1390	200	Xe, I, Kr
	HT-400 [88]	50	1750	100	Xe
	MHT-9 [89]	20-50	300-1500	30-200	-
Electrospray	S-iEPS [90]	0.1	1200	1.5	Ionic liquid
	TILE-5000 [83]	1.5	1800	30	Ionic liquid
	BET-1mN [91, 92]	0.7	800	< 9	Ionic liquid
PPT	EO-1 PPT [93]	0.14	1150	12.5	Teflon
	MPACS [94]	0.144	830	< 10	Teflon
VAT	μ CAT [53]	0.001-0.02	3000	< 10	Nickel

Using operational data obtained from various suppliers the thrust, power and thrust-to-power ratio in relation to the specific impulse of various electric propulsion systems can be determined. These are shown in Fig.A.1- A.3 below.

Thrust vs Specific Impulse

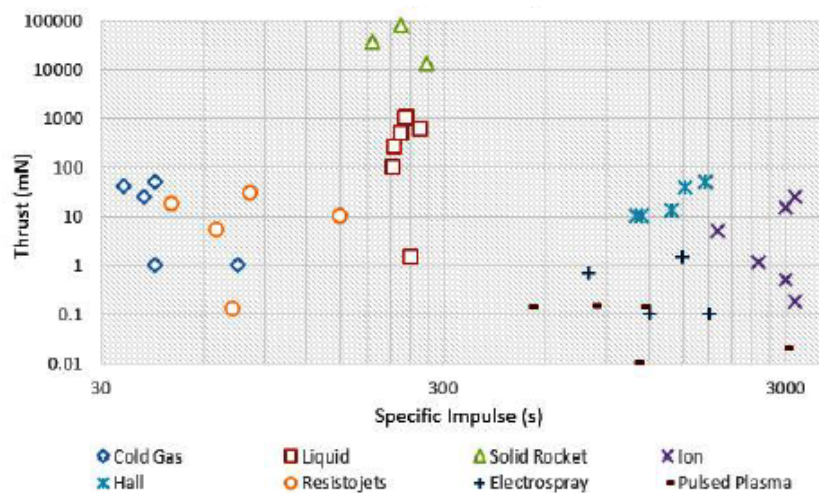


Fig. A.1 Relationship between thrust and specific impulse of various chemical and electrical propulsion systems [5].

The important features of Fig.A.1 are:

- Chemical propulsion systems (like cold gas thrusters) and resistojets are found in the low specific impulse range, with low to moderate thrust capability. They are mainly used for altitude correction applications.
- Liquid and solid rockets occupy a relatively low specific impulse range (due to low exhaust velocities) but produce the highest thrust of any of the systems considered. Solid rockets have a higher propellant density and can thus generate a greater thrust than liquid rockets.
- The remaining electric propulsion systems all occupy the higher end of the specific impulse range (implying high efficiency) in addition to a low to moderate thrust range, with Hall thrusters demonstrating the highest thrust capability among electric propulsion systems.

Power and Thrust to Power Ratio vs Specific Impulse

The power consumption of an electric propulsion system is an important parameter to consider as increased miniaturisation limits the power processing capabilities of a spacecraft and subsequently reduces its usability. It is therefore desirable to have a propulsion system which produces a decent performance from a low power requirement. Fig.A.2 shows the relationship between the power requirements for various electric propulsion systems and their specific impulses while Fig.A.3 shows the relationship between the thrust to power ratio and specific impulse.

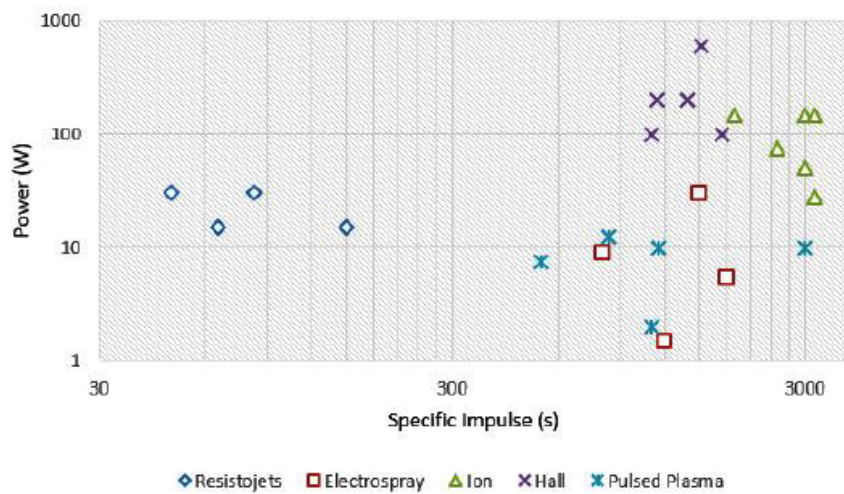


Fig. A.2 Relationship between power and specific impulse of various electrical propulsion systems [5].

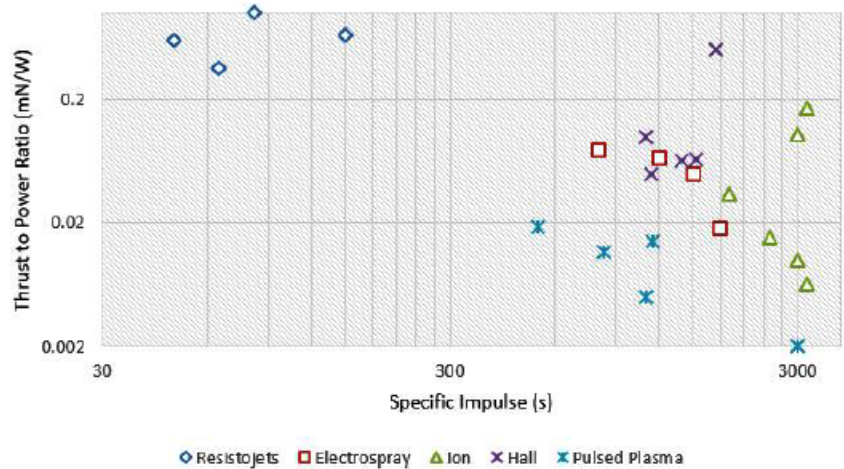


Fig. A.3 Relationship between thrust to power ratio and specific impulse of various electrical propulsion systems [5].

The important features of Figs.A.2 and A.3 are:

- Pulsed Plasma Thrusters and electro spray thrusters have the lowest power requirements (due their simple designs) with the electro spray thrusters producing higher thrust levels for the same power consumption as PPTs. In general PPTs exhibit low operational efficiencies. It must be noted that PPTs (including VATs) and electro spray thrusters can be operated well below the indicated power levels.
- Ion and Hall thrusters have the highest power consumption (owed to the complex features used in their design) and cannot operate below 10W. The RF ion thruster displays the highest specific impulse (due to its high operational efficiency).
- Electro spray and Hall thrusters exhibit noticeably high thrust to power ratios. In the case of Hall thrusters, this results from a low thruster efficiency.
- Lastly, it is observed that resistojets outperform all other electric propulsion systems with regards to the thrust to power ratio but have higher power requirements than both PPTs and electro spray devices and generate significantly lower specific impulses than the rest of the electric propulsion systems considered.

Appendix B

Plasma Physics Derivations

Debye length

When a test charge q_t is inserted within a neutral plasma ($n_e = n_i = n_0$) an electrostatic potential forms around the test charge.

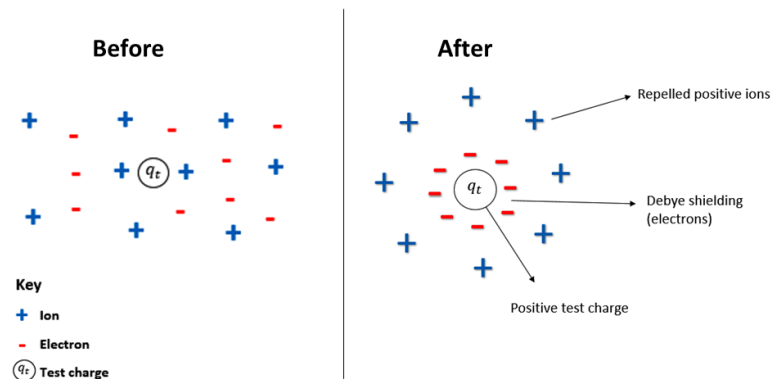


Fig. B.1 Neutral plasma containing a test charge.

The potential around the test charge can be obtained by solving a Poisson equation:

$$\nabla^2 \Phi = -\frac{1}{\epsilon_0} [q_t \delta(\vec{r}) + en_i(\vec{r}) - en_e(\vec{r})]. \quad (\text{B.1})$$

Equation (B.1) states that the Laplacian squared of the potential is equal to the sum of all charges present in the system which are: the test charge q_t , located at $r = 0$, plus the charges of the ions and electrons e , n_i and n_e are the ion and electron number densities respectively.

Ions are considerably larger in mass than electrons where they are so heavy that they do not

move. Therefore, to a first-order approximation, it can be assumed that the ions constitute a fixed positive background. This implies that the ion density is constant i.e. $n_i(\vec{r}) = n_0$. On the other hand the electrons are light and therefore they move, their movements are dictated by the following equation of motion:

$$m_e \frac{d\vec{u}_e}{dt} = e\vec{E} - \frac{1}{n_e} \nabla P_e = -e\vec{E} - \frac{1}{n_e} \nabla(n_e k_B T_e), \quad (\text{B.2})$$

where m_e and \vec{u}_e are the electron mass and velocity respectively. The right hand side of equation (B.2) represents the forces acting on the electrons, given by the electric field \vec{E} and pressure P_e (which can be written in terms of the electron temperature T_e and density). For simplicity, the temperature can be redefined such that it can be measured in units of energy (Joules or electronvolts) i.e. $k_B T_e \rightarrow T_e$.

To further simplify equation (B.2) the following hypotheses are made:

- Assume that the electrons are extremely light (they will respond immediately to the placement of the charged particle in the plasma). Hence, $m_e \rightarrow 0$.
- Assume that the electric field is given by the negative of the gradient of the potential: $\vec{E} = -\nabla\Phi$.
- Assume that the electrons are isothermal i.e. electron temperature is approximately constant: $T_e \approx \text{const}$.

Applying the above hypotheses to equation (B.2) gives:

$$0 \approx e\nabla\Phi - T_e \frac{\nabla n_e}{n_e} = \nabla(e\Phi - T_e \log n_e) \implies e\Phi - T_e \log n_e \approx \text{const}. \quad (\text{B.3})$$

The final expression in equation (B.3) can be written in terms of the electron density:

$$n_e = n_0 \exp\left(\frac{e\Phi}{T_e}\right) \quad (\text{B.4})$$

When there is no perturbation (no electric field produced) the electron density will just be equal to the initial density n_0 . Inserting equation (B.4) into equation (B.1) gives:

$$\nabla^2\Phi = -\frac{1}{\epsilon_0} \left[q_t \delta(\vec{r}) + en_0(\vec{r}) - en_0 \exp\left(\frac{e\Phi}{T_e}\right) \right] \quad (\text{B.5})$$

For small perturbations, $e\Phi \gg T_e \implies \frac{e\Phi}{T_e} \gg 1$, then equation (B.5) can be written as the Taylor expansion:

$$\nabla^2\Phi = -\frac{q_t}{\epsilon_0}\delta(\vec{r}) + \frac{e^2n_0}{\epsilon_0T_e}\Phi = -\frac{q_t}{\epsilon_0}\delta(\vec{r}) + \frac{1}{\lambda_{De}^2}\Phi, \quad (\text{B.6})$$

where $\frac{e^2n_0}{\epsilon_0T_e} = \frac{1}{\lambda_{De}^2}$ follows from dimensional analysis i.e $\frac{1}{\lambda_{De}^2}$ represents an inverse length squared. The term λ_{De} is called the electron Debye length:

$$\lambda_{De} = \sqrt{\frac{\epsilon_0T_e}{e^2n_0}} = 7 \times 10^3 \sqrt{\frac{T_e}{n_0}}, \quad (\text{B.7})$$

Where T_e is in eV and n_0 is in m^{-3} .

Equation (B.6) can now be solved and eventually yields the following solution:

$$\Phi(r) = \frac{1}{4\pi\epsilon_0} \frac{q_t}{r} \exp\left(-\frac{r}{\lambda_{De}}\right). \quad (\text{B.8})$$

The statistical approach used so far is only valid if there is a high number density of electrons and ions within the plasma volume (given by $\lambda_{De}^3 \implies n\lambda_{De}^3 = N_D \gg 1$, where N_D represents the number of charged particles within a Debye cube. If this condition is satisfied, then the one-to-one interactions between particles will be weak. The quasi-neutrality of a plasma is only true at distances beyond the Debye length (deviations from quasi-neutrality will occur at distances shorter than the Debye length).

Plasma frequency

Consider a slab of plasma with an initial electron number density n_e . Assume that the ions in the plasma constitute a fixed background, with the same density as the electrons. The plasma can be separated into three regions: region 1 where the charge is positive ($\rho < 0$); region 2 where the charge is approximately zero ($\rho \approx 0$); and region 3 where the charge is negative ($\rho < 0$). The electrons are displaced from the ions by a distance Δx (Fig. B.2). The displaced electrons will tend to be attracted back towards the ions, causing an oscillatory motion of the electrons with respect to the fixed ion background. The frequency of this resulting oscillation is precisely the plasma frequency.

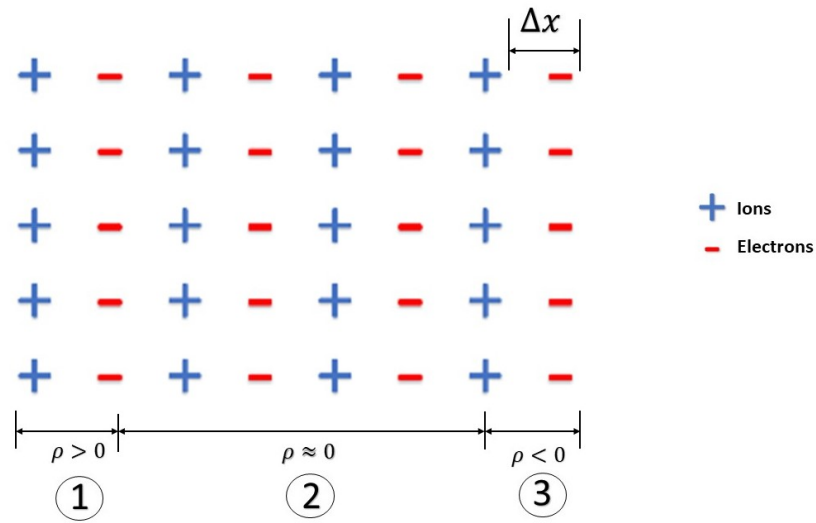


Fig. B.2 Plasma slab with electrons displaced from the fixed ion background.

To find an expression for the plasma frequency, the first step is to evaluate the electric field. From Gauss' law:

$$\frac{dE}{dx} = \frac{\rho}{\epsilon_0}. \quad (\text{B.9})$$

If $E = 0$ at the left end, then in region 2, by integrating Gauss' law for the charge present in region 1 due to the displacement of electrons towards region 3, the expression for E can be obtained in region 2:

$$E = \frac{n_0 e \Delta x}{\epsilon_0}. \quad (\text{B.10})$$

The equation of motion of the electrons, that are subjected to the electric field in (B.10), is then:

$$m_e \frac{d^2 \Delta x}{dt^2} = -eE = -\frac{n_0 e^2}{\epsilon_0} \Delta x \implies \frac{d^2 \Delta x}{dt^2} + \left(\frac{n_0 e^2}{\epsilon_0 m_e} \right) \Delta x = 0. \quad (\text{B.11})$$

The final expression in equation (2.24) has the characteristic form of an oscillatory motion equation with frequency of oscillation given by:

$$\omega_{pe}^2 = \frac{n_0 e^2}{\epsilon_0 m_e} \implies \omega_{pe} = \sqrt{\frac{n_0 e^2}{\epsilon_0 m_e}}. \quad (\text{B.12})$$

This frequency is called the electron plasma frequency and it gives the rate at which electrons oscillate from equilibrium, relative to a static ion background.

Appendix C

Mass Flow Measurement System Calibration

Introduction

An in-house mass flow measurement system, inspired by the orifice flow meter concept [67], was developed to measure very small propellant mass flow rates injected into the thruster. This chapter introduces the orifice plate concept and data obtained from the system's calibration process. The results from the calibration are then compared to previous results, obtained when the same calibration procedure was utilised, to check for repeatability. The results from this calibration process are then used to characterise the propellant flow rate into the thruster in all experimental tests conducted in the large stainless steel vacuum chamber.

Theory

Orifice plate concept

Any fluid flowing through an orifice constriction experiences a pressure drop across the orifice. This change in pressure can be used to determine the fluid's flow rate. Consider the following diagram of a fluid flowing through two chambers separated by an orifice plate with an orifice diameter denoted by D_0 .

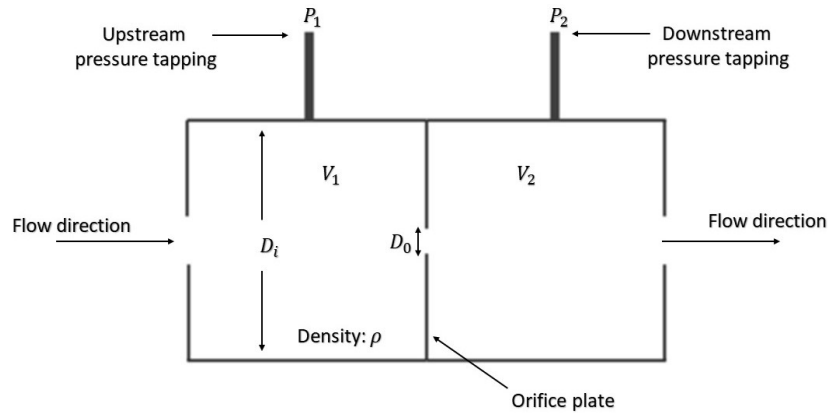


Fig. C.1 Orifice flow concept

If the speed of the fluid is subsonic (i.e. $v < \text{mach } 0.3$), the flow can be described well using the incompressible Bernoulli's equation. Then, the horizontal streamline flow through the axis is given by:

$$\Delta P = P_1 - P_2 = \frac{1}{2}\rho V_2^2 - \frac{1}{2}\rho V_1^2. \quad (\text{C.1})$$

The cross sectional areas of the flow (denoted as A_1 and A_2 respectively) and the volumetric flow rate (denoted by Q) can be used in place of the velocity terms by applying the continuity condition. Hence,

$$\Delta P = \frac{1}{2}\rho Q^2 \frac{1}{A_2^2} \left[1 - \left(\frac{A_2}{A_1} \right)^2 \right]. \quad (\text{C.2})$$

Solving for the volumetric flow rate, gives:

$$Q = \sqrt{\frac{2\Delta P}{\rho}} \frac{A_2}{\sqrt{1 - \left(\frac{A_2}{A_1} \right)^2}}. \quad (\text{C.3})$$

Equation (C.3) holds true only for perfect laminar, inviscid flows. The presence of turbulence and viscosity in real flows results in the dissipation of kinetic energy into heat. This subsequently reduces the flow rate. A discharge coefficient C_d is introduced to account for

this effect:

$$Q = C_d \sqrt{\frac{2\Delta P}{\rho}} \frac{A_2}{\sqrt{1 - \left(\frac{A_2}{A_1}\right)^2}}. \quad (\text{C.4})$$

The exact value of A_2 is uncertain due the complexity of the flow profile downstream from the orifice. To simplify matters, the following substitution is made:

$$C_f A_0 = C_d \frac{A_2}{\sqrt{1 - \left(\frac{A_2}{A_1}\right)^2}}, \quad (\text{C.5})$$

where A_0 is the area of the orifice and C_f represents the flow coefficient which depends on the diameter of the vessel, the orifice diameter and the Reynolds number. The flow coefficient can be experimentally determined or it can be obtained from various reference tables.

Substituting equation (C.5) into equation (C.4) gives the final expression for the volumetric flow rate (in ml/s) of the fluid:

$$Q = C_f A_0 \sqrt{\frac{2\Delta P}{\rho}}. \quad (\text{C.6})$$

Finally, the mass flow rate (in kg/s) can be determined by multiplying equation (C.6) with the density of the fluid:

$$Q_M = \rho Q = C_f A_0 \sqrt{2\rho\Delta P}. \quad (\text{C.7})$$

If the density of the fluid is known, along with the area of the orifice, a calibration curve can be produced upon which a particular mass flow rate can be deduced from a measured pressure differential. The flow coefficient c_f can then be extracted from the resulting curve fit.

Aims

- To produce a calibration curve for the orifice plate setup and to subsequently use the calibration curve to accurately characterise the propellant flow rate.

- To verify the validity of the calibration data by comparing it to a previous iteration of the experiment conducted with the same apparatus.

Mass flow rate calibration procedure

Experimental Setup

The following experimental setup was used to produce the calibration curve from which the mass flow rate could be deduced from a measured pressure difference across the orifice plate box:

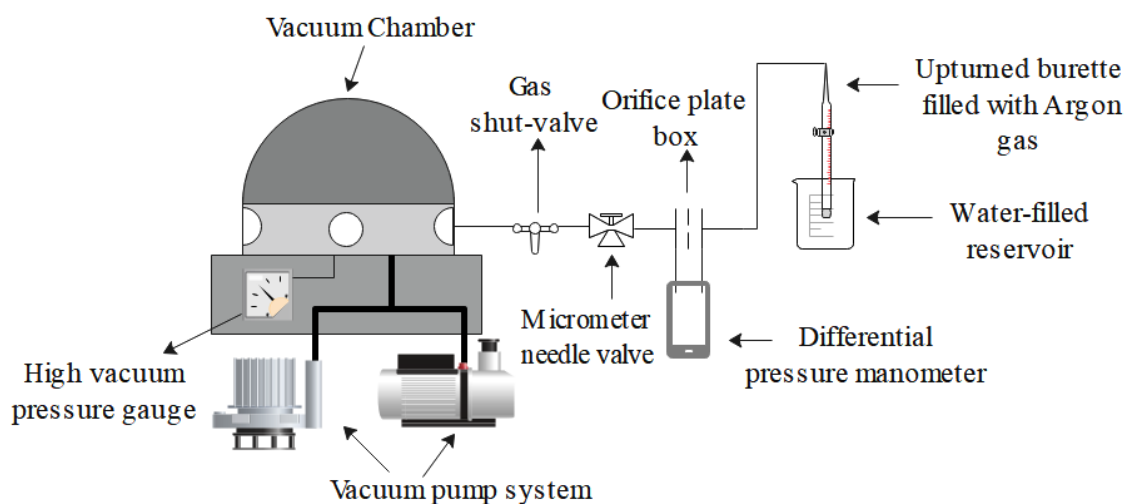


Fig. C.2 Mass flow measurement system calibration setup.

Methodology

The micrometer needle valve and gas-shut off valves were kept closed as the vacuum chamber was evacuated down to 0.10 ± 0.01 Torr. The mass flow measurement system was setup as indicated in Fig.7.7 with the gas inlet from the orifice plate box connected, via a silicone tube, to a 50 ml volume burette upturned in a water reservoir. Initially, the burette's stopcock valve was opened and the argon gas was slowly flushed into it until the water level within the burette was in line with the water level in the reservoir. The stopcock valve was then closed and the tube from the gas inlet of the orifice plate box was reconnected to the burette. The gas shut off valves were then opened, along with the stopcock valve of the burette. The argon was then siphoned from the burette as the entire system was exposed to the vacuum. The micrometer needle valve was adjusted to control the rate at which argon was being

siphoned while the pressure difference, across the orifice plate, was monitored using the manometer. When the desired pressure difference (for calibration) was obtained, the liquid level was allowed to rise to a preferred starting level (usually between 8-10 ml) measured using the graduations on the burette. A stopwatch was then used to measure the time taken to siphon 15.0 ± 0.1 ml of argon from the burette by observing the rising water column. The 15 ml volume was chosen to ensure that the pressure difference across the orifice plate remained constant (within a reasonable error margin) as evacuating a greater volume led to deviations in the pressure difference greater than one unit of error (i.e. > 1 mbar). The measured volumetric flow rate (in ml/s) was then converted to a mass flow rate (in kg/s) by multiplying the results with the density of argon (1.66 kg/m^3 at an ambient temperature of $293 \pm 3 \text{ K}$).

Results and discussion

A series of trials were conducted in three different pressure ranges. The raw data from these trials can be found in Table C.1. The initial pressure difference, denoted as ΔP_i , was measured at the starting point; and the final pressure difference, denoted as ΔP_f , was measured after the 15.0 ± 0.1 ml volume of argon gas had been evacuated. According to equation (C.7), the volume flow rate, and subsequently the mass flow rate, was expected to increase with an increased pressure differential, i.e. Q_M is proportional to the one half power of ΔP . This general trend was observed in the data. The average pressure differential and the average time taken to evacuate 15.0 ± 0.1 ml of argon at each pressure range was calculated from the raw data and is shown in Table C.2. Equation (C.7) was then fitted to the calibration data to produce the calibration curve for the mass flow measurement system displayed in Fig.C.3.

Wright [2] states that although this calibration procedure may yield accurate results with a minimum time investment, a careful approach needs to be taken to ensure that no liquids are sucked into the vacuum chamber, as this could potentially damage the vacuum system. It is also noted that since the siphoning of 15 ml of the gas is measured visually using the graduations on the burette, and since the stopwatch is controlled manually, the possibility of human error in parallax and reaction time may slightly decrease the validity of the data. However, these errors have been taken into account in the flow rate calculations.

Table C.1 Data obtained from the mass flow rate calibration experiment. The time taken to evacuate 15 ± 0.1 ml of argon from the burette is measured at various pressure differentials. ΔP_i is the differential pressure measured at the beginning of the evacuation and ΔP_f is the final pressure measured after the 15 ml of argon had been evacuated. All tests were conducted at an ambient temperature of 293 ± 3 K, with the vacuum chamber evacuated down to 0.10 ± 0.01 Torr.

$\Delta P_i (\pm 0.2 \text{ mbar})$	$\Delta P_f (\pm 0.2 \text{ mbar})$	$\Delta P_{ave} (\pm 0.2 \text{ mbar})$	Time (s) $\pm 3s$
5.6	5.8	5.7	195
5.8	6.2	6	207
5.6	5.6	5.6	222
5.7	6.2	5.95	222
5.6	5.6	5.6	165
5.6	5.5	5.55	174
5.5	5.9	5.7	195
5.5	5.8	5.65	153
5.7	5.6	5.65	177
5.6	5.7	5.65	198
10.5	10.5	10.5	120
10.7	10.3	10.5	153
10.5	10.2	10.35	129
10.2	10	10.1	144
10.6	10.7	10.65	120
10.7	10.6	10.65	123
10.6	10.5	10.55	132
10.5	10.4	10.45	144
10.4	10.2	10.3	159
10.4	10.2	10.3	126
10.2	9.8	10	147
20.5	20.4	20.45	90
20.5	20	20.25	96
20.6	20.6	20.6	96
20.8	21	20.9	105
20.6	20.7	20.65	111
20.4	20	20.2	120
20.7	21	20.85	123
20.6	20.5	20.55	108
20.7	20.8	20.75	102
20.8	20.7	20.75	129
20.6	20.3	20.45	117

Table C.2 The calculated average pressure differential and corresponding average evacuation time, along with the calculated Volume Flow Rates (VFR) and Mass Flow Rates (MFR) obtained using the data from Table C.1.

ΔP_{ave} (mbar)	Average Time (s)	VFR (ml/s)	Error (ml/s)	MFR (10^{-7} kg/s)	Error (kg/s)
5.71	190.80	0.079	± 0.001	1.31	$\pm 2.20 \times 10^{-9}$
10.40	136.09	0.110	± 0.003	1.83	$\pm 4.16 \times 10^{-9}$
20.58	108.82	0.138	± 0.004	2.29	$\pm 6.41 \times 10^{-9}$

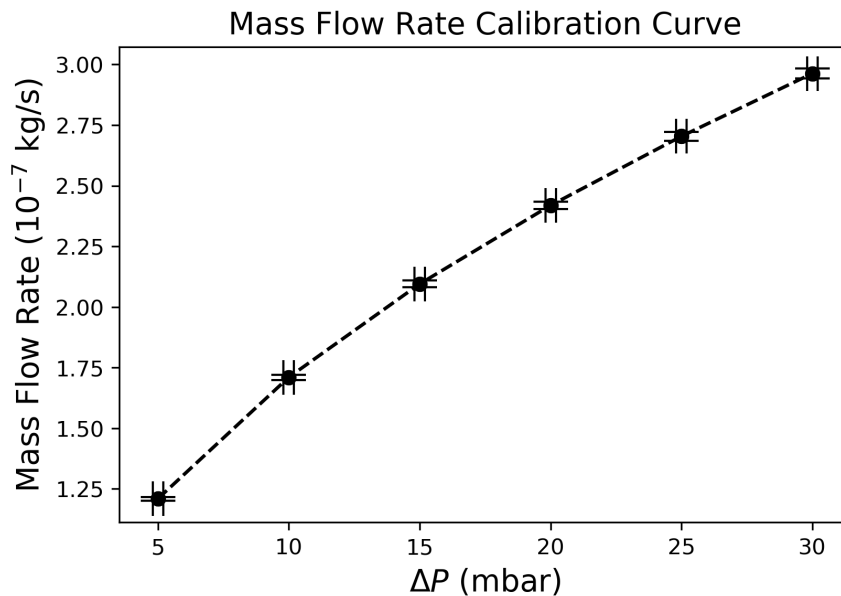


Fig. C.3 Fitted calibration curve for the mass flow measurement system

The results for the calculated time-average mass flow rates are in close agreement with the results obtained in the previous iteration of this calibration process. The flow rates measured in [10] are also on the order of 10^{-7} kg/s with an error of 2×10^{-8} kg/s at the roughly the same pressure differentials (see for example [10], p.75). The author of [10] also provides a comprehensive analysis of the system's working principle along with the necessary underlying assumptions and a justification for the theoretical model (refer to [10], p.63-79 for more details).

Error Analysis

The error in the volume flow rate $\delta(\text{VFR})$ is computed as:

$$\delta(VFR) = (VFR) \sqrt{\left(\frac{\delta V}{V}\right)^2 + \left(\frac{\delta t}{t}\right)^2}, \quad (C.8)$$

where δV and δt are the errors in evacuated volume and time respectively.

Table C.3 shows how the errors in the volume flow rate (shown in Table C.2) were calculated using equation (C.8). The mass flow rates and their corresponding errors are obtained by multiplying VFR and $\delta(VFR)$, respectively, by the density of argon gas, $\rho_{Ar} = 1.64 \times 10^{-7}$ kg/cm³ at 1 atm and 293 K (source: www.concoa.com/argon properties).

Table C.3 Calculation of errors in volume flow rate and mass flow rate.

ΔP_{ave} (mbar)	t (s)	δt (s)	V (ml)	δV (ml)	VFR (ml/s)	$\delta(VFR)$ (ml/s)	δMFR (kg/s)
5.71	190.80	± 3	15.0	± 0.1	0.079	± 0.001	± 2.20 × 10 ⁻⁹
10.40	136.09	± 3	15.0	± 0.1	0.110	± 0.003	± 4.16 × 10 ⁻⁹
20.58	108.82	± 3	15.0	± 0.1	0.138	± 0.004	± 6.41 × 10 ⁻⁹

Conclusion

A mass flow measurement system was assembled utilising the orifice plate concept. A calibration curve for the system was produced by measuring the average time required to evacuate a set volume of argon gas at a particular pressure differential across the orifice plate. The argon mass flow rate, at a particular pressure differential, was then deduced from the resulting curve fit to the data. Results obtained from this calibration procedure are in close agreement with those obtained in a previous experiment under almost identical conditions. This provides support towards the overall validity of the data.

Appendix D

Calculation of Beam Divergence Angle

Table 7.1 contains the system's thrust calculated from the measured ion beam current and acceleration voltage. The thrust was calculated under the following assumptions:

1. The beam consisted almost entirely of a singly ionised species.
2. The beam exhibited minimum divergence upon exiting the cathode aperture (i.e. the extracted beam satisfies the perveance matched case).

The first assumption was justified in section 6.2. The assumption of minimum beam divergence can be justified by measuring the spot size of the beam on the collector plate and calculating the divergence angle θ using:

$$\theta = \arctan \frac{R-r}{L}, \quad (\text{D.1})$$

where R is the radius of the beam spot, normal to the beam axis, which encloses 95% of the total beam current, r is the radius of the beam at the exit (cathode) aperture and L is the distance from the exit aperture to the collector plate (refer to Fig.D.1).

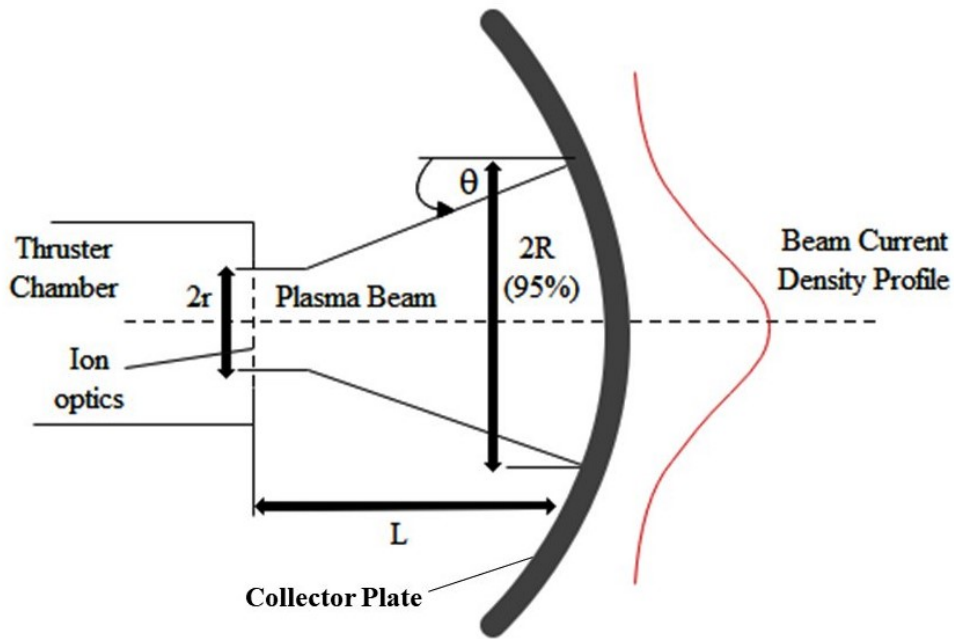


Fig. D.1 Schematic of the beam current density profile and the beam divergence angle.

Fig.D.2 displays a colour adjusted image of the beam spots formed by the 1x2 mm aperture (left) and the 2x2 mm aperture (right). In the case of the double aperture configuration, two distinct spots can be seen on the plate. The beam spot size on the collector plate was measured to be 20 ± 5 mm for the single aperture and 42 ± 5 mm for a double aperture system. For the single aperture system the radius of the beam at the aperture exit is equal to the radius of the aperture, i.e. $r_1 = 1$ mm. In the case of the double aperture configuration, the beam radius at the aperture exit is taken to be the sum of the radii of both apertures, i.e. $r_2 = 2$ mm. The distance from the cathode to the collector plate, where the beam spot was measured, was 90 ± 10 mm. Substituting the appropriate values into equation (D.1) gives:

$$\theta_1 = 5.71^\circ \pm 1.57^\circ, \quad (\text{D.2})$$

$$\theta_2 = 11.92^\circ \pm 1.52^\circ, \quad (\text{D.3})$$

where θ_1 and θ_2 represent the divergence angles for the 1x2 mm and 2x2 mm configurations respectively. Hence, the maximum thrust correction factor F_t , taking into account the largest error in each case is:

$$F_{t,1} = \cos(\theta_1) = \cos(6.34^\circ) = 0.994 \approx 1, \quad (\text{D.4})$$

$$F_{t,2} = \cos(\theta_2) = \cos(13.43^\circ) = 0.972 \approx 1. \quad (\text{D.5})$$

Therefore the loss in thrust never exceeds 3%, and for practical purposes the thrust correction factor can be reasonably approximated as $F_t \approx 1$. Subsequently, the total correction factor γ also becomes unity and the thrust can be estimated to good approximation using equation (7.8).

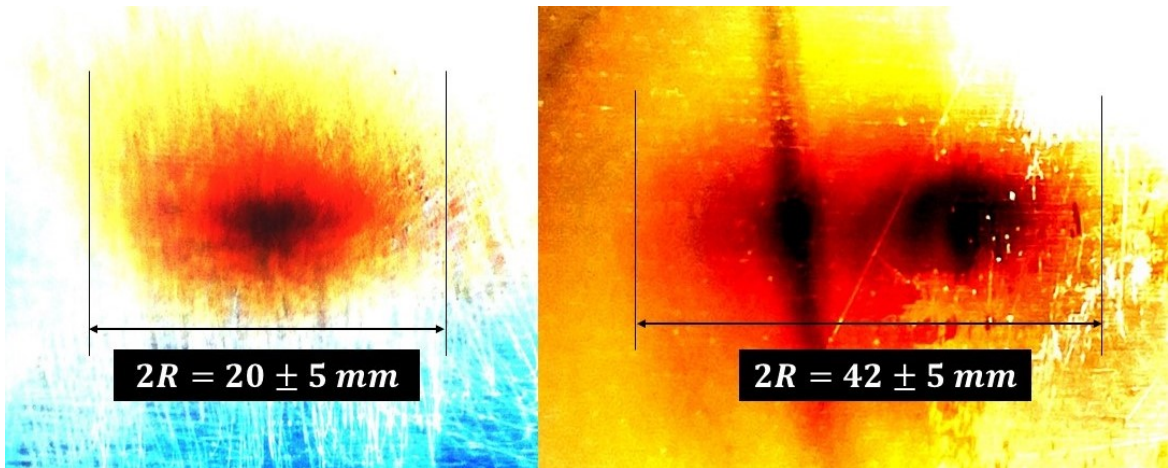


Fig. D.2 Colour adjusted image of the beam spot size for the 1x2 mm and 2x2 mm extractor apertures measured at the collector plate.

Appendix E

Data and Error Analysis

E.1 Preliminary Experiments

Error bars for Paschen curves

Uncertainty in electrode separation gap/tube length

The tube length is measured using a vernier caliper which has a reading error of 1/20 mm or 0.05 mm. Thus, the actual thruster tube length is 40.00 ± 0.05 mm.

Uncertainty in pressure readings from Kurt J.Lesker vacuum gauge

For pressures ranging from 1×10^{-3} to 400 Torr, the vacuum gauge has an uncertainty of $\pm 10\%$ of the reading. For example, if the vacuum gauge reads 1.00 Torr the uncertainty in measurement is ± 0.10 Torr.

Origin of the error bars in the Paschen curve

The uncertainty in the measured breakdown voltage reading is taken as the smallest division on the power supply's front panel display:

$$\delta V_b = 0.01 \text{ kV}. \tag{E.1}$$

The error in the product of pressure p and electrode separation distance d is calculated as follows:

$$\delta(p \cdot d) = (p \cdot d) \sqrt{\left(\frac{\delta p}{p}\right)^2 + \left(\frac{\delta d}{d}\right)^2}. \quad (\text{E.2})$$

However, since $\left(\frac{\delta d}{d}\right)^2 = \left(\frac{0.05}{40}\right)^2 \ll \left(\frac{\delta p}{p}\right)^2$, the expression above can be approximated as:

$$\delta(p \cdot d) \sim (p \cdot d) \left(\frac{\delta p}{p}\right). \quad (\text{E.3})$$

For example, for $(p) = 0.80$ Torr·cm, the corresponding pressure is 0.2 Torr and the error in the pressure measurement $\delta p = 0.1 \times 0.2 = \pm 0.02$ Torr. The the error in $(p \cdot d)$ is:

$$\delta(p \cdot d) = (0.80) \left(\frac{0.02}{0.2}\right) = \pm 0.08 \text{ Torr} \cdot \text{cm}. \quad (\text{E.4})$$

These uncertainties were used to produce the error bars in Fig.6.3.

Table E.1 Raw data, with errors, used to plot the Paschen curve in Fig.6.3. Note that the breakdown voltage represented here is taken as the average over three trials.

P·d (Torr·cm)	$\delta(P \cdot d)$ (Torr·cm)	V_b (kV)	δV_b (kV)
0.40	± 0.04	0.77	± 0.01
0.80	± 0.08	0.61	± 0.01
1.20	± 0.12	0.61	± 0.01
2.00	± 0.20	0.55	± 0.01
2.40	± 0.24	0.56	± 0.01
2.80	± 0.28	0.55	± 0.01
3.20	± 0.32	0.57	± 0.01
4.00	± 0.40	0.58	± 0.01
4.80	± 0.48	0.59	± 0.01
5.20	± 0.52	0.59	± 0.01
5.60	± 0.56	0.63	± 0.01
6.00	± 0.60	0.61	± 0.01
6.40	± 0.64	0.61	± 0.01
6.80	± 0.68	0.64	± 0.01
7.20	± 0.72	0.67	± 0.01
7.60	± 0.76	0.71	± 0.01
8.00	± 0.80	0.72	± 0.01

Error bars for voltage-current curves

The uncertainty in the measured voltage (δV) from the power supply and the uncertainty in the discharge current (δI) is taken as the smallest division on the power supply's front panel display:

$$\delta V = 0.01 \text{ kV}, \quad (\text{E.5})$$

$$\delta I = 0.001 \text{ mA}. \quad (\text{E.6})$$

These values were used to generate the error bars in Fig.6.4 and Fig.6.7.

Table E.2 Raw data, with errors, used to plot Fig.6.4. Note that the discharge voltage represented in each pressure range is taken as the average over five trials.

0.80-0.85 Torr			
Current (mA)	$\delta I(mA)$	V_d (kV)	δV_d (kV)
0.500	± 0.001	0.44	± 0.01
1.000	± 0.001	0.50	± 0.01
1.500	± 0.001	0.54	± 0.01
2.000	± 0.001	0.58	± 0.01
2.500	± 0.001	0.60	± 0.01
3.000	± 0.001	0.63	± 0.01
3.500	± 0.001	0.66	± 0.01
4.000	± 0.001	0.68	± 0.01
4.500	± 0.001	0.71	± 0.01
5.000	± 0.001	0.75	± 0.01
5.500	± 0.001	0.78	± 0.01
6.000	± 0.001	0.81	± 0.01
0.85-0.90 Torr			
Current (mA)	$\delta I(mA)$	V_d (kV)	δV_d (kV)
0.500	± 0.001	0.39	± 0.01
1.000	± 0.001	0.45	± 0.01
1.500	± 0.001	0.48	± 0.01
2.000	± 0.001	0.51	± 0.01
2.500	± 0.001	0.54	± 0.01
3.000	± 0.001	0.57	± 0.01
3.500	± 0.001	0.59	± 0.01
4.000	± 0.001	0.62	± 0.01
4.500	± 0.001	0.64	± 0.01
5.000	± 0.001	0.67	± 0.01
5.500	± 0.001	0.70	± 0.01
6.000	± 0.001	0.73	± 0.01

Table E.3 Continuation of data from Table.E.2

0.90-0.95 Torr			
Current (mA)	$\delta I(mA)$	V_d (kV)	δV_d (kV)
0.500	± 0.001	0.42	± 0.01
1.000	± 0.001	0.48	± 0.01
1.500	± 0.001	0.51	± 0.01
2.000	± 0.001	0.53	± 0.01
2.500	± 0.001	0.55	± 0.01
3.000	± 0.001	0.58	± 0.01
3.500	± 0.001	0.60	± 0.01
4.000	± 0.001	0.62	± 0.01
4.500	± 0.001	0.64	± 0.01
5.000	± 0.001	0.66	± 0.01
5.500	± 0.001	0.68	± 0.01
6.000	± 0.001	0.70	± 0.01

The error bars displayed in Fig.6.5 and Fig.6.6 originate from the standard deviation. They represent the magnitude that a measured voltage deviates from the mean voltage over all four trials i.e.

$$\delta V_i = \sigma = \sqrt{\frac{\sum (V_i - \bar{V}_i)^2}{N}}, \quad (\text{E.7})$$

where σ is the standard deviation, V_i is the measured voltage in a particular trial, \bar{V}_i is the average voltage over four trials and N is the number of trials.

Table E.4 The calculated standard deviation of the measured voltage across five trials used to generate the error bars in Fig.6.5.

1 mm Aperture	Measured Voltage (± 0.01 kV)					
I_d (mA)	Trial 1	Trial 2	Trial 3	Trial 4	Average	σ
0.000	0.50	0.50	0.50	0.50	0.50	± 0.00
0.500	0.53	0.53	0.51	0.51	0.52	± 0.01
1.000	0.60	0.61	0.58	0.54	0.58	± 0.03
1.500	0.62	0.67	0.64	0.61	0.64	± 0.02
2.000	0.68	0.71	0.70	0.66	0.69	± 0.02
2.500	0.71	0.74	0.74	0.70	0.72	± 0.02
3.000	0.74	0.75	0.78	0.73	0.75	± 0.02
3.500	0.76	0.80	0.81	0.76	0.78	± 0.02
4.000	0.78	0.81	0.84	0.77	0.80	± 0.03
4.500	0.78	0.77	0.85	0.79	0.80	± 0.03
5.000	0.79	0.78	0.86	0.79	0.81	± 0.03
5.500	0.81	0.81	0.86	0.80	0.82	± 0.02
6.000	0.82	0.85	0.88	0.82	0.84	± 0.02

Table E.5 The calculated standard deviation of the measured voltage across five trials used to generate the error bars in Fig.6.5.

2 mm Aperture	Measured Voltage (± 0.01 kV)					
I_d (mA)	Trial 1	Trial 2	Trial 3	Trial 4	Average	σ
0.000	0.30	0.30	0.30	0.40	0.33	± 0.04
0.500	0.37	0.39	0.38	0.43	0.39	± 0.02
1.000	0.41	0.44	0.43	0.49	0.44	± 0.03
1.500	0.44	0.48	0.47	0.51	0.48	± 0.03
2.000	0.48	0.50	0.51	0.54	0.51	± 0.02
2.500	0.52	0.53	0.54	0.57	0.54	± 0.02
3.000	0.55	0.56	0.57	0.60	0.57	± 0.02
3.500	0.57	0.58	0.59	0.62	0.59	± 0.02
4.000	0.59	0.60	0.61	0.65	0.61	± 0.02
4.500	0.60	0.62	0.63	0.66	0.63	± 0.02
5.000	0.62	0.63	0.64	0.68	0.64	± 0.02
5.500	0.63	0.64	0.65	0.69	0.65	± 0.02
6.000	0.64	0.65	0.66	0.70	0.66	± 0.02

Table E.6 The calculated standard deviation of the measured voltage across five trials used to generate the error bars in Fig.6.6.

4 mm Aperture	Measured Voltage (± 0.01 kV)					
I_d (mA)	Trial 1	Trial 2	Trial 3	Trial 4	Average	σ
0.000	0.50	0.50	0.50	0.45	0.49	± 0.02
0.500	0.60	0.55	0.51	0.49	0.54	± 0.04
1.000	0.64	0.65	0.61	0.58	0.62	± 0.03
1.500	0.67	0.67	0.66	0.68	0.67	± 0.01
2.000	0.71	0.74	0.70	0.71	0.72	± 0.02
2.500	0.72	0.77	0.76	0.73	0.75	± 0.02
3.000	0.78	0.82	0.88	0.82	0.83	± 0.04
3.500	0.82	0.81	0.92	0.88	0.86	± 0.04
4.000	0.85	0.90	0.94	0.93	0.91	± 0.04
4.500	0.86	0.93	0.96	0.94	0.92	± 0.04
5.000	0.88	0.94	0.97	0.96	0.94	± 0.03
5.500	0.90	0.95	0.98	0.96	0.95	± 0.03
6.000	0.92	0.98	1.00	0.97	0.97	± 0.03

Table E.7 The calculated standard deviation of the measured voltage across five trials used to generate the error bars in Fig.6.6.

8 mm Aperture	Measured Voltage (± 0.01 kV)					
I_d (mA)	Trial 1	Trial 2	Trial 3	Trial 4	Average	σ
0.000	0.30	0.30	0.30	0.30	0.30	± 0.00
0.500	0.39	0.36	0.36	0.36	0.37	± 0.01
1.000	0.45	0.43	0.43	0.44	0.44	± 0.01
1.500	0.50	0.48	0.49	0.48	0.49	± 0.01
2.000	0.53	0.52	0.52	0.52	0.52	± 0.00
2.500	0.55	0.55	0.55	0.56	0.55	± 0.00
3.000	0.58	0.59	0.58	0.58	0.58	± 0.00
3.500	0.60	0.61	0.60	0.60	0.60	± 0.00
4.000	0.62	0.62	0.62	0.63	0.62	± 0.00
4.500	0.64	0.64	0.64	0.65	0.64	± 0.00
5.000	0.66	0.66	0.66	0.66	0.66	± 0.00
5.500	0.67	0.67	0.67	0.68	0.67	± 0.00
6.000	0.69	0.68	0.69	0.70	0.69	± 0.01

Error bars for power vs discharge current curve

The error in the calculated discharge power (δP) used to generate the error bars in Fig.6.8 is found from the following expression:

$$\delta P = P \sqrt{\left(\frac{\delta V}{V}\right)^2 + \left(\frac{\delta I}{I}\right)^2}. \quad (\text{E.8})$$

For example, for the 8 mm aperture configuration, at a discharge current of 4.000 ± 0.001 mA and measured voltage of 0.62 ± 0.01 kV, the discharge power is 2.49 ± 0.04 W, i.e:

$$\delta P = 2.49 \sqrt{\left(\frac{0.01}{0.62}\right)^2 + \left(\frac{0.001}{4.000}\right)^2} = 0.04 \text{ W}. \quad (\text{E.9})$$

Table E.8 Raw data, with errors, used to generate Fig.6.8.

1 mm Aperture		
I_d (mA)	P_d (W)	δP_d
0.500	0.26	± 0.01
1.000	0.58	± 0.01
1.500	0.95	± 0.02
2.000	1.38	± 0.02
2.500	1.81	± 0.03
3.000	2.25	± 0.03
3.500	2.74	± 0.04
4.000	3.20	± 0.04
4.500	3.59	± 0.05
5.000	4.03	± 0.05
5.500	4.51	± 0.06
6.000	5.06	± 0.06
2 mm Aperture		
I_d (mA)	P_d (W)	δP_d
0.500	0.20	± 0.01
1.000	0.44	± 0.01
1.500	0.71	± 0.02
2.000	1.02	± 0.02
2.500	1.35	± 0.03
3.000	1.71	± 0.03
3.500	2.07	± 0.04
4.000	2.45	± 0.04
4.500	2.82	± 0.05
5.000	3.21	± 0.05
5.500	3.59	± 0.06
6.000	3.98	± 0.06

Table E.9 Raw data, with errors, used to generate Fig.6.8.

4 mm Aperture		
I_d (mA)	P_d (W)	δP_d
0.500	0.27	± 0.01
1.000	0.62	± 0.01
1.500	1.01	± 0.02
2.000	1.43	± 0.02
2.500	1.86	± 0.03
3.000	2.48	± 0.03
3.500	3.00	± 0.04
4.000	3.62	± 0.04
4.500	4.15	± 0.05
5.000	4.69	± 0.05
5.500	5.21	± 0.06
6.000	5.81	± 0.06
8 mm Aperture		
I_d (mA)	P_d (W)	δP_d
0.500	0.18	± 0.01
1.000	0.44	± 0.01
1.500	0.73	± 0.02
2.000	1.05	± 0.02
2.500	1.38	± 0.03
3.000	1.75	± 0.03
3.500	2.11	± 0.04
4.000	2.49	± 0.04
4.500	2.89	± 0.05
5.000	3.30	± 0.05
5.500	3.70	± 0.06
6.000	4.14	± 0.06

E.2 Ion Beam Current Measurements and Thrust Estimation

Error bars for V-I curves with changing aperture numbers

The error bars displayed in Fig.7.10 and on the left of Fig.7.11 originate from the standard deviation. They represent the magnitude that a measured discharge current deviates from the mean current over all five trials i.e.

$$\delta I_i = \sigma = \sqrt{\frac{\sum (I_i - \bar{I}_i)^2}{N}}, \quad (\text{E.10})$$

where, σ is the standard deviation, I_i is the measured discharge current in a particular trial, \bar{I}_i is the average current over five trials and N is the number of trials.

Table E.10 Standard deviation of measured discharge current across five trials, used to produce the error bars for the V-I curve for the 1x2 mm electrode aperture configuration in Fig.7.10.

	Discharge Current (mA)					
Applied Voltage (kV)	Trial 1	Trial 2	Trial 3	Trial 4	Trial 5	σ
0.00	0.00	0.00	0.00	0.00	0.00	± 0.00
0.50	0.06	0.08	0.06	0.05	0.07	± 0.01
1.00	0.23	0.22	0.24	0.21	0.23	± 0.01
1.50	0.80	0.76	0.78	0.78	0.73	± 0.02
2.00	1.59	1.62	1.57	1.56	1.58	± 0.02
2.50	2.67	2.59	2.68	2.59	2.63	± 0.04
3.00	3.81	3.78	3.81	3.59	3.76	± 0.08

Table E.11 Standard deviation of measured discharge current across five trials, used to produce the error bars for the V-I curve for the 2x2 mm electrode aperture configuration in Fig.7.10.

Applied Voltage (kV)	Discharge Current (mA)					σ
	Trial 1	Trial 2	Trial 3	Trial 4	Trial 5	
0.00	0.00	0.00	0.00	0.00	0.00	± 0.00
0.50	0.06	0.06	0.00	0.06	0.07	± 0.03
1.00	0.08	0.07	0.06	0.08	0.08	± 0.01
1.50	0.13	0.12	0.15	0.16	0.20	± 0.03
2.00	0.40	0.38	0.41	0.46	0.46	± 0.03
2.50	0.92	0.77	0.82	0.90	0.91	± 0.06
3.00	1.44	1.28	1.44	1.49	1.50	± 0.08
3.50	1.98	1.93	2.08	2.15	2.21	± 0.11
4.00	2.68	2.43	2.61	2.70	2.62	± 0.09

The error bars displayed on the right of Fig.7.11 and on Fig.7.12 are obtained from the resolution of the of the current sensor and the voltage resolution on the power supply, i.e $\delta I = \pm 0.1$ mA and $\delta V = \pm 0.01$ V.

Error bars for ion beam current measurement curve

Error in measured beam current

The error in the ion beam current δI_b used to produce the error bars in Fig.7.15 and Fig.7.16 were calculated as:

$$\delta I_b = I_b \sqrt{\left(\frac{\delta V_R}{V_R}\right)^2 + \left(\frac{\delta R_{true}}{R_{true}}\right)^2}, \quad (\text{E.11})$$

where $\delta R_{true} = 0.01$ M Ω and $\delta V_R = 0.01$ V are the smallest units of measurement on the ammeter and the oscilloscope used to make the measurements for the resistance and voltage respectively.

Table E.12 The calculated error in the measured ion beam current use to generate the error bars in Fig.7.15.

0.82 ± 0.01MΩ			
I_d (mA)	V_a (kV)	I_b (μA)	δI_b (μA)
0.50	1.57	1.87	± 0.05
1.00	2.02	5.21	± 0.12
1.50	2.43	9.94	± 0.22
2.00	2.80	15.50	± 0.34
2.50	3.10	16.40	± 0.36
3.00	3.36	18.25	± 0.41
1.64 ± 0.01MΩ			
I_d (mA)	V_a (kV)	I_b (μA)	δI_b (μA)
0.50	1.29	3.43	± 0.06
1.00	1.72	8.25	± 0.13
1.50	2.12	13.51	± 0.22
2.00	2.52	18.30	± 0.29
2.50	2.91	22.75	± 0.37
3.00	3.25	27.69	± 0.45
2.45 ± 0.01MΩ			
I_d (mA)	V_a (kV)	I_b (μA)	δI_b (μA)
0.50	1.30	4.61	± 0.07
1.00	1.77	10.29	± 0.15
1.50	2.15	17.27	± 0.24
2.00	2.51	25.72	± 0.36
2.50	2.85	34.59	± 0.49
3.00	3.17	47.08	± 0.66

Error in estimated thrust

The thrust can be expressed as a function of the acceleration voltage V_a and the beam current I_b as:

$$T(V_a, I_b) = CV_a^{1/2} I_b, \quad (\text{E.12})$$

where the constant $C = \sqrt{\frac{2m_i}{e}} = 2.8 \times 10^{-4}$ is expressed in SI units.

The error in the estimated thrust δT can then be calculated using the following expression:

$$\delta T = \sqrt{\left(\frac{\partial T}{\partial V_a} \delta V_a\right)^2 + \left(\frac{\partial T}{\partial I_b} \delta I_b\right)^2}, \quad (\text{E.13})$$

where:

$$\frac{\partial T}{\partial V_a} = \frac{CI_b}{2\sqrt{V_a}}, \quad (\text{E.14})$$

$$\frac{\partial T}{\partial I_b} = CV_a^{1/2}. \quad (\text{E.15})$$

Substituting in the appropriate values gives the error estimates found in Table 7.1.

Error in theoretical ion beam current

The theoretical ion beam current I_b^{Theo} depends on the acceleration voltage and is calculated using equation (7.3):

$$I_b^{Theo} = PV_a^{3/2}, \quad (\text{E.16})$$

where $P = \frac{4}{9}\pi\epsilon_0\sqrt{\frac{2e}{m_i}}S^2 = 3.17 \times 10^{-11}$ is the perveance expressed in SI units.

The error in the calculated theoretical ion beam current δI_b^{theo} is determined using the following expression:

$$\delta I_b^{Theo} = \sqrt{\left(\frac{\partial I_b^{Theo}}{\partial V_a} \delta V_a\right)^2} = \frac{3}{2}PV_a^{1/2}\delta V_a. \quad (\text{E.17})$$

Substituting in the appropriate values gives the errors listed in Table 7.2.

Error bars for ion production efficiency and electrical efficiency

Error in ion production efficiency

The error in the discharge power is calculated in the same way as equation (E.8), i.e:

$$\delta P_d = P_d \sqrt{\left(\frac{\delta V_a}{V_a}\right)^2 + \left(\frac{\delta I_d}{I_d}\right)^2}. \quad (\text{E.18})$$

Here, V_a and I_d are the acceleration voltage and discharge current respectively.

The error in the ion production efficiency $\delta \eta_d$ is calculated using the following expression:

$$\delta \eta_d = \eta_d \sqrt{\left(\frac{\delta P_d}{P_d}\right)^2 + \left(\frac{\delta I_b}{I_b}\right)^2}. \quad (\text{E.19})$$

The expression (E.19) was used to obtain the error bars in Fig.7.17.

Error in electrical efficiency

The error in the total power δP_T is:

$$\delta P_T = \sqrt{(\delta P_b)^2 + (\delta P_d)^2}, \quad (\text{E.20})$$

where,

$$\delta P_b = P_b \sqrt{\left(\frac{\delta I_b}{I_b}\right)^2 + \left(\frac{\delta V_a}{V_a}\right)^2}, \quad (\text{E.21})$$

and δP_d can be obtained from equation (E.18).

The error in electrical efficiency $\delta \eta_e$ is given by:

$$\delta \eta_e = \eta_e \sqrt{\left(\frac{\delta P_b}{P_b}\right)^2 + \left(\frac{\delta P_T}{P_T}\right)^2}. \quad (\text{E.22})$$

The expression (E.22) was used to obtain the error bars in Fig.7.18.

Error bars for thrust to power ratio

The error in the calculated thrust-to-power ratio $\delta(T/P)$ is calculated using:

$$\delta(T/P) = (T/P) \sqrt{\left(\frac{\delta T}{T}\right)^2 + \left(\frac{\delta P_T}{P_T}\right)^2}. \quad (\text{E.23})$$

Substituting in the appropriate values gives the error bars in Fig.7.19.